

Duquesne University

Duquesne Scholarship Collection

Electronic Theses and Dissertations

Fall 2013

Oxide based earth abundant semiconductors and oxygen evolving catalysts for photoelectrochemical and PV driven water splitting

Mourad Frites

Follow this and additional works at: <https://dsc.duq.edu/etd>

Recommended Citation

Frites, M. (2013). Oxide based earth abundant semiconductors and oxygen evolving catalysts for photoelectrochemical and PV driven water splitting (Doctoral dissertation, Duquesne University). Retrieved from <https://dsc.duq.edu/etd/555>

This Immediate Access is brought to you for free and open access by Duquesne Scholarship Collection. It has been accepted for inclusion in Electronic Theses and Dissertations by an authorized administrator of Duquesne Scholarship Collection. For more information, please contact beharyr@duq.edu.

OXIDE BASED EARTH ABUNDANT SEMICONDUCTORS AND OXYGEN
EVOLVING CATALYSTS FOR PHOTOELECTROCHEMICAL AND PV DRIVEN
WATER SPLITTING

A Dissertation

Submitted to the Bayer School of Natural and Environmental Sciences

Duquesne University

In partial fulfillment of the requirement for the degree of
Doctor of Philosophy in Chemistry

By

Mourad Frites

December 2013

Copyright by

Mourad Frites

2013

OXIDE BASED EARTH ABUNDANT SEMICONDUCTORS AND OXYGEN
EVOLVING CATALYSTS FOR PHOTOELECTROCHEMICAL AND PV DRIVEN
WATER SPLITTING

By

Mourad Frites

Approved November 11, 2013

Shahed U. M. Khan, Ph.D.
Associate Professor of Chemistry and
Biochemistry
Duquesne University
(Dissertation Director)

Ellen Gawalt, Ph.D.
Associate Professor of Chemistry and
Biochemistry
Duquesne University
(Committee Member)

Jenifer Aitken, Ph.D.
Associate Professor of Chemistry and
Biochemistry
Duquesne University
(Committee Member)

Di Gao, Ph.D.
Associate Professor, Chemical and
Petroleum Engineering
University of Pittsburgh
(External Reviewer)

Philip Reeder, Ph.D.
Dean, Bayer School of Natural
and Environmental Sciences
Duquesne University

Ralph Wheeler, Ph.D.
Chair, Department of Chemistry and
Biochemistry
Professor of Chemistry and Biochemistry
Duquesne University

ABSTRACT

OXIDE BASED EARTH ABUNDANT SEMICONDUCTORS AND OXYGEN EVOLVING CATALYSTS FOR PHOTOELECTROCHEMICAL AND PV DRIVEN WATER SPLITTING

By

Mourad Frites

December 2013

Dissertation supervised by: Dr. Shahed U. M. Khan

In the first part of this dissertation , photosplitting of water on the surface of semiconductor electrodes was investigated. Stability consideration favors metal oxide based semiconductors, hence titania and iron oxide were selected. High band gap for n -TiO₂ and low charge carrier mobility for n -Fe₂O₃ hinders their utilization for efficient water splitting. To enhance the spectral response of these semiconductors, nonmetal impurities such as hydrogen and carbon were used as doping elements. Hydrogen modification of n -TiO₂ was carried out by cathodic reduction of rutile thin film in basic electrolyte under dark conditions. Carbon modification of n -TiO₂ and n -Fe₂O₃ was carried out by flame oxidation of a clean Ti and Fe substrates where the carbon source is the combustion products of CH₄ and O₂. Flame temperature and gas flow rates were optimized. Iron oxide suffers high recombination rate of the photogenerated electron-

hole pair. To overcome this limitation, n -Fe₂O₃ nanowires were successfully synthesized by thermal oxidation of Fe metal sample under optimum oxidation temperature and time.

Inspired by the natural photosynthesis, in the second part, leaf-like amorphous silicon (a-Si) based photo-electrochemical cells (PECs) were synthesized for monolithic water splitting. The fundamental limitation of silicon, such as instability in electrolyte solution, was overcome by covering a-Si with TiO₂ as a visible light transparent thin film. While a-Si provides the necessary photovoltage, TiO₂ layer protects a-Si and provides the favorable valence band for water oxidation. These PECs were further protected by an ultra-thin film of Mn-oxide for long term operations.

In the third part, solar driven water electrolysis to generate H₂ was investigated. In this study we particularly investigated transition metal oxides such as porous Ni-Co₃O₄ and Ni-Co-mixed oxides as efficient oxygen evolving catalysts. The synthesis of the highly porous Ni-Co₃O₄ electrodes was carried out by mixing an appropriate amount of Ni and Co₃O₄ powders. Spray pyrolysis was used for the synthesis of transition metal mixed oxides on a conductive substrate, this was carried out by mixing different volume ratios of Ni(NO₃)₂ and Co(NO₃)₂ aqueous solutions. The activity of these transition metal oxides thin films was investigated for oxygen evolution during water electrolysis.

DEDICATION

To my wife Ibtisam, and my precious daughter Yasmine.

ACKNOWLEDGMENT

I would like to give my sincere thanks to my dissertation advisor, Dr. Shahed U. M. Khan, for his valuable supervision, continual guidance, support, and advice for 5 years. He has been an inspiration to me, and I have learned so much from him. I am so grateful for his time and patience with me throughout all steps towards the completion of this dissertation.

I would also like to thank my dissertation committee members, Dr. Ellen Gawalt, Dr. Jennifer Aitken, and Dr. Di Gao, who accepted to oversee this dissertation.

I would also like the entire faculty members in the Department of Chemistry and Biochemistry for their support.

Additionally, I would like to thank Dan Bodnar, Dave Hardesty, Lance Crosby and Benjamin Lauterbach for their technical expertise and instrumental maintenance. Also, Mr. Ian Welsh and the departmental office staff, Amy Stroyne, Sandy Russell and Margaret N. Cowburn for their help in laboratory and administration needs.

I gratefully acknowledge University of Toledo and U. S. Air Force for the financial support of part of this work.

TABLE OF CONTENTS

	Page
Abstract.....	vi
Dedication.....	vii
Acknowledgment.....	viii
List of Figures.....	xii
Chapter 1: Introduction.....	1
1.1 Water splitting on the surface of semiconductor electrodes.....	3
1.1.1 Water splitting on the surface of titanium oxide thin film electrode.....	8
1.1. 2 Water splitting on the surface of iron oxide thin film electrode.....	11
1.2 Monolithic solar water splitting	13
1.3 Solar driven water electrolysis.....	16
1.4 Research Focus.....	19
Chapter 2: Experimental.....	20
2.1 Synthesis of Hydrogen modified (HM-) n -TiO ₂ thin films.....	20
2.2 Synthesis of carbon modified (CM-) n -TiO ₂ thin films by thermal flame oxidation.....	21
2.3 Synthesis of nanostructured n -TiO ₂ thin films	22
2.4 Surface modification of n -TiO ₂ and CM- n -TiO ₂ , thin films by metal islets.....	23
2.5 Synthesis of iron oxide n -Fe ₂ O ₃ nanowires and carbon modified (CM-) n -Fe ₂ O ₃ thin films.....	24
2.6 Measurements of photocurrent density.....	24
2.7 Solar simulated light source.....	26
2.8 Fabrication of a self-driven a-Si based photoelectrochemical cell (PEC).....	28

2.8.1 Deposition of visible light transparent TiO ₂ on Tj-a-Si.....	28
2.8.2 Deposition of manganese oxide layer on TiO ₂ covered Tj-a-Si solar cel.....	29
2.8.3 Hydrogen gas collection at Pt cathode in Mn-oxide-TiO ₂ coated Tj-a-Si /Pt PEC	30
2.9 Synthesis of Ni-Co ₃ O ₄ porous electrode	31
2.10 Synthesis of Co-oxide and Ni-Co-mixed oxide thin films electrodes.....	34
2.11 Scanning Electron Microscopy (SEM) and energy dispersive spectroscopy (EDS) measurements.....	35
2.12 UV-Vis spectroscopic measurements.....	36
2.13 X-ray and XPS characterization of oxide thin films.....	36
Chapter 3: Results and Discussion.....	37
3.1 Hydrogen modified (HM)<i>n</i>-TiO₂ thin film electrodes.....	37
3.1.1 Photoresponse of HM- <i>n</i> -TiO ₂ thin film electrodes.....	37
3.1.2 Characterization of HM- <i>n</i> -TiO ₂ thin films using spectroscopic methods.....	41
3.1.3 Monochromatic photocurrent of HM- <i>n</i> -TiO ₂ thin films electrodes	44
3.1.4 Band gap energy of HM- <i>n</i> -TiO ₂ thin films.....	46
3.1.5 Summary.....	47
3.2 Carbon modified (CM)<i>n</i>-TiO₂ thin film electrodes.....	47
3.2.1 Surface morphology and structure characterization of <i>n</i> -TiO ₂ and CM- <i>n</i> -TiO ₂ thin films.....	47
3.2.2 Elemental analysis of CM- <i>n</i> -TiO ₂ thin film using EDS.....	48
3.2.3 X-ray diffraction (XRD) of CM- <i>n</i> -TiO ₂ and <i>n</i> -TiO ₂ thin films	50
3.2.4 Photoelectrochemical water splitting at CM- <i>n</i> -TiO ₂ thin film electrodes under an external minimal bias.....	51

3.2.5 Photoconversion efficiency of water splitting at CM- <i>n</i> -TiO ₂ and <i>n</i> -TiO ₂ thin film electrodes under an external minimal bias.....	55
3.2.6 Monochromatic photocurrent density for CM- <i>n</i> -TiO ₂ and <i>n</i> -TiO ₂	58
3.2.7 Diffuse reflectance spectra of CM- <i>n</i> -TiO ₂ and <i>n</i> -TiO ₂ thin films.....	60
3.2.8 Band gap energy of CM- <i>n</i> -TiO ₂ thin films.....	61
3.2.9 AC impedance spectroscopy: flat band potential and doping densities of CM- <i>n</i> -TiO ₂ and <i>n</i> -TiO ₂ thin films.....	62
3.2.10 Effect of surface modification by metal islets on the photocatalytic activity of CM- <i>n</i> -TiO ₂ thin film electrodes.....	67
3.2.11 Surface morphology of CM- <i>n</i> -TiO ₂ and metal islet decorated CM- <i>n</i> -TiO ₂ thin films	67
3.2.12 Photocatalytic activity of CM- <i>n</i> -TiO ₂ and metal islets decorated CM- <i>n</i> -TiO ₂ thin film electrodes.....	69
3.2.13 Effect of surface morphology on the photoactivity of <i>n</i> -TiO ₂ and CM- <i>n</i> -TiO ₂ thin film electrodes.....	71
3.2.14 Summary.....	74
3.3 Iron oxide nanowires and carbon modified (CM)<i>n</i>-Fe₂O₃ thin films for photoelectrochemical water splitting.....	75
3.3.1 Surface morphology of <i>n</i> -Fe ₂ O ₃ and CM- <i>n</i> -Fe ₂ O ₃ thin films.....	76
3.3.2 Photocurrent density of <i>n</i> -Fe ₂ O ₃ nanowires and CM- <i>n</i> -Fe ₂ O ₃ thin films under a minimal external bias.....	77
3.3.3 Photoconversion efficiency of water splitting at <i>n</i> -Fe ₂ O ₃ nanowires and CM- <i>n</i> -Fe ₂ O ₃ thin films under a minimal external bias.....	79
3.3.4 Monochromatic photocurrent density of <i>n</i> -Fe ₂ O ₃ nanowires and CM- <i>n</i> -Fe ₂ O ₃	81
3.3.5 Band gap energy of CM- <i>n</i> -Fe ₂ O ₃ thin film.....	82
3.3.6 UV-Vis spectra of <i>n</i> -Fe ₂ O ₃ nanowires and CM- <i>n</i> -Fe ₂ O ₃ thin films.....	83

3.3.7 AC impedance spectroscopy: flat band potential and doping densities of $n\text{-Fe}_2\text{O}_3$ nanowires and CM- $n\text{-Fe}_2\text{O}_3$ thin films.....	84
3.3.8 Elemental analysis of $n\text{-Fe}_2\text{O}_3$ nanowires and CM- $n\text{-Fe}_2\text{O}_3$ thin films using EDS	86
3.3.9 X-ray diffraction (XRD) patterns of $n\text{-Fe}_2\text{O}_3$ nanowires and CM- $n\text{-Fe}_2\text{O}_3$ thin films.....	87
3.3.10 Summary.....	88
3.4 Monolithic water splitting and artificial photosynthesis.....	89
3.4.1 Current-Voltage (I-V) curve for Tj-a-Si solar cell.....	90
3.4.2 Volumes of H_2 gas collected using Mn-oxide - TiO_2 coated Tj-a-Si solar cell based PEC.....	93
3.4.3 Solar to hydrogen efficiency, %STHE.....	94
3.4.4 Stability of Mn-oxide- TiO_2 coated Tj-a-Si solar cell based PEC in the electrolyte Solution.....	95
3.4.5 Summary.....	96
3.5 Water electrolysis.....	96
3.5.1 Optimum power for water electrolysis.....	96
3.5.2 Earth abundant electrocatalyst for oxygen evolution reaction (OER).....	101
3.5.2.1 Development of earth abundant and high performance porous catalyst for oxygen generation for solar driven water electrolysis	101
3.5.2.2 Catalytic activity of Ni-Co-mixed oxide toward OER under an external bias.....	104
3.5.3 Summary.....	109
References.....	110

LIST OF FIGURES

	Page
1.1 Primary energy uses by end-use sector, 2010-2035 (quadrillion Btu).....	2
1.2 Photo-electrochemical cell (PEC) for water splitting using: a) <i>n</i> -type photoactive semiconductor and Pt counter electrode; b) <i>p</i> -type photoactive semiconductor and Pt counter electrode; c) tandem electrochemical cell.....	4
1.3 Band gap energy for different semiconductors.....	6
1.4 Pourbaix diagram for water splitting.....	7
1.5 Monolithic water splitting electrochemical cell.....	14
1.6 Spectral response for monocrystalline silicon (Mono-Si) and amorphous silicon (a-Si).....	15
1.7 Solar driven water electrolysis	17
1.8 Volcano plot for oxygen evolution over metal oxide electrodes versus enthalpy of the transition from lower oxide to higher oxide in acidic (filled squares) and basic mediums (unfilled squares).....	19
2.1 Thermal flame oxidation of Ti metal sample for the synthesis of CM-n-TiO ₂	22
2.2 Hydrothermal treatments of Ti metal samples.....	23
2.3 Spectral response of the silicon detector: model 10DP/SB.....	25
2.4 Photocurrent density measurements by subtracting the dark current density from the illumination current density.....	26
2.5 Solar simulator spectrum compared to spectral irradiance air mass 1.5, Orion Data: the spectral data obtained from the manufacturer, Solar Simulator lab: spectral data measured in the lab using Si detector (model-DP/SB), 1.5 Global: full spectrum of the solar light obtained from NREL.....	28
2.6 Photocurrent density of TiO ₂ covered Tj-a-Si versus the number of drops of TiO ₂	29
2.7 Curing Mn(OH) ₂ deposited on TiO ₂ covered Tj-a-Si under vacuum.....	30
2.8 Water splitting using a self driven monolithic a-Si based PEC.....	31

2.9	Sintering temperature profile for porous Ni-Co ₃ O ₄ electrode	32
2.10	Fluid pore filling porosity measurement for Ni-Co ₃ O ₄ electrode	33
2.11	Spray pyrolysis apparatus used to synthesis Ni-Co mixed oxides Co monoxide catalysts	35
3.1	Photoelectrochemical cell under light and under external bias for water splitting.....	37
3.2	Photocurrent density of undoped <i>n</i> -TiO ₂ and HM- <i>n</i> -TiO ₂ thin film electrodes as a function of measured potential in 2.5 M KOH electrolyte and under 0.1 W cm ⁻² solar simulated light	38
3.3	Cycling tests for HM- <i>n</i> -TiO ₂ in terms of photocurrent density, J _p (mA cm ⁻²) under the same experimental conditions as was specified earlier in the experimental sections. Each curve is defined in the plot's legend from d1 (day 1) to d30 (day 30).....	39
3.4	Cycling tests for HM- <i>n</i> -TiO ₂ in terms of photocurrent density, J _p (mA cm ⁻²) after drying the electrode at 100°C, 150°C and 200°C, respectively.....	40
3.5	Photocurrent density of HM- <i>n</i> -TiO ₂ , the dried HM- <i>n</i> -TiO ₂ at 200°C and the rehydrogenated HM- <i>n</i> -TiO ₂ thin film electrodes as a function of applied potential in 2.5 M KOH electrolyte and under 0.1Wcm ⁻² solar simulated light.....	41
3.6	Top view SEM images for HM- <i>n</i> -TiO ₂ thin films and regular <i>n</i> -TiO ₂ thin films before reduction.....	42
3.7	Xray diffraction (XRD) patterns for <i>n</i> -TiO ₂ and HM- <i>n</i> -TiO ₂ thin films compared to reference patterns of Rutile (03-065-0192, 01-077-0443); Anatase (01-086-1156, 01-086-1155); and Ti (01-089-5009).....	43
3.8	Valence band X-ray photoelectron spectroscopy (XPS) spectra for regular <i>n</i> -TiO ₂ and HM- <i>n</i> -TiO ₂	43
3.9	Monochromatic photocurrent density, j _p (λ), as a function of wavelength of light, λ, for unmodified <i>n</i> -TiO ₂ and HM- <i>n</i> -TiO ₂ . The monochromatic photocurrent measurements were performed under monochromatic light intensity of 0.1W cm ⁻² from a global AM 1.5 solar simulator and 2.5 M KOH as electrolyte. The measured potential used was set at 0.2 V/SCE.....	45
3.10	Conduction band inversion at the interface <i>n</i> -type semiconductor – electrolyte when a negative bias is applied.....	45

3.11	The respective plots of $(\eta h\nu)^{1/2}$ vs. $(h\nu)$ to determine the band gap of HM- <i>n</i> -TiO ₂ and undoped <i>n</i> -TiO ₂ thin films. The measurements were performed under monochromatic light with an intensity of 0.1 W cm ⁻² from a global AM 1.5 solar simulator and 2.5 M KOH as electrolyte.....	46
3.12	Top view SEM images of flame oxidized CM- <i>n</i> -TiO ₂ thin films and undoped <i>n</i> -TiO ₂ thin films.	48
3.13	Hyper map and EDS spectra of CM- <i>n</i> -TiO ₂ and <i>n</i> -TiO ₂ showing the surface elemental distribution.....	49
3.14	Elemental mapping for CM- <i>n</i> -TiO ₂ thin film over a large cross sectional area (low magnification) With red for Ti atoms, blue for O atoms and green for C atoms...50	
3.15	Xray diffraction (XRD) patterns for <i>n</i> -TiO ₂ and CM- <i>n</i> -TiO ₂ thin films compared to reference patterns of Rutile (03-065-0192, 01-073-1765); Anatase (01-086-1156, 01-086-1157); and Ti (01-089-5009).....	51
3.16	Photocurrent density as a function of measured potential, E_{meas} (V/SCE) under light intensity of 0.1 W cm ⁻² from a global AM 1.5 solar simulator and in 5 M KOH electrolyte, (a) Photocurrent density for <i>n</i> -TiO ₂ (b) Photocurrent density for CM- <i>n</i> -TiO ₂	54
3.17	Photocurrent density as a function of measured potential, E_{meas} (V/SCE) for CM- <i>n</i> -TiO ₂ thin film electrodes synthesized by thermal flame oxidation at the optimum condition of flame temperature and different oxidation times. The measurements were performed under light a intensity of 0.1 W cm ⁻² from a global AM 1.5 solar simulator, and in 5 M KOH electrolyte.....	55
3.18	Photoconversion efficiency as a function of applied potential E_{app} (V/ E_{aoc}) under light intensity of 0.1 W cm ⁻² from a global AM 1.5 solar simulator in a 5 M KOH electrolyte. Curve (a): <i>n</i> -TiO ₂ and curve (b): CM- <i>n</i> -TiO ₂	58
3.19	The monochromatic photocurrent density, $j_p(\lambda)$, as a function of the wavelength, λ (nm), for undoped <i>n</i> -TiO ₂ and CM- <i>n</i> -TiO ₂ . The monochromatic photocurrent measurements were performed under a light intensity of 0.1 W cm ⁻² from a global AM 1.5 solar simulator in 5 M KOH electrolyte. The measured potential used was 0.1 V/SCE.....	59
3.20	Diffuse reflectance spectra for undoped <i>n</i> -TiO ₂ and CM- <i>n</i> -TiO ₂	60
3.21	The respective plots of $(\eta h\nu)^{1/2}$ vs. $(h\nu)$ to determine the band gap of CM- <i>n</i> -TiO ₂ and undoped <i>n</i> -TiO ₂ thin films. The measurement were performed under a light intensity of 0.1 W cm ⁻² from a global AM 1.5 solar simulator in 5 M KOH electrolyte.....	61

3.22	Nyquist plot for CM- <i>n</i> -TiO ₂ and <i>n</i> -TiO ₂ thin films electrodes measured in 2.5 M KOH in dark conditions with the equivalent RC circuit.....	64
3.23	Mott-Schottky plot of <i>n</i> -TiO ₂ and CM- <i>n</i> -TiO ₂ thin films measured at various AC frequencies. 10 mV AC amplitude, 2.5 M KOH electrolyte measured in the dark.....	66
3.24	SEM picture for: a) CM- <i>n</i> -TiO ₂ before metal islets electrodeposition b) CM- <i>n</i> -TiO ₂ after Ru islets electrodeposition (bright spots for the metal islets and clusters).....	68
3.25	Photocurrent density (j_p , mA cm ⁻²) versus measured potential (V_{meas} , V/SCE) for: ◆— Ru metal islet decorated CM- <i>n</i> -TiO ₂ ●-- Bare CM- <i>n</i> -TiO ₂ electrodes. Note that the bare CM- <i>n</i> -TiO ₂ samples are not highly optimized.....	70
3.26	Top view SEM picture: (a) Ti metal sample (left) after hydrothermal treatment in 5% HCl solution at 180°C for 10 hours and (b) higher magnifications	72
3.27	Photocurrent density as a function of measured potential, E_{meas} (V/SCE), for CM- <i>n</i> -TiO ₂ thin film synthesized from a flat Ti sample and CM- <i>n</i> -TiO ₂ thin film synthesized from an etched Ti sample. The photocurrent measurement was carried out under light intensity of 0.1 W cm ⁻² from a global AM 1.5 solar simulators, and 2.5 M KOH electrolyte.....	73
3.28	Top view SEM picture (a) Ti metal sample (left) after hydrothermal treatment in 5% HCl solution at 180°C for 10 hours and (b) CM- <i>n</i> -TiO ₂ thin film synthesized by thermal flame oxidation of the etched Ti metal sample at the optimum condition of flame temperature and time, 825°C and 15 min, respectively.....	74
3.29	Top and side view SEM images for <i>n</i> -Fe ₂ O ₃ nanowires. Top view SEM image of <i>n</i> -Fe ₂ O ₃ flat sample, and flame oxidized CM- <i>n</i> -Fe ₂ O ₃ thin films.....	76
3.30	Photocurrent densities as a function of measured potential, E_{meas} (V/SCE), for <i>n</i> -Fe ₂ O ₃ nanowires and <i>n</i> -Fe ₂ O ₃ flat sample under light intensity of 0.1 W cm ⁻² from a global AM 1.5 solar simulator in 5 M KOH electrolyte.....	78
3.31	Photocurrent density as a function of measured potential, E_{meas} (V/SCE), for <i>n</i> -Fe ₂ O ₃ nanowires and CM- <i>n</i> -Fe ₂ O ₃ thin film electrodes under light intensity of 0.1 W cm ⁻² from a global AM 1.5 solar simulator in 5 M KOH electrolyte.....	79
3.32	Photoconversion efficiency for <i>n</i> -Fe ₂ O ₃ and CM- <i>n</i> -Fe ₂ O ₃ as a function of applied potential E_{app} (V/E_{aoc}) under light intensity of 0.1 W cm ⁻² from a global AM 1.5 solar simulator in 5 M KOH electrolyte.....	80
3.33	Monochromatic photocurrent density, $j_p(\lambda)$, as a function of wavelength of light, λ (nm), for <i>n</i> -Fe ₂ O ₃ nanowires and CM- <i>n</i> -Fe ₂ O ₃ thin film electrodes. The	

	monochromatic photocurrent measurements were performed under light intensity of 0.1 W cm^{-2} from a global AM 1.5 solar simulator in 5 M KOH electrolyte.....	81
3.34	The respective plots of $(\eta h\nu)^{1/2}$ vs. $(h\nu)$ to determine the band gap of $n\text{-Fe}_2\text{O}_3$ nanowires and CM- $n\text{-Fe}_2\text{O}_3$. The measurement were performed under a light intensity of 0.1 W cm^{-2} from a global AM 1.5 solar simulator in 5 M KOH electrolyte.....	82
3.35	UV-Vis spectra for $n\text{-Fe}_2\text{O}_3$ and CM- $n\text{-Fe}_2\text{O}_3$	83
3.36	Mott-Schottky plot of $n\text{-Fe}_2\text{O}_3$ nanowires and CM- $n\text{-Fe}_2\text{O}_3$ thin films measured at various AC frequencies. 10 mV AC amplitude, 2.5 M KOH electrolyte measured in dark.....	85
3.37	EDS spectra of CM- $n\text{-Fe}_2\text{O}_3$ thin films showing the surface elemental composition.....	86
3.38	EDS spectra of $n\text{-Fe}_2\text{O}_3$ nanowires thin film showing the surface elemental composition.....	87
3.39	Xray diffraction (XRD) patterns for iron oxide (nanowires) and carbon modified iron oxide (CM- $n\text{-Fe}_2\text{O}_3$) thin films compared to the reference patterns of Fe_2O_3 (01-072-0469, 01-087-1165); Fe_3O_4 (01-089-0691, 01-087-2334); Fe (00-003-0968, 01-089-0690) and Fe (00-006-0669).....	88
3.40	Schematic diagram of the monolithic leaf-like Mn-oxide - TiO_2 coated Tj-a-Si PEC. The diagram demonstrates the self-driven generation of oxygen on the light illuminated (1 sun) Mn-oxide - TiO_2 coated Tj-a-Si surface and hydrogen gas on the dark stainless steel (SS) surface during water splitting in 2.5 M KOH electrolyte.....	90
3.41	Top view SEM picture of TiO_2 coated Tj-a-Si and Mn-oxide- TiO_2 coved Tj-a-Si solar cell.....	91
3.42	Plots of photocurrent density and cell power density versus photovoltage for Tj-a-Si solar cell to determine the maximum photovoltage (V_{max}) at a maximum power.....	92
3.43	XRD patterns acquired from the as-prepared Mn-oxide film. Patterns for Mn_2O_3 are observed and compared to PDF 01-071-0636; patterns for Mn_3O_4 are also observed and compared to PDF 00-001-1127, as shown.	92
3.44	Volumes of Hydrogen gas (mL) collected versus time (min). In the inset a fitting line was drawn for the linear part of the plot of the volumes of H_2 evolved per cm^2 of photoactive Tj-a-Si surface of area 0.69 cm^2 versus time.....	93

3.45	Hydrogen current vs time plots for different powers (P) supplied to electrochemical cell from the power supply (the areas of the Pt anode and Pt cathode were 0.69 cm ² and 4.25 cm ² respectively).....	98
3.46	The effect of the applied voltage on hydrogen current at similar powers but different voltages from the power supply (the areas of the Pt anode and Pt cathode were 0.69 cm ² and 4.25 cm ² respectively).....	98
3.47	The effect of high voltages from a Power Supply on hydrogen currents (the areas of the Pt anode and Pt cathode were 0.69 cm ² and 4.25 cm ² respectively).....	99
3.48	Hydrogen current density vs time plots for power supplied from solar cell 1, 2, and 3 under solar simulated light intensity of 0.1 mW cm ⁻² (the areas of the Pt anode and Pt cathode were 0.69 cm ² and 4.25 cm ² respectively).....	100
3.49	I-V curves for the three solar cells used to power the electrochemical cell during water splitting. The photoactive areas of solar cell 1, 2 and 3 used were 9.6 cm ² , 5.0 cm ² and 6.2 cm ² respectively.....	100
3.50	Top view SEM image of porous Ni-Co ₃ O ₄	102
3.51	Current density, J (mA cm ⁻²) versus cell voltage (Volt) and cell power density, P (mW cm ⁻²) for the Dj-a-Si solar cell under solar simulated light intensity of 0.1 Wcm ⁻²	104
3.52	Current density, J (mA cm ⁻²) versus applied potential (E, V/SCE) for oxygen evolution reaction (OER) during water splitting in 2.5 M KOH electrolyte solution showing the highest activity for Ni-Co ₂ O ₃ mixed oxide with a ration of Ni/Co = 3.....	105
3.53	Current density, J (mA cm ⁻²) versus applied potential (E, V/SCE) for oxygen evolution reaction (OER) during water splitting in 2.5 M KOH electrolyte solution showing the highest activity for Ni-Co-mixed oxides compared to Co-oxide and bare FTO coated conducting glass.....	106
3.54	Cyclic voltammetry plots for Ni-Co-mixed oxide with optimum composition, Co-oxide, Ni-oxide deposited on FTO coated glass substrate in 2.5 M KOH electrolyte.....	107
3.55	Tafel plots obtained from the I-V (current density I and potential, V) curve during OER on Ni-Co mixed oxide and Co-oxide thin films. The overpotentials for OER were obtained using $\eta = E_{app} - 0.116$ where E_{app} is the measured potential at the electrode during OER.	108
3.56	SEM Pictures of (A) Co-oxide on FTO coated glass substrate (B) Ni-Co-mixed oxide on FTO coated glass substrate (c) Porous Ni-Cobalt oxide plate.....	109

Chapter 1

Introduction

The world is in an urgent need to develop a renewable and carbon neutral source of energy to mitigate the world's growing dependence on fast depleting fossil fuel as the primary energy source.¹ Fossil fuel burning generates carbon footprint and harmful products. Carbon dioxide contributes to the global warming; SO₂, NO_x and mercury released from power plant are directly associated with acid rain, acid mine drainage and aquatic pollution.^{2, 3, 4, 5} Nuclear power plant is considered as a perfect emission free energy source; however, the unsolvable long term storage of nuclear wastes and the unpredictable radioactive leaks during natural or man-made disasters make it an unpopular solution to the future energy shortage. Converting solar energy to hydrogen fuel by water splitting offers an alternative energy solution to overcome the predictable energy crisis.¹

Hydrogen is an energy carrier and not an energy source and has many advantages over electricity. Hydrogen can be stored more effectively and reconverted to electricity when needed by combining it with the atmospheric O₂ in fuel cells. In this process and in burning hydrogen the only product is water which makes it carbon neutral and environmentally friendly.

Currently hydrogen gas extracted from fossil fuel is being used in ammonia and methanol production plants as syngas. In the future the use of H₂, produced from clean and renewable sources, will be also used to power fuel cell vehicles (FCVs) and stationary fuel cells for electricity generation.⁶ Transportation (public or private), which accounts for about 25% of total energy consumption in the United State, as shown in

figure 1.1⁷, is one of the main sectors that will benefit from a potential hydrogen economy. The use of hydrogen to power fuel cell vehicles (FCVs) will cut down on CO₂ emissions and mitigate the effect of global warming. More importantly fuel cells avoid the fundamental limitation of the Carnot Cycle in converting chemical energy to electrical energy. As a result this makes it more efficient than any other internal combustion engine, which would help reduce fuel consumption and significantly alleviate the burden on drivers tight budget.^{8, 9, 10}

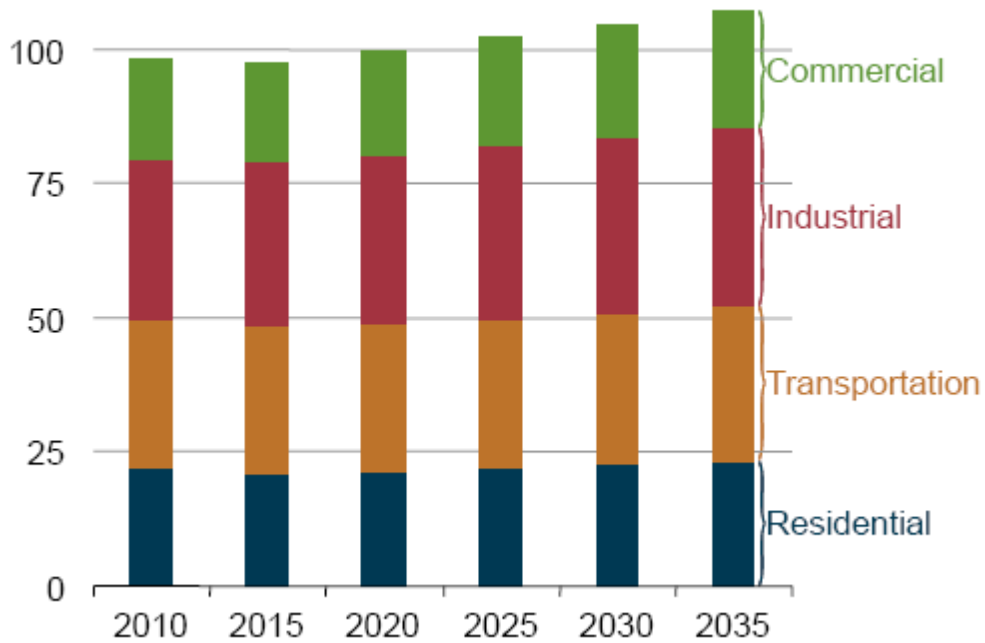


Figure 1.1 Primary energy uses by end-use sector, 2010-2035 (quadrillion Btu).⁷

Solar energy is a naturally occurring and omnipresent. Although it is difficult to harvest, it can be efficiently converted into a sustainable hydrogen fuel. Solar energy conversion to H₂ fuel includes: a) photoassisted water splitting on the surface of semiconductor electrodes. b) solar driven water electrolysis on the surface of an oxygen

evolving catalyst where photovoltaic (PV) solar cells are used to harvest the energy of the photons and supply the necessary photovoltage to drive the water splitting reaction.

1.1 Water splitting on the surface of semiconductor electrodes:

Converting solar energy to H₂ fuel by photoelectrochemical splitting of water on the surface of semiconductor electrodes was first demonstrated in the early 1970s during the oil crisis. Honda and coworkers¹¹ demonstrated the photoelectrochemical splitting of water under UV light in an electrochemical cell with the use of TiO₂ as the photoanode and a Platinum (Pt) wire as a the counter electrode. Since then their work has been investigated intensively during past decades.^{12, 13, 14, 15} Further investigations are expected to overcome the growing dependence on the fast-depleting fossil fuel as the primary energy source and to minimize the devastating effects of global warming caused mainly by the burning of fossil fuel.

A typical photoelectrochemical cell (PEC) for water splitting consists of a semiconductor electrode as the photoanode (*n*-type), and a counter metal electrode as the cathode Figure 1.2 a; Platinum metal (Pt) is the most suitable cathode among all metals due to its intrinsic property of fast kinetics for hydrogen evolution reaction (HER). Other metals such as nickel (Ni) can be also used as cathodes, where their slow hydrogen reduction kinetics compared to Pt is offset by the high price of the precious metal (Pt). When a *p*-type semiconductor is used in the PEC (Fig. 1.2 b) then the working electrode would be the photocathode. In another PEC configuration, better known as a self-driven tandem cell (see Fig. 1. 2 c), both anode and cathode are photoactive and therefore exposed to the same light illumination. In this configuration oxygen evolves on the

surface of the *n*-type semiconductor (anode) and hydrogen evolves on the surface of the *p*-type semiconductor (cathode), and no bias is necessary since both oxidation and reduction reactions are driven by the energy of the absorbed light.

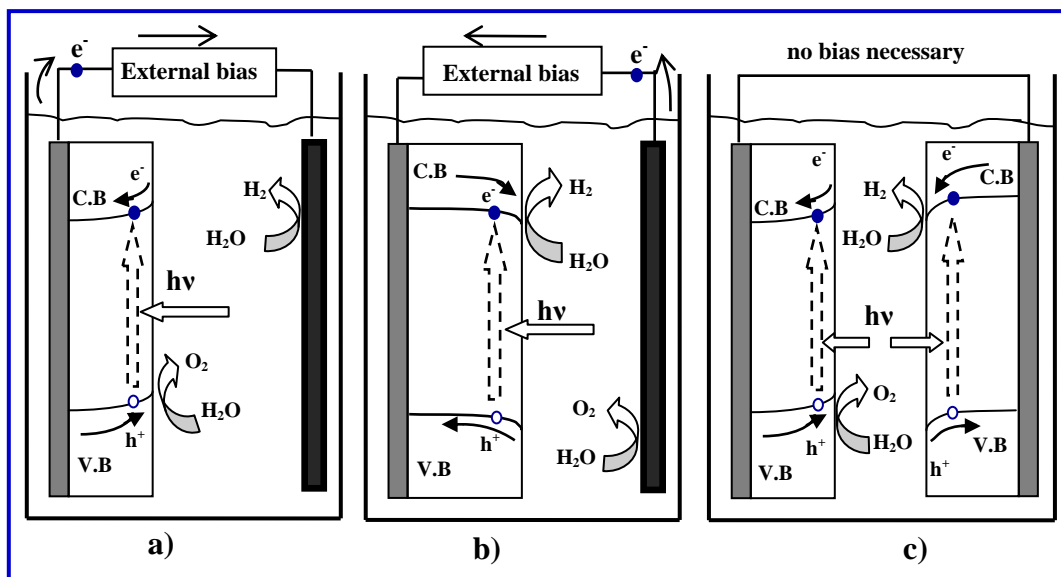
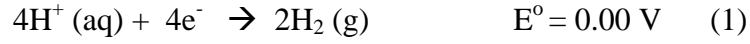


Figure 1.2 Photo-electrochemical cell (PEC) for water splitting using: a) *n*-type photoactive semiconductor and Pt counter electrode; b) *p*-type photoactive semiconductor and Pt counter electrode; c) tandem electrochemical cell.

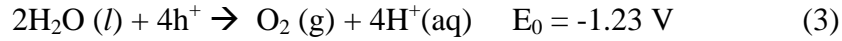
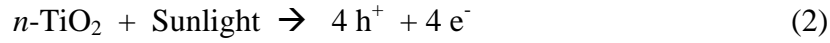
When a semiconductor such as *n*-TiO₂ is irradiated, the photoactivity of the semiconductor is initiated by absorption of photons with energy ($E = h\nu$) equal to or greater than the band gap (3 eV for rutile and 3.2 eV for anatase)¹⁶ a small fraction of electrons and holes are generated. Depending on the density of states, only a fraction of these charge carriers arrive at the surface where they react with the adsorbed molecules or ions. Water splitting on the surface of semiconductor electrodes can be carried out in acidic or basic mediums; however, stability considerations favor basic media when metal oxide electrodes are used as anodes. The reaction steps involved in photoelectrochemical cell with *n*-TiO₂ as anode are:

In acidic media:

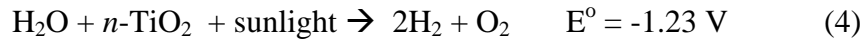
At dark cathode (e.g. Pt metal):



At a photoactive anode ($n\text{-TiO}_2$)

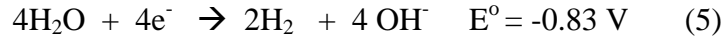


Addition of reactions (1), (2), and (3) gives the overall water splitting reaction on the surface of $n\text{-TiO}_2$ electrode under sunlight illumination in aqueous acidic media as,

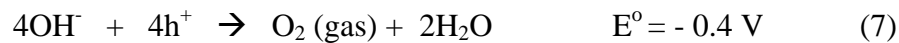
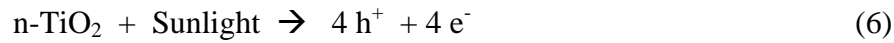


In basic medium:

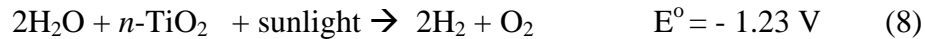
At dark cathode (e.g. Pt metal)



At a photoactive anode ($n\text{-TiO}_2$)



Addition of reactions (5), (6), and (7) gives the overall water splitting reaction on the surface of $n\text{-TiO}_2$ electrode under sunlight illumination in aqueous basic media as,



The first consideration in using semiconductors for water splitting is their band gap; under illumination the semiconductor must generate an intrinsic photovoltage higher

than the standard redox potential (1.23V) plus ohmic, thermodynamic and kinetic barriers for the water splitting reaction. Thus an optimized band gap is required for maximum absorption of sun light and must be larger than the energy required to split water molecules (1.23 eV). Furthermore, the band gap edges position must straddle the oxygen and hydrogen evolution potentials (see figure 1.3),¹⁷ so that the photogenerated holes (h^+) in the valance band are more positive than the oxygen evolution potential and the photogenerated electrons (e^-) in the conduction band are more negative than the hydrogen evolution potential. The second consideration in PEC applications for water splitting is the chemical stability of the semiconductor electrodes in basic or acidic electrolytes.

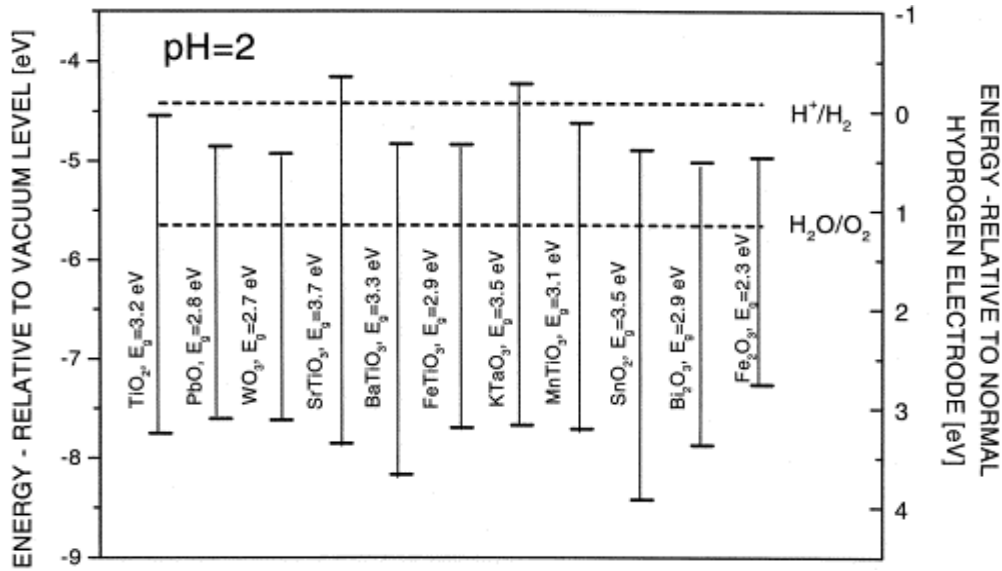


Figure 1.3 Band gap energy for different semiconductors.¹⁷

Note that in Figure 1.3 the water splitting reaction is given in acidic medium (pH = 2), which implies that the values of potentials for oxygen and hydrogen evolution change with the pH of the electrolyte. In fact, potentials for oxygen and hydrogen

evolution are pH dependent and the relationship was found to be Nerstian according to equations (9) and (10). Potentials here are given with respect to the normal hydrogen electrode (NHE):

Nurstian H_2 evolution potential:

$$E_{\text{cathode}} = 0V - 0.059\text{pH V vs NHE} \quad (9)$$

Nurstian O_2 evolution potential:

$$E_{\text{anode}} = 1.23V - 0.059\text{pH V vs NHE} \quad (10)$$

Note that the difference of these two equations shows that at any given pH the water splitting potential is 1.23 V. The plot of the cathodic and anodic Nerstian potentials versus pH, results in what is commonly known as the Pourbaix diagram of water is shown in figure 1.4.

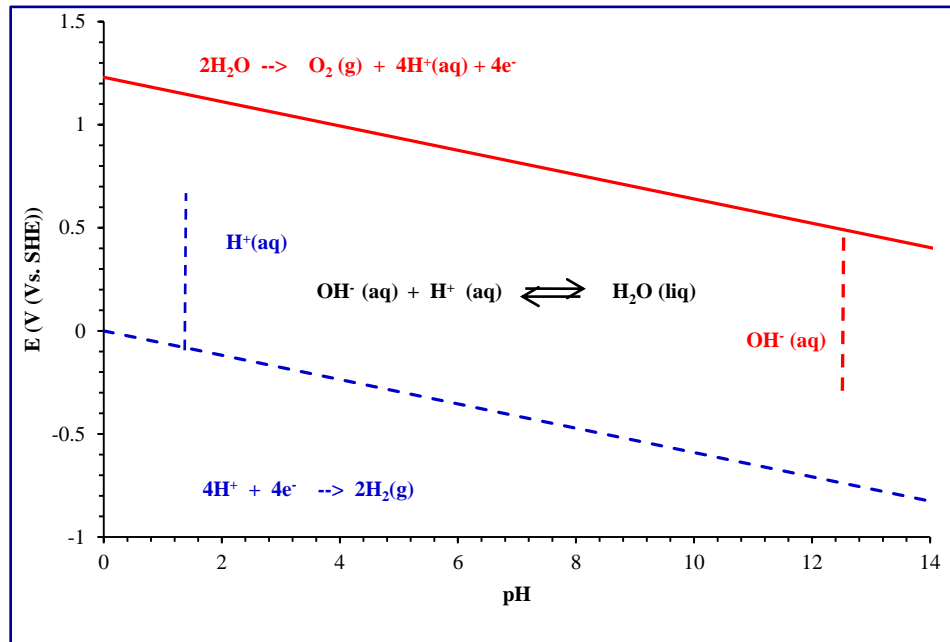


Figure 1.4 Pourbaix diagram for water splitting.

Photo dissolution of semiconductor electrodes and lack of efficient light absorption (high band gap for the most suitable ones) are the main challenges for efficient water splitting under solar light. Progress in research and development on efficient solar-to-fuel conversion largely depends on the development of new stable, photo-active and cost effective materials.

Stability consideration favors all inorganic oxide based materials for the oxygen evolution reaction (OER); hence, cost effective oxide based semiconductors appear to be the most promising materials for water splitting under solar light illumination. Moreover, their optical properties can be modified by the incorporation of impurities such as H, N, S, C, and transition metals in their crystalline structures.^{15, 18, 19, 20, 21, 13, 22} These impurities/dopants help to lower the band gap of these semiconductors, and thus extend their spectral response to the visible region of the solar spectrum. A large number of semiconductor photo-catalysts such as TiO_2 , Fe_2O_3 , WO_2 , and ZrO_2 have been reported for water splitting under artificial light.^{15, 22, 23, 24} In addition combinatorial chemistry offers a rapid growing field to design new catalysts such as multiple band gap semiconductor thin films that are synthesized by chemical vacuum deposition, sol-gel and spray pyrolysis.^{25, 26, 27}

1.1.1 Water splitting on the surface of Titanium Oxide thin film electrode:

Since the first investigation on water splitting over TiO_2 electrodes under UV light illumination,¹¹ numerous studies have been conducted on TiO_2 as the semiconductor catalyst of choice for water splitting due to the position of its band gap

vis-à-vis hydrogen and oxygen evolution potentials; however, its wide band gap hinders the efficient use of titania as a photo-anode for OER.

In spite of its chemical stability in electrolyte solutions, *n*-TiO₂ has serious disadvantages, the main one is due to its intrinsic band gap (3 eV (414 nm) for Rutile and 3.2 eV (387 nm) for anatase) which absorbs only the UV light that accounts for 3% of the solar radiation.²⁸ To increase the photoresponse of *n*-TiO₂ within the UV region and to shift its spectral response to include the visible region ($400\text{ nm} \leq \lambda \leq 800\text{ nm}$) is still an ongoing challenge in order to increase the utility of *n*-TiO₂ as a catalyst for water splitting. The best approach to meet this challenge is to dope *n*-TiO₂ with different elements (metal and nonmetals) and thus decrease its photo threshold energy. Transition metals have been used intensively as impurities dopands for *n*-TiO₂.^{13, 28, 29, 30, 31} Mixed results were reported about improving the spectral response of metal doped Titania.^{13, 28, 32, 33, 34} In some investigations the negative effects of using transition metals as dopants were attributed to the metal dopant atoms serving as a center for charge carrier recombination.^{13, 28} It turns out that visible light absorption in metal doped *n*-TiO₂ is due to the electronic transition within the conduction band (d-d transition) rather than band gap lowering.³⁵ It is also not known whether the deception caused by the use of transition metals was the reason for shifting the interest to nonmetallic elements as alternative dopants.

Recently nonmetallic elements such as carbon,^{15, 18} nitrogen,^{19, 13} sulfur,²¹ and hydrogen^{36, 37, 38} were used to dope *n*-TiO₂. Nitrogen doped *n*-TiO₂ was reported to be visible light active which according to Asahi et al¹⁹ is due to band gap narrowing. In contrast, the improved photoactivity of TiO_{2-x}N_x in the visible light is due to electronic

excitation from an isolated N 2p state, located above the native valence band edge O 2p state, to the conduction band rather than an excitation over a narrowed band gap.^{39, 40} Also, N doping was found to diminish UV light absorption in *n*-TiO₂.⁴¹ Hydrogen modification of *n*-TiO₂ was mainly achieved by heat treatment of amorphous Titania under a hydrogen gas stream.^{36, 37} And upon incorporation of hydrogen within the structure of *n*-TiO₂ the native white color of TiO₂ blackened. The spectral response of H-doped *n*-TiO₂ was found to shift to the visible part of the incident light used.^{37, 38}

The breakthrough in shifting the photo threshold energy of TiO₂ to visible light was achieved when carbon was used as dopant by Khan et al.¹⁵ The carbon modified *n*-TiO₂ (CM-*n*-TiO₂) showed enhancement of absorption in the UV region and also red shifted to the visible region. A natural gas flame was used in synthesizing carbon modified *n*-TiO₂. An efficiency of 8.35% under artificial light from Xenon lamp was reported for water splitting; a significant reduction of the band gap from 3.0 eV to 2.32 eV was also reported. Wet chemistry was investigated for the synthesis of CM-*n*-TiO₂ particles. CM-*n*-TiO₂ particles were synthesized by hydrolysis of a precursor solution of TiCl₄ or titanium tetraisopropoxide (TTIP) in the presence of tetrabutylammonium hydroxide, ethylene glycol or glucose as carbon sources.^{18, 42, 43} The photoactivity of CM-*n*-TiO₂ particles was evaluated as the rate of photo-degradation of organic compounds (e.g. methylene blue) under visible light illumination.⁴³ Khan et al.¹⁵ reported the presence of substitutionally bonded carbon which resulted in a new electronic state (mid band) within the forbidden band gap of native rutile. However, Kisch et al.¹⁸ reported the presence of elemental carbon or carbon-containing species. On the other hand theoretical investigations using DFT calculations by Di Valentin et al.

⁴⁴ indicated the possible existence of both substitutional and interstitial carbon in CM-*n*-TiO₂.

1.1.2 Water splitting on the surface of iron Oxide thin film electrodes:

Efficient production of hydrogen from a renewable and inexhaustible source, water, and the use of a stable semiconducting electrode under sunlight illumination is still of a paramount importance at the dawn of this twenty first century. Interestingly iron (III) oxide (Fe₂O₃) has the suitable properties to be used among other semiconductors for photoelectrochemical splitting of water to hydrogen and oxygen. It is abundant; low cost; environmentally friendly and it is stable in basic electrolytes. In addition, iron oxide has a band gap of 2–2.2 eV.⁴⁵ Therefore, it can absorb a considerable part of the solar light up to 620 nm which accounts for nearly 40% of the sunlight photons.^{45, 46, 47} These properties make it attractive to investigate the use of iron oxide as a photocatalyst for a massive production of hydrogen by photoelectrochemical water splitting.^{48, 49, 50, 51}

The photocatalytic activity of Fe₂O₃ is mainly hampered by its low charge carrier mobility, high resistivity and slow charge transfer across the interface. This leads to a high recombination probability of the photogenerated electron-hole pairs.⁴⁸ To minimize these limitations and improve the photoresponse of iron (III) oxides, the latter was doped with various metal and nonmetal dopants.^{49, 50, 51} Different methods were used for the synthesis of iron (III) oxide electrodes. These include pressing the polycrystalline Fe₂O₃ into a palette followed by sintering,^{52, 53} spray pyrolysis of a solution of Fe(NO₃)₃ or FeCl₃ on a hot conductive glass substrate,^{54, 22} and by chemical vapor deposition (CVD).

⁵⁵ Nevertheless, these iron oxide photoanodes exhibited a low photocurrent density during the water splitting reaction.

Silicon doped iron (III) oxide synthesized by ultrasonic spray was reported by Cezar et al.⁴⁹ During the photoelectrochemical splitting of water the Si doped Fe₂O₃ showed an enhancement of photocurrent density compared to the pristine Fe₂O₃. Hu et al.⁵⁶ investigated Pt metal as dopant for iron (III) oxide thin films. The Pt-doped Fe₂O₃ were prepared by electrochemical route and showed an enhancement in photocurrent density of 1.43 mA cm⁻² at a potential of 0.4 V vs Ag/AgCl compared to 0.69 mA cm⁻² for an undoped iron oxide sample under light illumination of 410 mW cm⁻².

Since carbon modification of *n*-TiO₂ photocatalyst showed a remarkable enhancement in its catalytic activity during water splitting under artificial light,¹⁵ carbon doping of iron oxide could play a significant role in modifying its optical and electrical behavior. Nanostructure morphologies of iron oxide thin films such as nanowires or nanorodes offer alternative option to circumvent some of the limitations due to the short photogenerated charge carriers lifetime or diffusion length.⁵⁷ The nanostructure surface morphology reduces the charge carriers transport distance to reach the oxidizing species at the semiconductor- electrolyte interface (h⁺) and increase the collection efficiency of electrons.⁵⁸ Due to light scattering within porous structures, a rough surface of iron oxide with nano-rodes, or nano-wires like structures would effectively increase light absorption and therefore a higher photocurrent is generated.

1.2 Monolithic solar water splitting:

The cost of converting solar energy to hydrogen can be minimized by the use a self-driven monolithic photoelectrochemical cell (PEC) that would eliminate the costs associated with separate construction and interconnection of solar cells and the electrochemical water electrolyzers. The concept is to develop a leaf-like water splitting PEC as shown in Figure 1.5 that would split water into hydrogen and oxygen under sunlight illumination. Such a process is promising with the use of semiconductors that generate enough electromotive force under sunlight illumination to drive the thermodynamically unfavorable water splitting reaction. Silicon based solar cells can satisfy this criteria of such PEC.

Since the first publication on amorphous silicon (a-Si) in the late 1960s,⁵⁹ a-Si has been considered as a promising material compared to the costly crystalline silicon based solar cells.⁶⁰ Furthermore, a-Si has a better photoresponse in the more energetic visible region of the solar spectrum than crystalline silicon which is most sensitive in the less energetic longer wavelengths (IR) region figure 1.6.^{59, 60} Triple junction amorphous silicon (Tj-a-Si) solar cells are generally used for electricity generation. However, stability issues of a-Si in aqueous electrolytes, its high valence band with respect to the oxygen oxidation potential, and its smaller band gap (1.2 eV) make it unfavorable for direct water splitting under solar light. These fundamental limitations can be surmounted by covering a-Si with a visible light transparent stable thin film. While a-Si provides the necessary power to drive the water splitting reaction under light illumination, the deposited thin film layer protects a-Si and provides the favorable valence band for water oxidation.

High band gap oxide based semiconductors are mostly transparent to visible light and stable in basic electrolytes. Such oxides can be used as a transparent conductive corrosion resistant (TCCR) layer to protect a-Si based solar cells in electrolyte solutions. Note that non-oxide based semiconductors with a narrow optical band gap cannot be used as stable and optically transparent materials to protect Si-based cells. For this reason most low band gap semiconductor materials are generally unstable and absorb visible light, hence, cannot act as ideal optically transparent material.

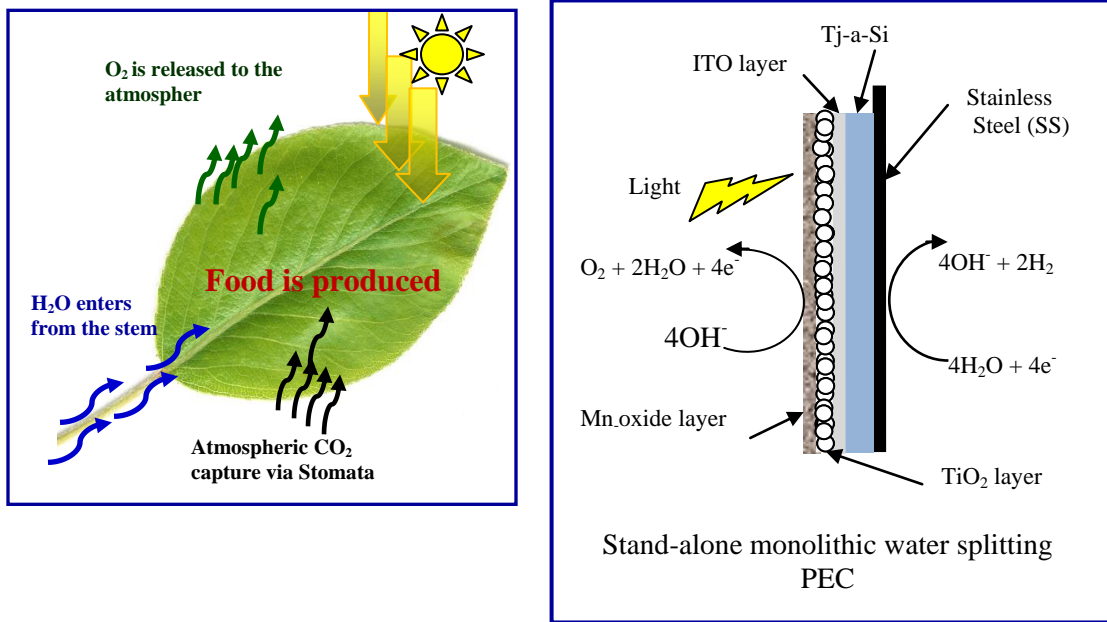


Figure 1.5 Monolithic water splitting electrochemical cell

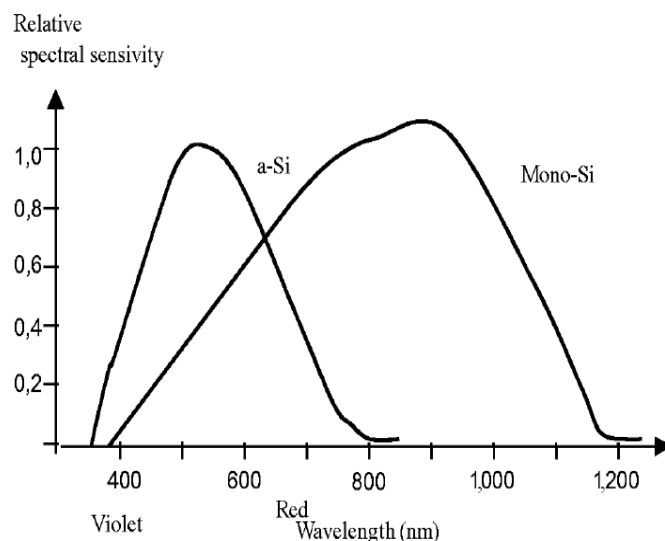


Figure 1.6 Spectral response for monocrystalline silicon (Mono-Si) and amorphous silicon (a-Si)⁵⁹

Due to the advantages of amorphous silicon (a-Si) mentioned above, Tj-a-Si could be used as a photoactive *n*-type anode for oxygen evolution. The counter reaction, HER, takes place at the back, dark side, of this leaf-like PEC (see Fig.1.5).

Past studies showed interests in the use of silicon based solar cells for direct water splitting under sunlight; however, they lacked stability in aqueous solutions. Hence, different materials and methods were employed for Si surface passivation in order to improve its stability during oxygen evolution or hydrogen evolution.^{61, 62, 63}

Transition metal oxides are cost effective thin films which can be used as TCCR protective layer on Tj-a-Si. Titanium oxide (TiO₂) is the most suitable among transition metal oxides because it absorbs only in the UV-region and exhibits high stability in alkaline mediums. Also, a thin coating of Mn₂O₃ was found to stabilize crystalline *n*-Si, and *n*-GaAs in earlier studies.^{62, 64} Low temperature processes at < 200 °C are essential to avoid thermal degradation of Tj-a-Si solar cells during deposition of these TCCR films

on its surface. Some important studies pioneered the utilization of solar cells such as single crystal Si (pin-pin),⁶¹ *p/n*-GaAs,⁶⁴ *p/n*-Si,²⁶ *n/p*-GaAs/*p*-GaInP₂,²⁷ *p/n*-Fe₂O₃,²² and triple junction amorphous silicon 65 for efficient self-driven photoelectrochemical splitting of water without the need an external power source.

1.3 Solar driven water electrolysis:

Electrolysis of water to generate hydrogen and oxygen is a well-known electrochemical process. It requires an external applied potential to overcome the thermodynamic, ohmic and kinetic barriers to drive the water-splitting reaction.^{66, 67} Compared to traditional processes that use fossil fuel to generate hydrogen, water electrolysis is a pollution free process and has the flexibility of choosing different external power sources such as electrical grid, solar cells or wind power. This makes water electrolysis the most desirable process.

Abundant and cost effective solar energy can be used to generate the external power required to drive the electrolysis reaction (Fig 1.7). However, low current efficiency of the present water electrolyzers has made the process less competitive compared to steam reforming of methanol or natural gas.^{68, 69} Past and current research efforts on water electrolysis have and are focused on the sluggish kinetics of oxygen evolution,^{70, 71} thereby, fundamental research to understand the mechanism of O₂ evolution on the catalyst surfaces are of great interest in the design of an efficient oxygen evolving electrocatalysts. Note that efficient oxygen evolving electrocatalysts are those with a minimum over potential and hence must operate at or near the Nernstian potential of the O₂/H₂O or the O₂/OH⁻ reaction in acidic or basic mediums, respectively and having

lower Tafel slope and high exchange current density (current density at zero overpotential).

Earlier work on the oxygen evolution reaction (OER) included noble metals and rare metal oxides such as RuO_2 and IrO_2 .^{72, 73, 74} However, the dependence on rare metals is not a popular approach because a massive worldwide manufacturing of noble/rare metal based electrolyzers would drive up the price further and the scarcity of such materials will limit large scale utilization. Perhaps the most suitable approach is to use earth abundant transition metals and their oxides or a combination of transition metals and their oxides in order to quell the over potential required for OER at the anode surface.

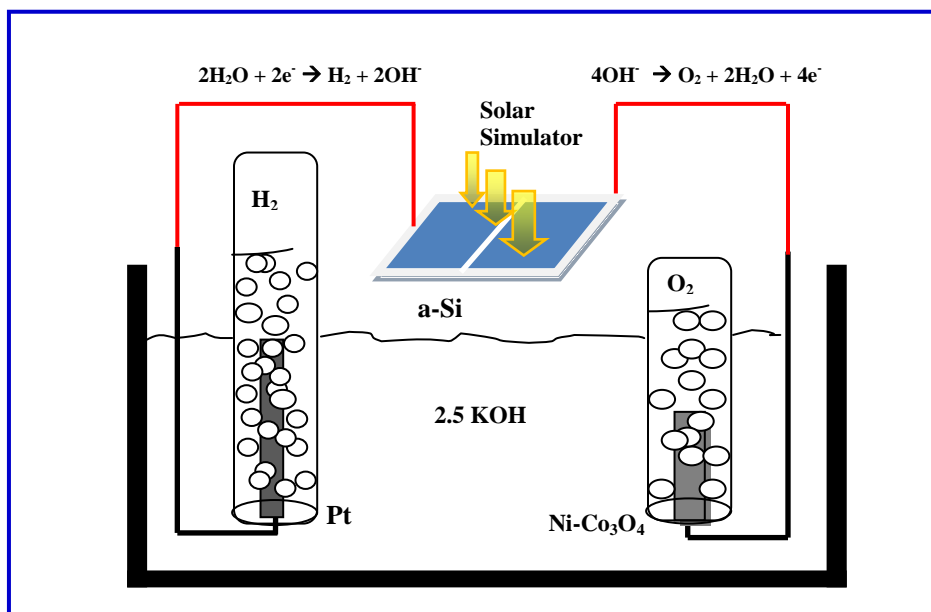


Figure 1.7 Solar driven water electrolysis.

The dilemma in the field of catalyst is the dearth of ample catalyst descriptors for oxygen evolution. Yet it is only by trial and error that catalysts such as RuO₂ and IrO₂ were discovered as state of the art catalysts for OER. Although there have been attempts to find some useful correlations between catalytic activity toward OER and the nature of the catalyst (e.g. metal oxidation state, surface morphology,...etc).^{71, 75, 76, 77} Up to now the most accepted descriptors or guidelines for efficient catalyst is the broadly known Volcano plots (figure 1.8)⁷⁵, where the catalysts activity of different metal oxides toward OER is plotted against the energy change involved during the transition from lower to higher valence state which results in a pyramid/volcano shape plot.

The transition metals, Ni and Co, and their oxides have been extensively studied individually and as alloys for their electrocatalytic activity toward the OER.^{78, 79, 80, 81, 82, 83, 84, 85, 86} Previous investigations on the transition metals single oxide electrodes (Ni-oxide and Co-oxide) were focused on enhancing the catalytic activity for OER by modifying the surface morphology. This work showed that the improvement of the catalytic activity of these earth abundant transition metal single oxides toward OER seemed to have reached a limit. Investigators in the field have already circumvented these limitations with the use of mixed transition metal oxides, where the synergistic effects on electrocatalytic activities toward OER as two or more oxides are mixed together were reported.^{73, 87} The electro-catalytic behavior of these mixed oxides toward OER was noted to be affected by the catalyst composition and synthesis techniques.⁸⁸

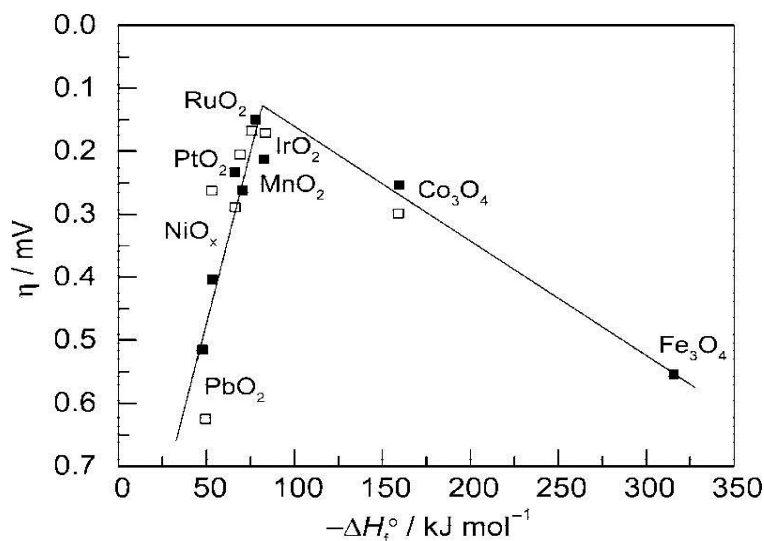


Figure 1.8 Volcano plot for oxygen evolution over metal oxide surfaces versus the enthalpy of the transition from lower oxide to higher oxide in acidic (filled squares) and basic mediums (unfilled squares).⁷⁵

1.4 Research Focus

In this dissertation we investigated three major routes for efficient photoelectrochemical water splitting. We reported first the photoelectrochemical splitting of water on the surface of photoactive semiconductor oxide. Titanium oxide and iron oxide were the photocatalysts of choice for this project. The photoactivity of the high band gap *n*-TiO₂ thin films was enhanced by the incorporation of hydrogen and carbon on its surface or lattice. Hydrogen modification of *n*-TiO₂ was achieved by cathodic reduction of a pristine *n*-TiO₂ in basic electrolyte. Carbon modification of *n*-TiO₂ was achieved by thermal flame oxidation of *n*-TiO₂. The successful use of carbon in *n*-TiO₂ modification was the drive in this project to dope Fe₂O₃ with carbon. In addition, the effect of the surface morphology on the electrochemical behavior of the modified or unmodified *n*-TiO₂ or Fe₂O₃ was investigated.

Inspired by the natural photosynthesis process, a leaf-like photoelectrochemical cell (PEC) was investigated for efficient and low cost water splitting. The new self-driven PEC consists of a-Si protected by a visible transparent thin film of TiO₂, which was further protected by a Mn-oxide thin film for long term use. In this “standalone” PEC the underlying a-Si provides the required photovoltage to drive the water splitting reaction and the top layer of TiO₂ insures the stability and tunes the unfavorable valence band of silicon.

In the third part of this project, Ni-Co-mixed oxides electrodes were synthesized from different volumetric ratios of Ni(NO₃)₂ and Co(NO₃)₂ aqueous solutions by spray pyrolysis. The spray was carried out on conducting fluorine doped tin oxide (FTO) coated glass substrate. The electrocatalytic activity of the Ni-Co mixed oxide electrodes toward oxygen evolution in basic medium was examined in terms of current density and was compared to Co-oxide electrodes which was recently introduced as the most efficient and low cost electrocatalyst for oxygen evolution.⁷⁹

Chapter 2

Experimental

2.1 Synthesis of hydrogen modified (HM-)n-TiO₂ thin films:

Ti metal sheets of 0.25 mm thick (Alfa Co.) were cut to an area of ~1.0 cm². Ti metal samples were cleaned in a sonicator for three 15 min intervals with: (i) acetone; (ii) acetone: double de-ionized water (1:1); (iii) double de-ionized water, then dried under dry Argon stream at room temperature. The dry Ti sheets were thermally oxidized to *n*-

TiO₂ in a tubular electric furnace with both ends opened to ambient atmosphere. The optimum conditions of oxidation temperature and time were investigated. The temperature in the tubular furnace was measured by a digital thermocouple (Omega Engineering). The *n*-TiO₂ thin films were then reduced by applying a negative voltage of -1.6 V vs SCE in a single compartment three electrodes electrochemical cell, where, *n*-TiO₂, Pt, and saturated calomel electrode (SCE) were the working, counter, and reference electrodes, respectively. The electrochemical reduction of *n*-TiO₂ was carried out in 2.5 M KOH under dark conditions for 6 minutes.

2.2 Synthesis of carbon modified (CM)*n*-TiO₂ thin films by thermal flame

oxidation:

Ti samples of ~1.0 cm² and 0.25 mm thickness (Alfa Co.) were cleaned as mentioned in section 2.1. CM-*n*-TiO₂ thin films were synthesized by flame oxidation of the cleaned Ti samples at different temperatures (700-850°C) and oxidation times, using a custom designed large area flame (Knight, model RN. 3.5 xawc) under controlled oxygen and natural gas flows. A digital thermocouple (Omega Engineering) was used to measure the flame's temperature, which was maintained constant by controlling the oxygen and natural gas flow rates using FL-1807 and FL-1806 flow meters (Omega Engineering), respectively. The optimum flow rate was found to be 2.23 L min⁻¹ for oxygen and 3.32 L min⁻¹ for natural gas. To insure a proper and uniform oxidation the flame was kept downward facing the Ti sample (Fig. 2.1). The front side of the CM-*n*-TiO₂ electrode is the area facing the flame. The apparatus was kept in a closed system to avoid the effects of the natural air flow from the surrounding environment on the flame. The combustion

products were naturally vented from this system. For comparison a reference sample of undoped n -TiO₂ was synthesized as mentioned in section 2.1.

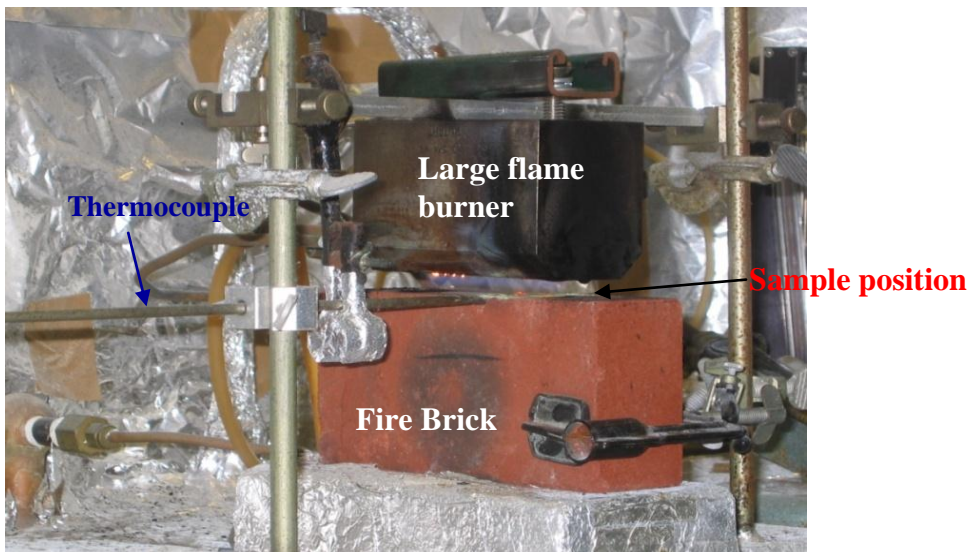


Figure 2.1 Thermal flame oxidation of Ti metal sample for the synthesis of CM- n -TiO₂

2.3 Synthesis of nanostructured n -TiO₂ thin films:

Ti metal samples of $\sim 1.0 \text{ cm}^2$ and 0.25 mm thickness (Alfa Co.) were cleaned as reported in section 2.1. The clean and dried Ti metal samples were initially etched in concentrated HCl at 80°C for 10 min to remove any remaining oxides on the surface of the Ti metal samples. After washing with sufficient DI water the etched sample were hydrothermally treated in about 5% HCl at 200°C in an autoclave or acid digesting vessel (model: parr 4746-4747 High Pressure, 23 mL) for 5-10 hours (Fig. 2.2). After cooling, the Ti samples were cleaned with enough DI water then dried under a dry argon stream at room temperature. The surface morphology of the resulting Ti samples was examined using a Hitachi S3400 scanning electron microscope. The nanostructured Ti samples

were oxidized according to sections 2.1 and 2.2 to yield $n\text{-TiO}_2$ and CM- $n\text{-TiO}_2$ thin films respectively.

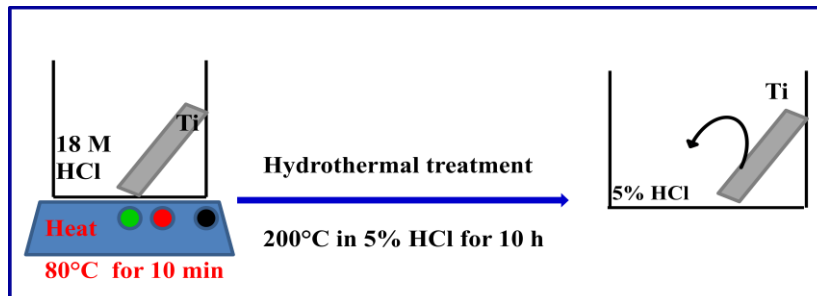


Figure 2.2 Hydrothermal treatments of Ti metal samples.

2.4 Surface modification of $n\text{-TiO}_2$ and CM- $n\text{-TiO}_2$ thin films by metal islets:

Details regarding the synthesise of CM- $n\text{-TiO}_2$ and $n\text{-TiO}_2$ can be found in our earlier sections. Electrodeposition of different metal islets were performed in a three electrodes single-compartment electrochemical cell with $n\text{-TiO}_2$ or CM- $n\text{-TiO}_2$ as a working electrode, platinum wire as the counter electrode and a saturated calomel electrode (SCE) as the reference. The galvanostatic electrodeposition of different metal islets on the surface of $n\text{-TiO}_2$ and CM- $n\text{-TiO}_2$ electrodes surfaces was carried out at a current density of $-250 \mu\text{A cm}^{-2}$ ⁸⁹ for different times (seconds) using scanning potentiostat (VersaSTAT 3 running VersaStudio software, Princeton Applied Research). All electrodeposition experiments were performed at room temperature accept for nickel (Ni), where the temperature of nickel electrodeposition bath was kept at 50°C.⁹⁰ The undoped $n\text{-TiO}_2$ samples were reduced/hydrogenated to HM- $n\text{-TiO}_2$ in a basic electrolyte (2.5 M KOH) prior to metal electrodeposition. The procedure was carried out in the same

electrochemical cell, as mentioned above, by applying a negative polarization potential (-1.6 V/SCE for 6 minute) to the working electrode.

2.5 Synthesis of iron oxide ($n\text{-Fe}_2\text{O}_3$) nanowires and carbon modified (CM-) $n\text{-Fe}_2\text{O}_3$ thin films:

Iron metal sheets of $\sim 1\text{cm}^2$ and 0.25mm thickness (Alfa Co.) were cleaned and dried according to the procedure used to clean Ti metal samples. The cleaned and dried Fe metal samples were thermally oxidized at different temperatures in a tubular electric furnace with both ends opened to ambient atmosphere (Multiple Unit, Series C4497 WEO). Iron (III) oxide nanowire thin films were prepared by the oxidation of Fe samples at different temperatures (550 – 900°C) for different periods of times. The synthesis of CM- $n\text{-Fe}_2\text{O}_3$ thin films was carried out by flame oxidation of Fe metal sheet at different temperatures (700–900°C) and time. The same method and apparatus used to carry out the flame oxidation of Ti metal sheet was used in making CM- $n\text{-Fe}_2\text{O}_3$.

2.6 Measurements of photocurrent density:

The photoresponse of the photoanodes, HM- $n\text{-TiO}_2$, CM- $n\text{-TiO}_2$, $n\text{-Fe}_2\text{O}_3$ nanowires and CM- $n\text{-Fe}_2\text{O}_3$ was evaluated by measuring the rate of oxygen evolution, which is proportional to the anodic photocurrent density, J_p (mA cm^{-2}). The working electrodes were placed at a distance of 8 inches from the light source and illuminated by a full spectrum of solar simulated light with an intensity of 0.1W.cm^{-2} (1 sun) from a solar simulator with a global AM 1.5 filter (Thermo Oriel model 81192). The intensity of the solar simulated light and the spectral radiation of the solar simulator were measured with

a Silicon detector (UDT Sensors Inc., Model 10DP/SB) having a spectral response as shown in Fig. 2.3.⁹¹

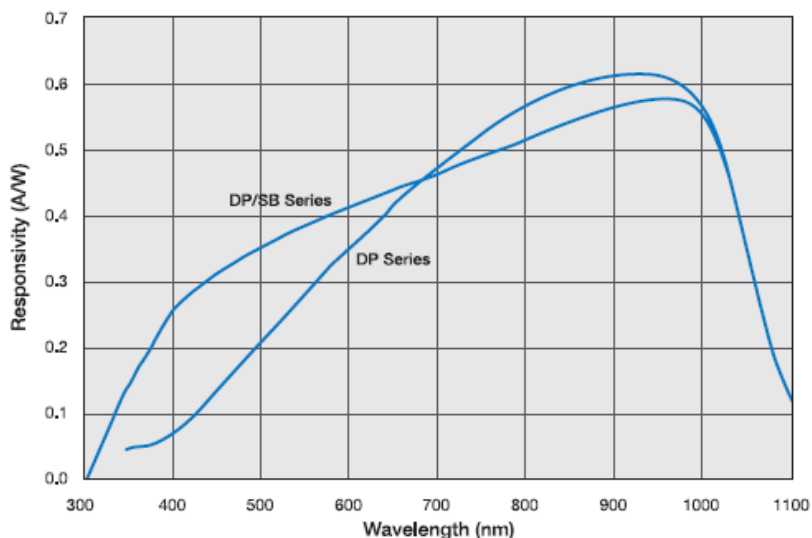


Figure 2.3 Spectral response of the silicon detector: model 10DP/SB.⁹¹

Linear sweep voltammetry (LSV) curves of the photoelectrodes were obtained using a scanning potentiostat (VersaSTAT 3 running VersaStudio software, Princeton Applied Research) at a scan rate of 50 mV.s^{-1} . This experiment was performed in a custom made three-electrode single-compartment electrochemical cell, with the semiconductor as working electrode, platinum wire as a counter electrode, and the saturated calomel electrode (SCE) as a reference. A solution of 2.5 M KOH was used as the electrolyte. The electrochemical behavior of the photocatalysts was studied by LSV in the dark and under solar simulated light illumination. The photocurrent density (J_{photo}) was obtained by subtracting the dark current density (J_{dark}) from the total current density under illumination, J_{total} (Fig. 2.4). The electrochemical cell compartment was made of quartz to minimize its interaction with the incident light. A spectra-physics

monochromator, model 7725, was used to generate monochromatic light in order to measure the monochromatic photocurrent density, $J_p(\lambda)$, of the photoelectrodes.

$$J_{photo} = J_{total} - J_{dark} \quad (11)$$

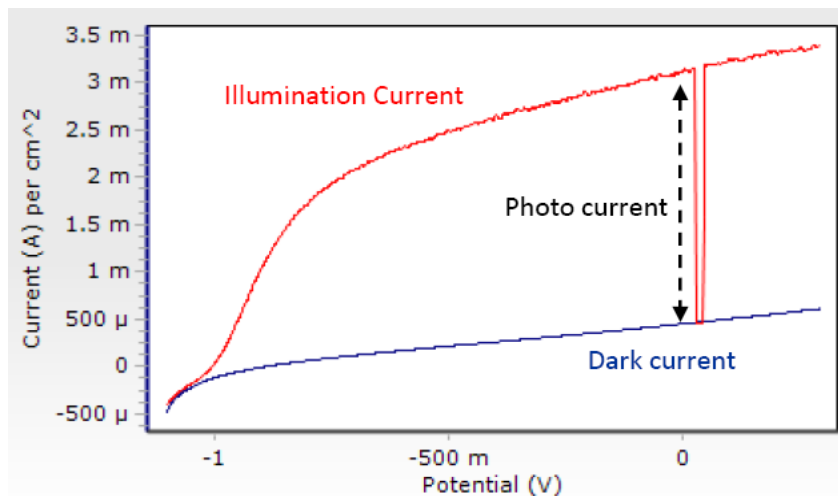


Figure 2.4 Photocurrent density measurements by subtracting the dark current density from the illumination current density.

2.7 Solar simulated light source:

To test the photocatalyst electrodes for water splitting, it is convenient to have a source of light as part of the research laboratory set up. Photoelectrochemical water splitting reactions have been carried out under different sources of light such as xenon lamps and solar simulators. These light sources operate at different electrical power inputs and consequently lead to different incident light intensities and spectral distributions compared to sunlight. Over the past years xenon lamps have received a lot of criticism as a non reliable light source. Xenon lamps contain more UV light with

respect to the solar spectrum, and the amount of UV light increases as the lamp gets older. In addition, the light intensity from xenon lamps is not uniform and is dependent upon the distance from the light source. Lately most research laboratories in this field are equipped with solar simulators as a reliable light source. Solar simulators not only produce an incident light with intensity close to that of natural sunlight (1sun or 0.1 W cm^{-2}), but also simulate the spectral distribution of the incident light to be consistent with the full spectrum of sunlight. Light generated by a solar simulator contains the same amount of UV and visible light with respect to natural light. One of the serious issues in this field is the absence of a standardized procedure or technique to measure and quantify the solar simulated light in research laboratories.

A solar simulator (Thermo Oriel model 81192) equipped with 1000 W Xenon lamp and a global AM 1.5 filter was used as a light source throughout this investigation. The light intensity was measured using Si detector (Model 10DP/SB) as mentioned in the previous section. Note that Si detectors with different spectral sensitivities may lead to different light intensities as well as to a different spectral distribution of the incident light. Hence, it is not possible to fully compare the spectrum obtained in different laboratories using different detectors. Figure 2.5 shows a comparison between the full spectrum of the solar simulator used in this investigation and the full spectrum of the solar light obtained from NREL.⁹² The term full spectrum used here is limited to the UV and visible regions as these are the only radiations that drive the electronic transitions within titanium oxide and iron oxide semiconductors.

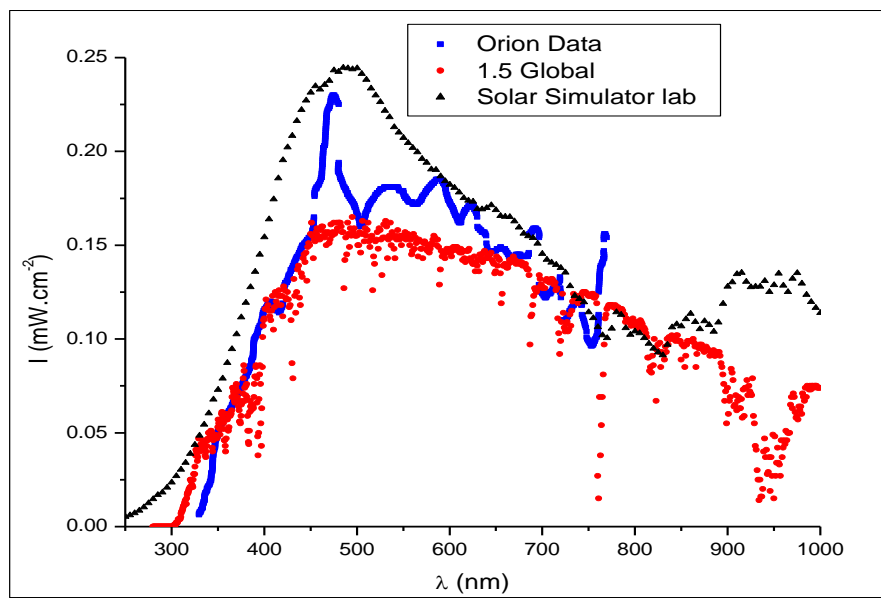


Figure 2.5 Solar simulator spectrum compared to spectral irradiance air mass 1.5, Orion Data: the spectral data obtained from the manufacturer, Solar Simulator lab: spectral data measured in the lab using Si detector (model-DP/SB), 1.5 Global: full spectrum of the solar light obtained from NREL.

2.8 Fabrication of a self-driven a-Si based photoelectrochemical cell (PEC):

2.8.1 Deposition of visible light transparent TiO₂ on Tj-a-Si:

An advanced method was used to deposit a homogenous and durable thin film of TiO₂ on a Tj-a-Si surface. In this method an ultrafine colloidal solution of TiO₂ (Degussa p 25) was utilized instead of a suspension of TiO₂ particles. The colloidal solution consisted of 80 mg of TiO₂ powder in 10 mL of ethanol, in presence of 10 μ L of acetylacetone as a structure directing agent.⁹³ A binder Triton X100 (5 micro liters in 10 mL of ethanol) was added to the suspension to obtain homogeneous films. Also, the binder helped to minimize the cracking in the film during drying. The mixture was first homogenized in a high-speed centrifuge (Avanti J-20XP) at 3,000 rpm for 15 min in order to obtain a clear colloidal solution at the top and a thick white precipitate at the

bottom. A single drop from the top of the ultrafine colloidal solution of TiO_2 was spread on the surface of the Tj-a-Si with an area of 0.69 cm^2 then spin coated for one min. This process was repeated for several times and then dried at room temperature. The resulting films of TiO_2 were sintered at 200°C for 1 hour to obtain a uniform solvent free TiO_2 thin film on the Tj-a-Si surface. The optimum number of drops was limited to 10, to allow enough light to reach the underlying Tj-a-Si (Fig. 2.6).

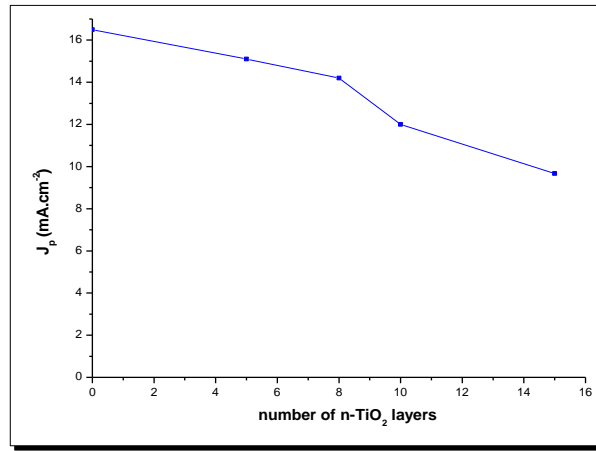


Figure 2.6 Photocurrent density of TiO_2 covered Tj-a-Si versus the number of drops of TiO_2 .

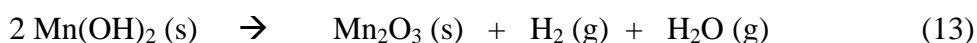
2.8.2 Deposition of manganese oxide layer on TiO_2 covered Tj-a-Si solar cell:

The bath for the deposition of manganese oxide thin layer consisted of aqueous solutions of 0.03 M MnCl_2 , 1.4 M NH_4OH having a total volume of 50 mL. 0.25M of NH_4Cl was added to the mixture to slightly lower the pH of the solution. The solution was stirred continuously at room temperature. The TiO_2 thin film covered Tj-a-Si solar cell sample was then immersed in the deposition bath for 15 minutes to allow deposition of $\text{Mn}(\text{OH})_2$ on its surface. After taking it out of the deposition bath the sample was rinsed with double deionized water and dried at room temperature. It was then

transferred to a glass funnel that was evacuated to 2×10^{-5} torr. The sample in the evacuated glass funnel was heated at 220°C for 15 min (Fig. 2.7). Heating in the vacuum resulted in the loss of water and hydrogen, thereby leaving a thin film of Mn_2O_3 . The deposition process of Mn_2O_3 is described by chemical reactions (12) and (13):⁶²



During heating at 220°C under vacuum of 2×10^{-5} torr:



Formation of Mn_2O_3 was confirmed earlier by X-ray photoelectron spectroscopy analysis (XPS).⁶² Note that the unstable MnO_2 would be formed when $\text{Mn}(\text{OH})_2$ is heated under ambient conditions according to the reaction:

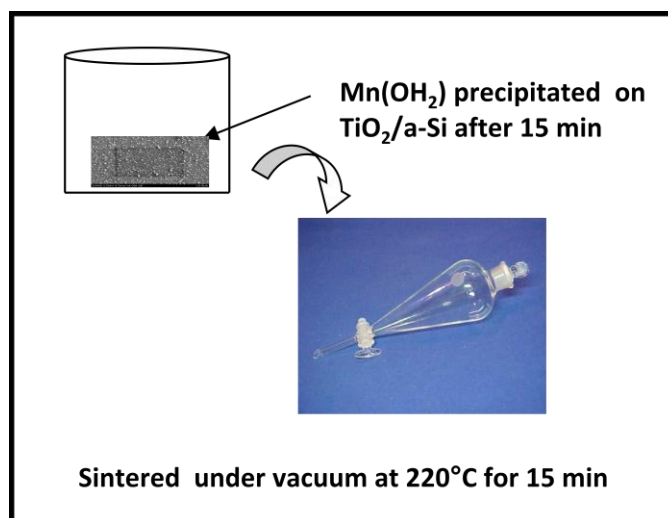
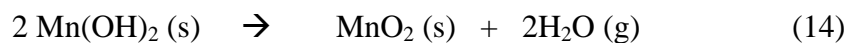


Figure 2.7 Curing $\text{Mn}(\text{OH})_2$ deposited on TiO_2 covered Tj-a-Si in vacuum.

2.8.3 Hydrogen gas collection at Pt cathode in Mn-oxide-TiO₂ coated

Tj-a-Si /Pt PEC:

Schematic diagram of a monolithic self-driven Mn-oxide-TiO₂ coated Tj-a-Si/SS PEC as shown in Figure 1.5 was modified to Mn-oxide-TiO₂ coated Tj-a-Si/Pt PEC Figure 2.8 by connecting a platinum wire with the back stainless steel (SS) surface to facilitate H₂ gas collection. The self-driven monolithic water splitting PEC under solar simulated light illumination in which O₂ evolves on the front Mn-oxide-TiO₂ coated Tj-a-Si surface (photoanode) and H₂ evolves on Pt (cathode). Hydrogen gas was collected by displacing the electrolyte solution inside a graduated test tube inverted over the Pt wire.

The Mn-oxide-TiO₂ coated Tj-a-Si- solar cell was placed at a distance of 8 inches from the solar simulator with global AM 1.5 filters having light intensity of 0.1W cm⁻² (1 sun). The bias needed for water splitting reaction was provided by the underlying Tj-a-Si solar cell under the same illumination conditions.

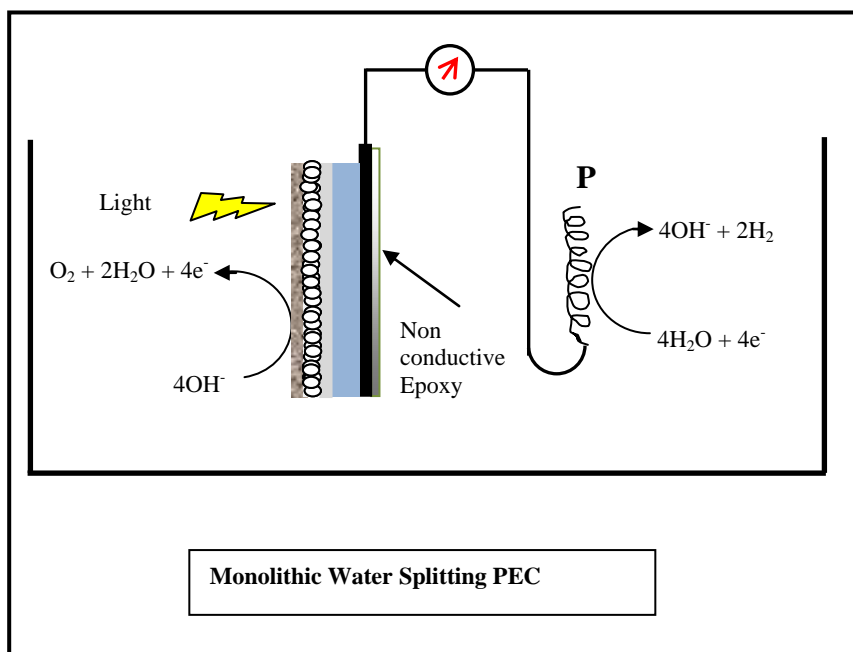
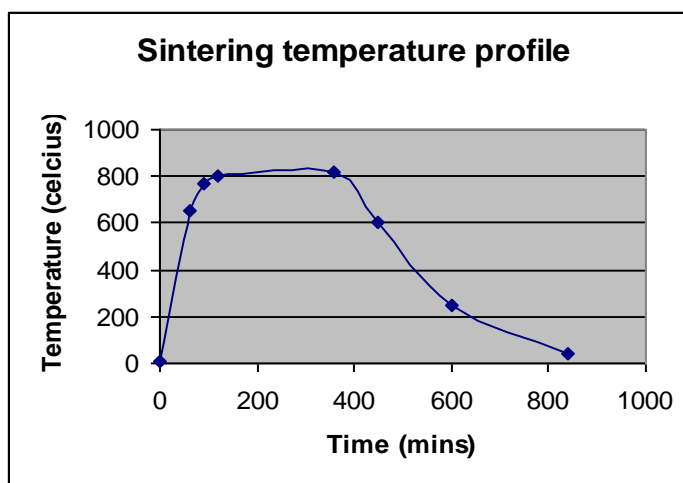


Figure 2.8 Water splitting using a self driven monolithic a-Si based PEC.

2.9 Synthesis of Ni-Co₃O₄ porous electrode:

Suitable amounts of Ni metal powder (150 micron, 99.99%, Sigma-Aldrich), Co₃O₄ powder (10 micron, Sigma-Aldrich) and small amounts (0.1 molar ratio) Al powder (20 micron, 99 %, Sigma-Aldrich) were thoroughly mixed. The mixture was pressed under a pressure of 20 torr. The resulting pallet was sintered at 800 °C for 4 hours in an electric furnace with controlled heating and cooling cycles under argon atmosphere. The temperature profile of the sintering is shown in Figure 2.9.



draining out. This was continued until the sample got completely saturated with water. The amount of water needed to saturate the sample gave us the void volume, i.e. empty volume created by leaching out of aluminum powder. For calculating the bulk volume, a graduated cylinder of 10 mL was taken. The bulk volume was calculated by displacement of water by completely water saturated electrode in a graduated cylinder filled with water. The change in the level indicated the total bulk volume of the electrode filled with water. From these values of void volume and the bulk volume, the void ratio of Ni-Co₃O₄ was calculated from the following formula:

$$\text{Void Ratio} = \frac{\text{Void Volume}}{\text{Bulk Volume}} \quad (15)$$

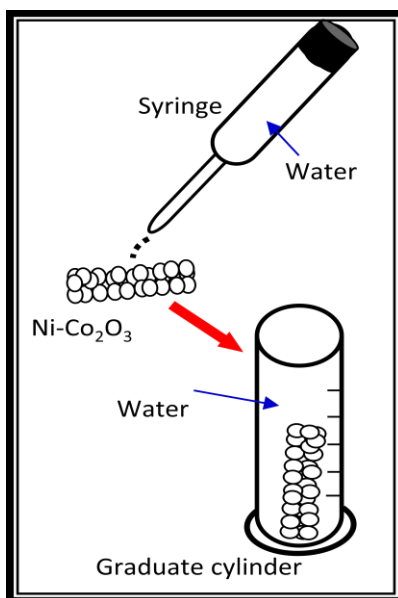


Figure 2.10 fluid pore filling porosity measurements for Ni-Co₃O₄ electrode

For comparison RuO₂ thin films were deposited on the surface of Ti metal sheet (Ti metal sample were cleaned as reported in section 2.1). Ruthenium chloride paste was

painted on the surface of the cleaned Ti substrate and dried first at 60 °C for 20 min under air ambient, then heated in air for 20 min at 250–275 °C. The procedure was repeated 2 to 3 times to increase the RuO₂ thin film thickness then finally annealed under air ambient for 4 h at 250 –275 °C.⁶¹

The catalytic activity of Ni-Co₃O₄ toward OER, in terms of H₂ collected over the cathode, was compared to the state of the art Ti-RuO₂ in a solar driven water electrolysis in 2.5 M KOH, with Pt as a cathode. The external bias was provided to the electrochemical cell via a silicon based solar cell under solar simulated light. Hydrogen gas was collected by displacing the electrolyte solution inside a graduated test tube inverted over the Pt cathode.

2.10 Synthesis of Co-oxide and Ni-Co-mixed oxide thin film electrodes:

Commercially available fluorine doped tin oxide (FTO) coated conducting glass substrates were cleaned in a sonicator using acetone, Acetone: Di-water (50:50) and Di-water respectively. Each step lasted 30 min. The cleaned FTO glass substrates were then dried under dry argon stream. The resistivity of the resulting ITOs was found to be within 14-20 ohm cm at room temperature. Aqueous solutions of 0.05 M Ni(NO₃)₂, 0.05 M Co(NO₃)₂ and different volume ratios of these aqueous solutions were used as spray solutions to synthesize Co-oxide and Ni-Co mixed oxides. The spray operation was carried out for a total of 30 sec having three 10 sec spray periods on an FTO conducting glass substrate at a temperature of 180°C using a pneumatic nozzle and oxygen as the carrier gas figure 2.11. In between each spray period there were intervals of ~ 10 min for the substrate temperature to be raised to 180°C on a hot plate. It is important to mention

here that the total spray time depends solely on the nozzle's orifice and the pressure of O₂ carrier gas. A conducting silver epoxy was applied to the four edges of the FTO glass to ensure a uniform electrical conductivity across the electrode surface during water electrolysis. After the spray the silver epoxy at the edges of the electrodes was covered with a non-conductive resin based epoxy. Cyclic Voltammetry (CV) was used as the main tool to examine the electrocatalytic performance of these electrodes toward OER. A three electrodes configuration in a single-compartment cell was used, with Ni-Co mixed oxides or Co-oxide as a working electrode, platinum wire as a counter electrode, and SCE as a reference electrode. The single compartment cell was filled with 2.5 M KOH as an electrolyte solution.

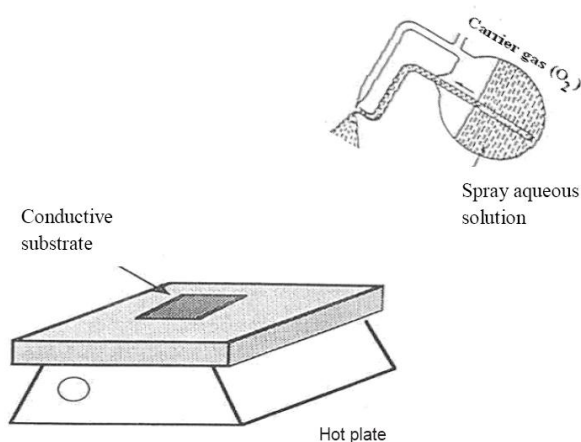


Figure 2.11 Spray pyrolysis apparatus used to synthesis Ni-Co-mixed oxides and Co-monoxides catalysts.

2.11 Scanning electron microscopic (SEM) and energy dispersive spectroscopic (EDS) measurements:

The surface morphology of the synthesized thin film oxides was characterized using Scanning Electron Microscopy (SEM), and was performed on a high-resolution

Hitachi S-3400 SEM. The Hitachi S-3400 SEM equipped with a Bruker Quantax energy dispersive spectrometer was also used for energy dispersive spectroscopic (EDS) analysis. Samples were mounted on a double sided carbon tape affixed to an aluminum sample holder. EDS spectra and mapping were collected at accelerating voltage of 15 kV and a working distance of 10 mm. A high field emission ZEISS EVO SEM was also used to characterize the surface morphology of CM-*n*-TiO₂, *n*-Fe₂O₃ nanowires and CM-*n*-Fe₂O₃ thin films.

2.12 UV-Vis Spectroscopic Measurements:

UV-Vis absorption spectra of CM-*n*-TiO₂, and CM-*n*-Fe₂O₃ thin films were recorded using a Varian Cary 1E UV-Visible Spectrophotometer. Labsphere (Model DRA-Ca-30I) with a reflectance Teflon standard (I.D.USRS-99-010) was used.

2.13 X-ray and XPS characterization of oxide thin films:

Crystallographic information were collected from X-ray diffraction (XRD) using PANalytical X'Pert-Pro MPD with 45 kV Cu K α radiation source ($\lambda = 1.541 \text{ \AA}$). Scans were collected from 20 to 70 degrees 2θ at a continuous scan rate. The change in the valence band induced by the hydrogenation of *n*-TiO₂ was examined by XPS measurements. The measurement was carried out using a leybold LHS-10 spectrometer with MgK α (1253.6 eV) X-ray source at a pass energy of 100 eV. The pressure in the analysis chamber was typically 2×10^{-8} Torr.

Chapter 3

Results and Discussion

3.1 Hydrogen modified (HM)*n*-TiO₂ thin film electrodes

3.1.1 Photoresponse of HM-*n*-TiO₂ thin film electrodes:

Under light illumination with energy larger than the band gap energy, electrons and holes are generated within the photocatalyst (*n*-TiO₂). Applying an external positive bias above the flat band potential of the semiconductor leads to the bending of the valence and conduction bands. Electrons are transferred from the anode (under positive polarization) to the counter electrode via an external circuit in the electrochemical cell while the holes are diffused to the surface of the *n*-TiO₂ to react with oxidizable species at the electrode –electrolyte interface (Fig. 3.1).

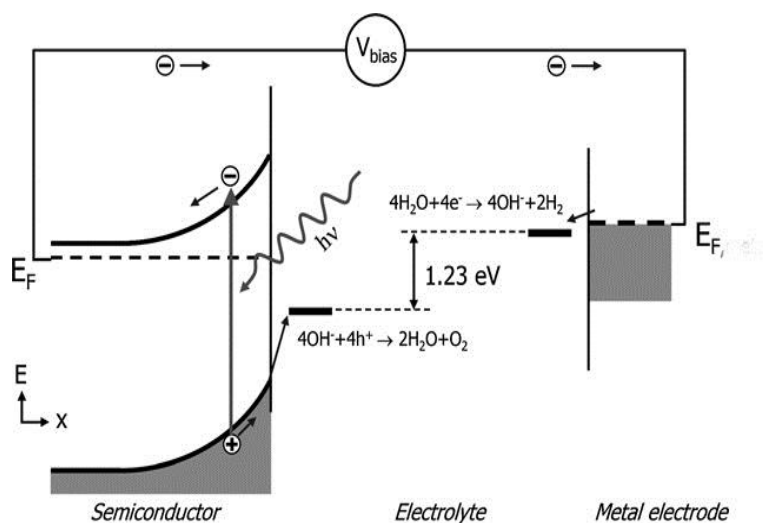


Figure 3.1 Photoelectrochemical cell under light and an external bias for water splitting.⁹⁴

Figure 3.2 shows the dependence of photocurrent density (J_p , mA cm^{-2}) as a function of measured potential (E_{meas} vs SCE) for undoped $n\text{-TiO}_2$ and hydrogen modified HM- $n\text{-TiO}_2$ synthesized as reported in the experimental section 2.1. It is observed in Figure 3.2, for example, at -0.4 V/SCE that the photocurrent density enhanced to 1.97 mA cm^{-2} for HM- $n\text{-TiO}_2$ compared to 0.5 mA cm^{-2} for undoped $n\text{-TiO}_2$. This fourfold enhancement of the photoactivity of HM- $n\text{-TiO}_2$ in terms of photocurrent density could be attributed to the reduction of $n\text{-TiO}_2$ by gain of hydrogen during the cathodic polarization of $n\text{-TiO}_2$ in 2.5 M KOH electrolyte.

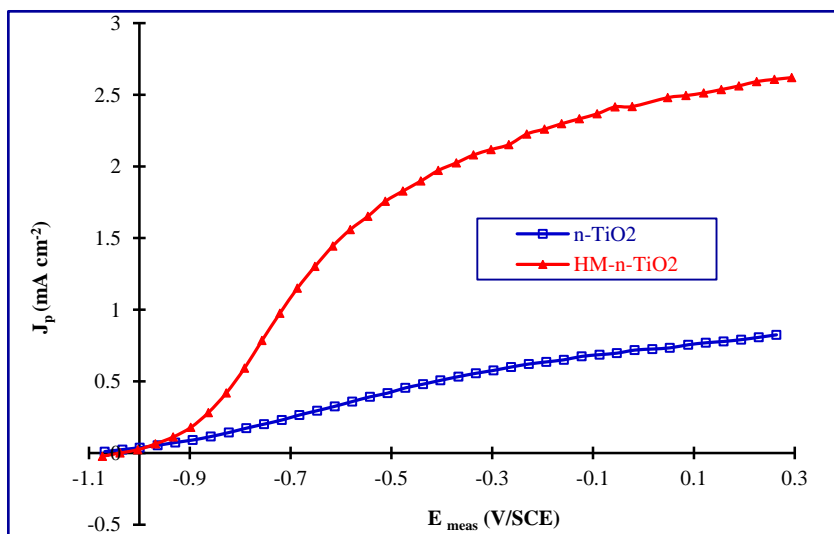


Figure 3.2 Photocurrent density of undoped $n\text{-TiO}_2$ and HM- $n\text{-TiO}_2$ thin film electrodes as a function of measured potential in 2.5 M KOH electrolyte and under 0.1 W cm^{-2} solar simulated light.

As indicated in the experimental section the hydrogenation of $n\text{-TiO}_2$ was carried out by cathodic reduction of the electrode at -1.6 V/SCE in a 2.5 M KOH solution. Taking into account the nature of chemical species in the electrolyte at this negative potential, the only reaction expected at the electrode surface is hydrogen evolution. And

according to Lemon et. al.⁹⁵ besides molecular hydrogen formation during the reduction some of the protons are inserted within the structure of n -TiO₂ to compensate for the negative charge. Ultimately proton insertion increases the nonstoichiometry/defect in n -TiO₂ structure which may lead to the formation of mid-gap states¹⁵ where electrons could be excited from either the valence band or the newly created states to the conduction band.

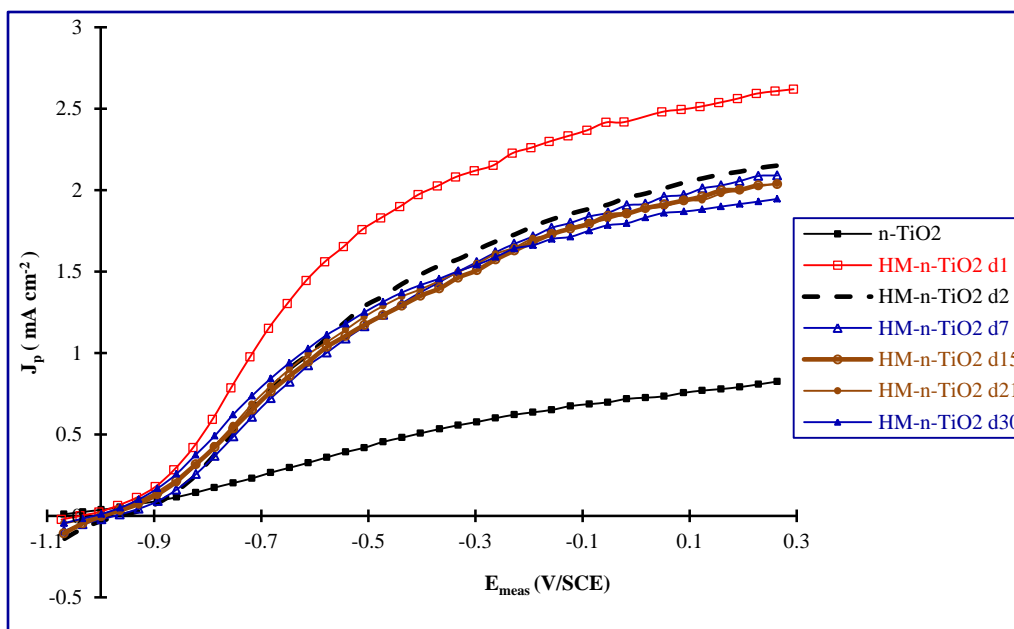


Figure 3.3. Cycling tests for HM- n -TiO₂ in terms of photocurrent density, J_p (mA cm⁻²) under the same experimental conditions as was specified earlier in the experimental sections. Each curve is defined in the plot's legend from d1 (day 1) to d30 (day 30).

Cycling of HM- n -TiO₂ photocatalyst as a function of time was carried out for 30 days testing period. The test consists of measuring the photocurrent density generated during water splitting under solar simulated light. Initially, the photoactivity of HM- n -TiO₂ decreased after the first day then exhibited a substantial stability for the following 29 days as shown in Figure 3.3. During the cycling period, HM- n -TiO₂ was rinsed with DI-water after each measurement and then dried at room temperature. Because hydrogen

tends to be attracted to dangling bonds³⁷, the initial drop of the modified n -TiO₂ photoactivity could be due to the loss of all or part of the hydrogen attached to dangling bonds at the surface of the semiconductor.

These results led to investigate of the photoactivity of HM- n -TiO₂ after drying it at a higher temperature. Figure 3.4 shows that after drying at 200°C the photocurrent density of HM- n -TiO₂ decreased significantly. More interestingly, the photoactivity of the dried electrode was restored after reducing it under the same experimental conditions as shown in Figure 3.5.

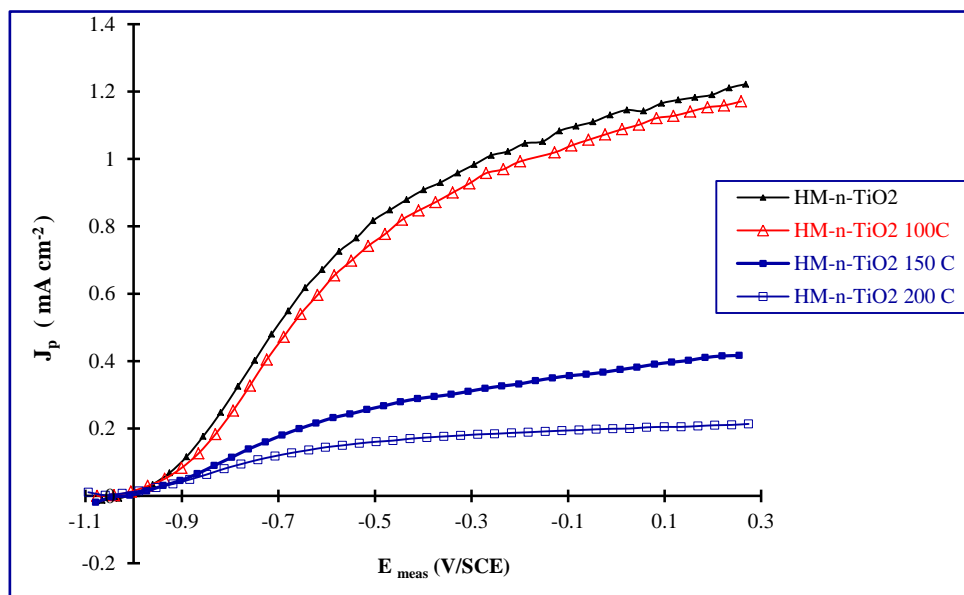


Figure 3.4. Cycling tests for HM- n -TiO₂ in terms of photocurrent density, J_p (mA cm⁻²) after drying the electrode at 100°C, 150°C and 200°C, respectively.

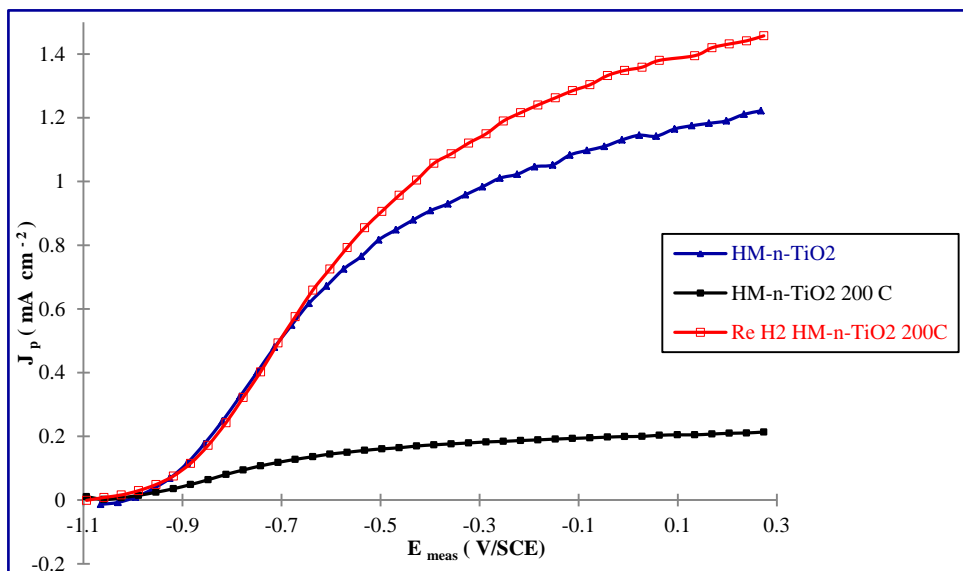


Figure 3.5. Photocurrent density of HM-*n*-TiO₂, the dried HM-*n*-TiO₂ at 200°C (HM-*n*-TiO₂ 200°C) and the rehydrogenated HM-*n*-TiO₂ (Re H₂ HM-*n*-TiO₂ 200°C) thin film electrodes as a function of applied potential.

3.1.2 Characterization of HM-*n*-TiO₂ thin films using spectroscopic methods:

Surface morphology of *n*-TiO₂ thin films was investigated using scanning electron microscopy (SEM) before and after hydrogenation and no sign of difference was observed as shown in figure 3.6.

X-ray diffraction spectroscopy (XRD) was used to investigate the structure of *n*-TiO₂ thin films before and after hydrogenation. Figure 3.7 shows strong XRD diffraction peaks which signify that the thin film of *n*-TiO₂ is highly crystalline and consists mainly on rutile phase with some peaks belonging to the anatase phase. The peak at 53° 2θ may belong to Ti metal or to the non stoichiometric titanium oxide^{96, 97} such as Ti₃O (jcpds: 01-073-1583) and Ti₆O (jcpds: 01-072-1471). After hydrogenation, the new HM-*n*-TiO₂ thin film XRD pattern (Fig. 3.7) exhibits the same crystalline phase. From XRD patterns of *n*-TiO₂ and HM-*n*-TiO₂ it can be concluded that reduction/

hydrogenation of $n\text{-TiO}_2$ does not result in a systematic change in its crystalline phase.³⁷ Therefore the incorporation of hydrogen could be either limited to the surface of the electrode or a possible charge compensating cations intercalation into the lattice of $n\text{-TiO}_2$ during the reduction process. The intercalation of hydrogen into the lattice of $n\text{-TiO}_2$ was suggested by Lemon et al.⁹⁵ who confirmed proton insertion with the use of Quartz Crystal Microbalance analysis.

The density of states (DOS) of the valence band of $n\text{-TiO}_2$ and HM- $n\text{-TiO}_2$ was measured with valence band X-ray photoelectron spectroscopy (XPS). Figures 3.8 show that the hydrogenated $n\text{-TiO}_2$ thin film exhibits an identical valence band similar to that of $n\text{-TiO}_2$ prior to hydrogenation and no additional electronic states were observed above the valence band in contrast to what was reported by Chen et al.^{37, 38} It was noted that in their case hydrogenation of $n\text{-TiO}_2$ nanoparticles was carried out at a high temperature.

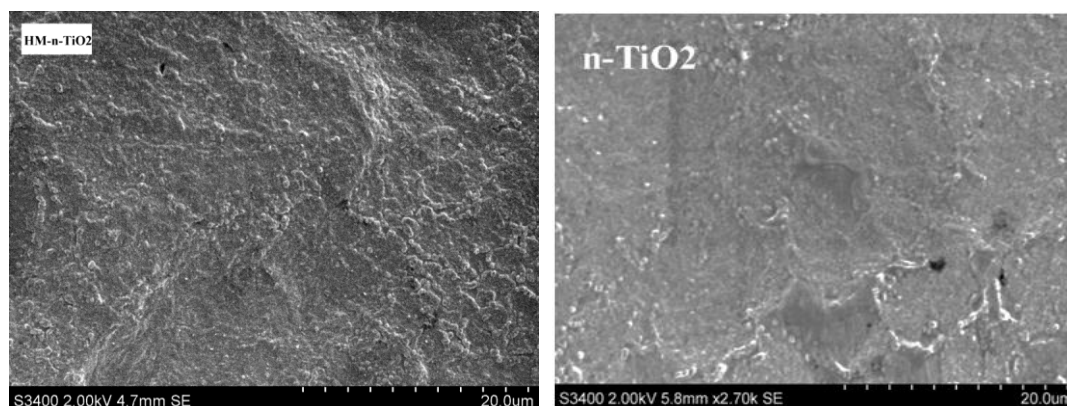


Figure. 3.6 Top view SEM images for HM- $n\text{-TiO}_2$ thin films and regular $n\text{-TiO}_2$ thin films before reduction

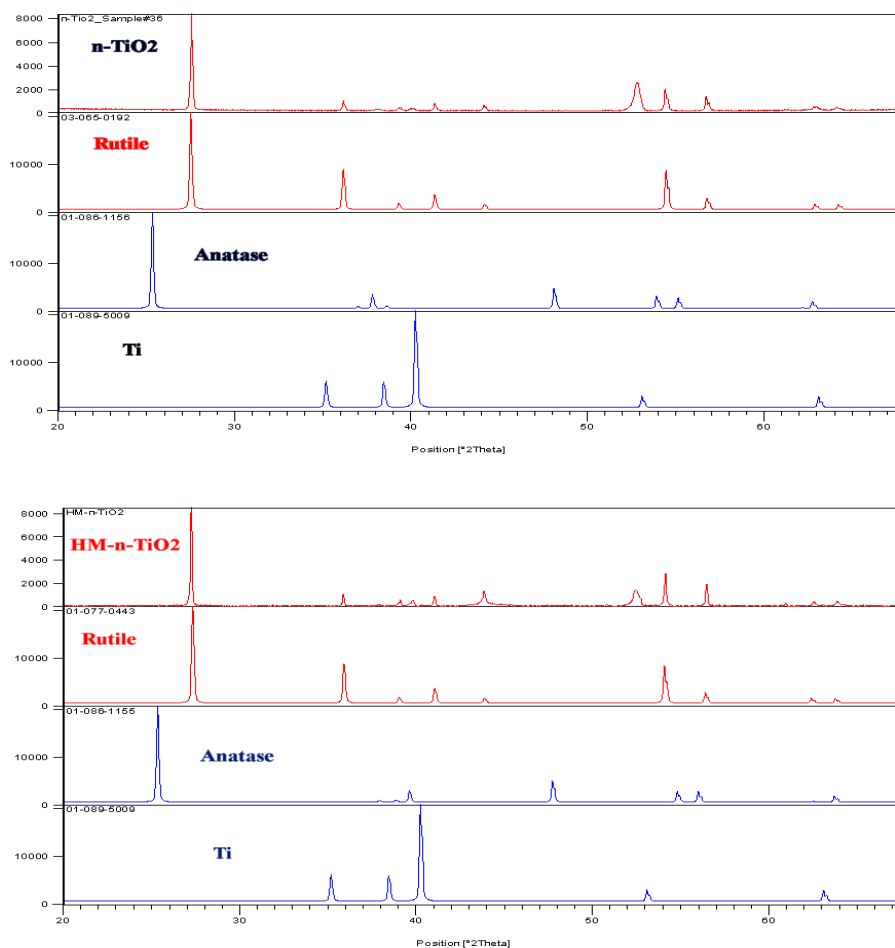


Figure 3.7 X-ray diffraction (XRD) patterns for *n*-TiO₂ and HM-*n*-TiO₂ thin films compared to reference patterns (jcpds cards) of Rutile (03-065-0192, 01-077-0443); Anatase (01-086-1156, 01-086-1155); and Ti (01-089-5009)

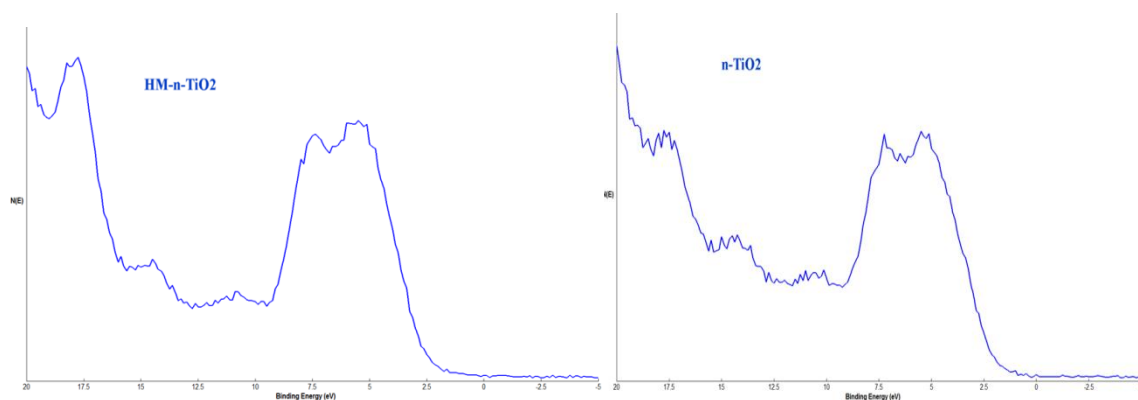


Figure 3.8 valence band X-ray photoelectron spectroscopy (XPS) spectra for regular HM-*n*-TiO₂ and *n*-TiO₂.

3.1.3 Monochromatic photocurrent of HM-*n*-TiO₂ thin film electrodes:

The photoresponse of an electrode under monochromatic light (UV, visible and IR regions) is of great importance for its applications. The monochromatic photocurrent plot has a significant advantage over the UV-Vis absorbance spectra due to electronic transitions not related to the band gap, such as d-d transitions⁹⁸ which are the result of photon absorption with no photocurrent generation.

To investigate the photoresponse of HM-*n*-TiO₂ under various single wave lengths of the incident solar simulated light, a monochromatic photocurrent density, $j_p(\lambda)$, measured at an applied potential of 0.2 V/SCE versus wavelength λ (nm), was collected and plotted. Because photocurrent density depends on the applied potential (Fig. 3.2), the later was chosen to be within the photocurrent saturation region. Figure 3.9 shows that the photosensitivity of HM-*n*-TiO₂ increased in the UV region compared to undoped *n*-TiO₂. However, the photocurrent decreases significantly under shorter wave lengths in the UV region ($\leq 350\text{nm}$) for both electrodes. The low photocurrent generated in this region is due to the low efficiency of charge carrier collection⁹⁹. This phenomenon can be explained by the fact that under highly energetic wave lengths (within the UV region), the conduction band of the semiconductor becomes populated with electrons exited from the valence band. This higher excitation rate causes the inversion of the conduction band, as if the semiconductor electrode is biased by an external negative potential, where the majority charge carriers in *n*-type semiconductors (electrons) recombine with the minority charge carriers (holes) before reaching the interface semiconductor-electrolyte⁹⁹ as seen in figure 3.10.

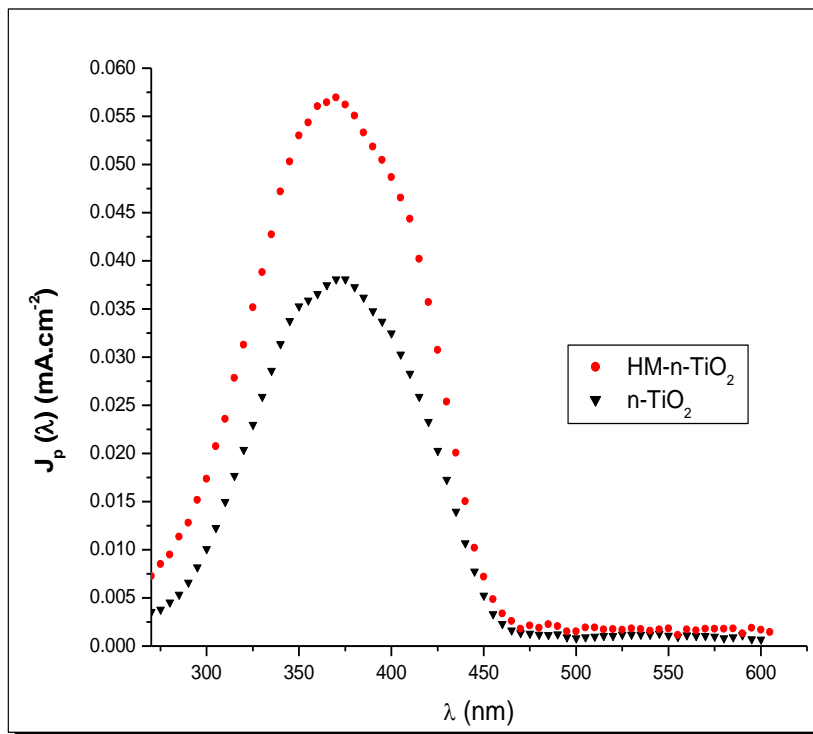


Figure. 3.9 Monochromatic photocurrent density, $j_p(\lambda)$, as a function of wavelength of light, λ (nm), for unmodified *n*-TiO₂ and HM-*n*-TiO₂. The monochromatic photocurrent measurements were performed under monochromatic light intensity of 0.1 W cm⁻² from a global AM 1.5 solar simulator and 2.5 M KOH as electrolyte. The measured potential used was set at 0.2 V/SCE.

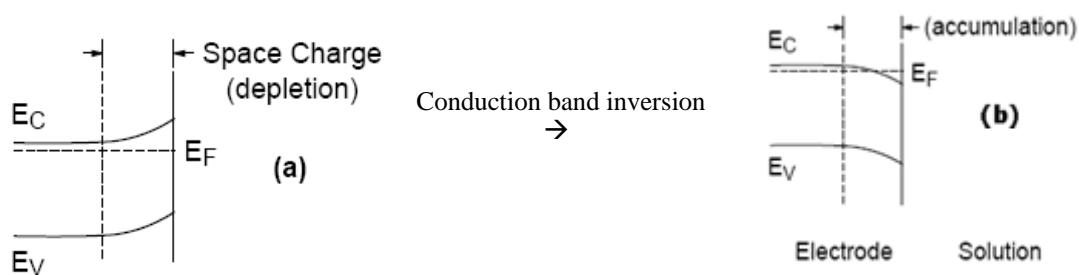


Figure 3.10 Conduction band inversion at the interface n-type semiconductor – electrolyte when a negative bias is applied.

3.1.4 Band gap energy of HM-*n*-TiO₂ thin films:

Figure. 3.11 shows Tauc plot of $(\eta h\nu)^{1/2}$ versus $(h\nu)$ for HM-*n*-TiO₂ and *n*-TiO₂.

Note that η is the quantum efficiency calculated using the formula:

$$\eta(\lambda) = \frac{j_p(\lambda)}{eI_0(\lambda)} \quad (16)$$

where $j_p(\lambda)$ is the wavelength dependent photocurrent density, e is the electronic charge, $I_0(\lambda)$ is wavelength dependent intensity of incident light, and $(h\nu)$ represents frequency dependant photon energy.

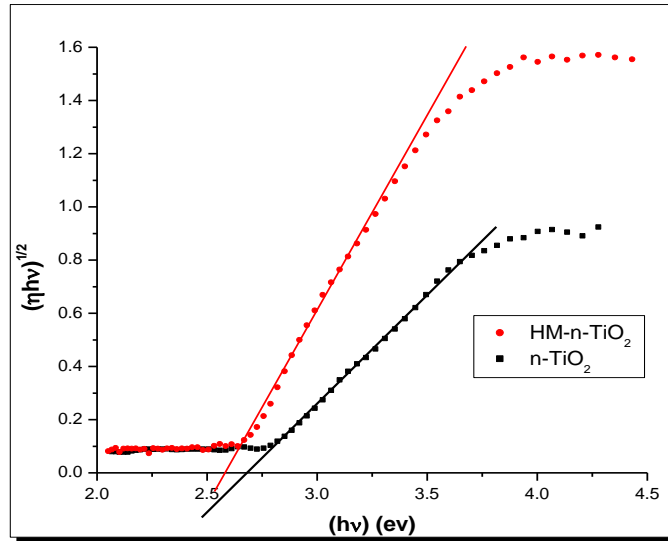


Figure 3.11 The respective plots of $(\eta h\nu)^{1/2}$ vs. $(h\nu)$ to determine the band gap of HM-*n*-TiO₂ and undoped *n*-TiO₂ thin films. The measurements were performed under monochromatic light with an intensity of 0.1 W cm^{-2} from a solar simulator with global AM 1.5 and 2.5 M KOH electrolyte.

An extrapolation of the linear regions of the plots, $(\eta h\nu)^{1/2}$ versus $(h\nu)$ for both electrodes, gives the band gap value as the intercept to the horizontal axis (where $(\eta h\nu)^{1/2} = 0$). From the extrapolation, the band gap of HM-*n*-TiO₂ was found to be slightly narrower from 2.7 eV for regular *n*-TiO₂ to 2.6 eV. It is worthwhile to note that the band

gap of 2.7 eV for n -TiO₂ thin film was found to be lower than that of n -TiO₂ particles.¹⁰⁰

This may be attributed to a very low level carbon doping by ambient CO₂ in the electric furnace when n -TiO₂ was synthesized as reported in section 2.1.

3.1.5 Summary:

We have demonstrated a simple approach to incorporate hydrogen into n -TiO₂ (to synthesize HM- n -TiO₂) by electrochemically generating hydrogen gas onto its surface under cathodic polarization at room temperature. The photo-catalytic activity of HM- n -TiO₂ towards water splitting was enhanced by four fold compared to regular n -TiO₂.

3.2 Carbon modified (CM)- n -TiO₂ thin film electrodes:

3.2.1 Surface morphology and structure characterization of n -TiO₂ and CM- n -TiO₂ thin films:

Figure 3.12 compares the surface morphologies of CM- n -TiO₂ thin film synthesized by thermal flame oxidation of Ti metal substrate and regular n -TiO₂ thin film synthesized by thermal oxidation in an electric furnace under ambient atmosphere as reported in the experimental section 2.2. SEM images of the surface reveal that the major difference in the samples is the surface morphology and consequently the enhanced surface area and multiple absorption of reflected light across the nanostructures. CM- n -TiO₂ thin film has a rough surface compared to a nearly flat surface of the regular n -TiO₂. The morphology of CM- n -TiO₂ consists of sharp edges with wall like nano-and-micro structures. These wall-like structures are vertically oriented and some of them appear to have collapsed due to the flame's heat. Flame oxidation of Ti metal produces an oxide

thin film with sharp edges; however it is not known whether the dramatic change in surface morphology is due to the presence of carbon in the surface/structure of the titanium oxide or from the flame environment.

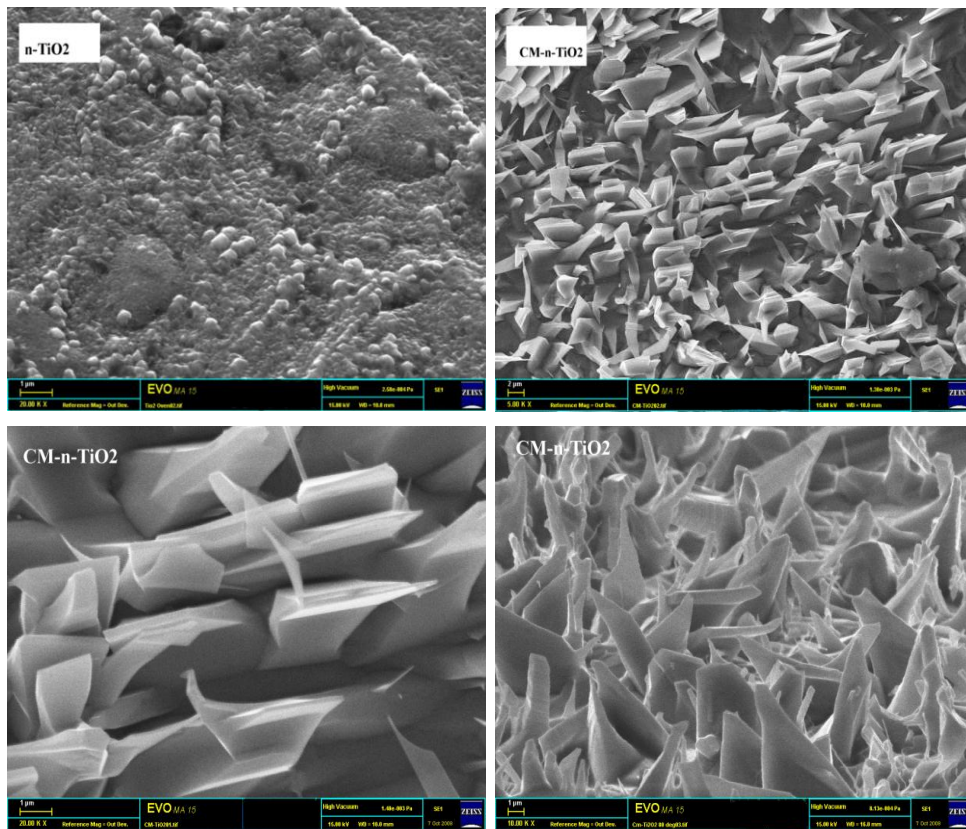


Figure. 3.12 Top view SEM images of flame oxidized CM-*n*-TiO₂ thin films and undoped *n*-TiO₂ thin films.

3.2.2 Elemental analysis of CM-*n*-TiO₂ thin films using EDS:

Figure 3.13 shows EDS spectra of the catalyst which includes a combination of surface morphology and the elemental distribution of C, Ti, and O in CM-*n*-TiO₂ thin film. The catalyst's color changes depending on the thermal oxidation method from gray for furnace oxidized *n*-TiO₂ to dark gray for flame oxidized CM-*n*-TiO₂ samples.

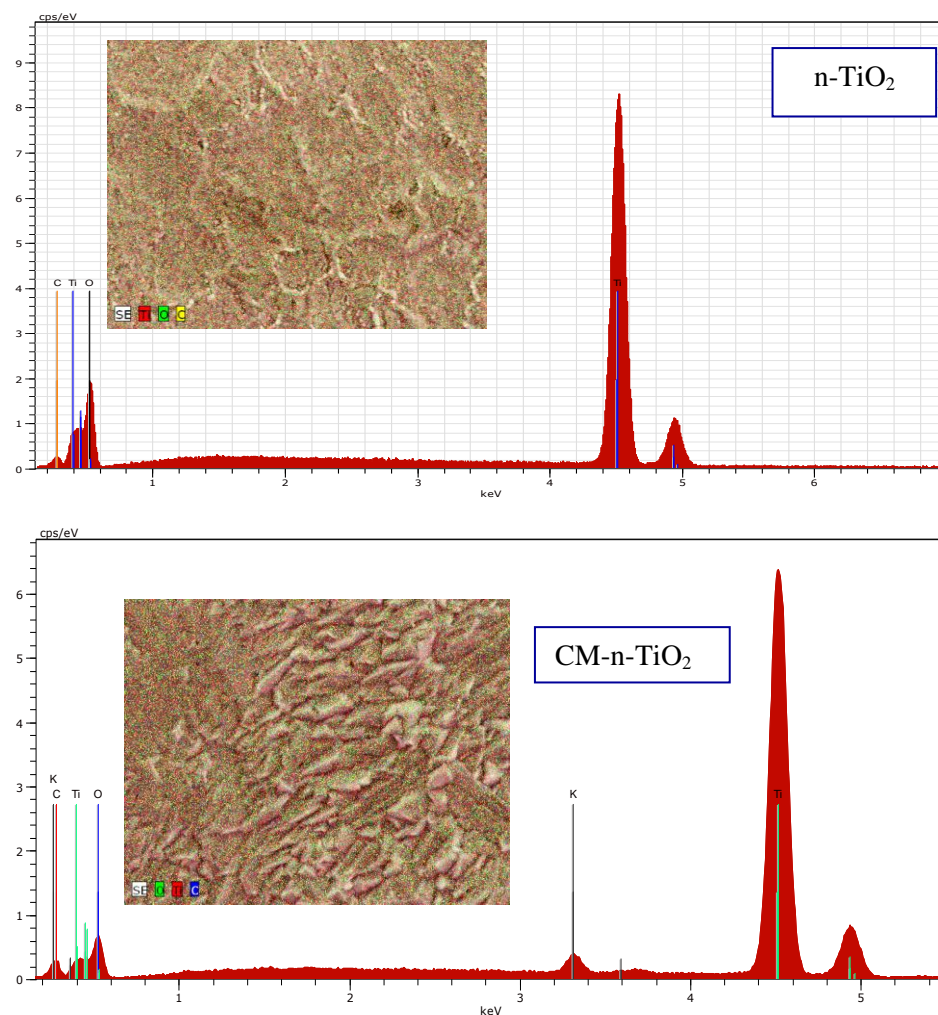


Figure 3.13 Elemental mapping and EDS spectra of $\text{CM-}n\text{-TiO}_2$ and $n\text{-TiO}_2$ showing the surface elemental distribution.

Elemental composition of $\text{CM-}n\text{-TiO}_2$ showed variation from one sample to another. The surface composition of $\text{CM-}n\text{-TiO}_2$ was taken for different selected samples and the atomic percent of Ti, O, and C are given in Table 1. The standard deviations of the atomic percent of Ti, O and C were found to be 6.6%, 6.2% and 2.6%, respectively. This variation in the surface composition results lead to investigate a single sample where the EDS measurements were taken at different surface spots and over large cross sectional area (lower magnification) as seen in Table 2. The carbon atomic percent of Ti,

O and C decreases as the cross sectional area increases as shown in Table 2, this is possibly due to the presence of residual carbon in different spots as shown in Fig. 3.14.

Table 1. EDS analysis and surface composition of n -TiO₂ and CM- n -TiO₂

<i>Elements Atom %</i>	<i>Unmodified n-TiO₂</i>	<i>Carbon modified CM-n-TiO₂</i>	
		<i>Composition</i>	<i>Sd</i>
Ti	40.55	38.95	6.6
O	57.78	56.70	6.2
C	1.67	3.50	2.2

Table 2. EDS analysis and surface composition of a single sample CM- n -TiO₂

<i>Elements Atom %</i>	<i>CM-n-TiO₂</i>			
	<i>Magnification 1</i>		<i>10×</i>	<i>50×</i>
	<i>Composition</i>	<i>Sd</i>	<i>Composition</i>	<i>Composition</i>
Ti	43.91	5.6	41.03	41.42
O	52.2	7.6	56.59	56.56
C	3.30	1.6	2.17	1.78

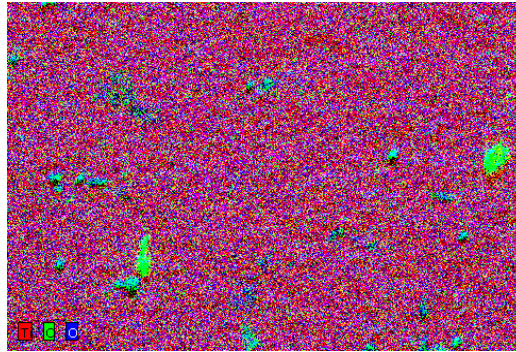


Figure 3.14 Elemental mapping for CM- n -TiO₂ thin film over a large cross sectional area (low magnification) with red for Ti atoms, blue for O atoms and green for C atoms.

3.2.3 X-ray diffraction (XRD) of n -TiO₂ and CM- n -TiO₂ thin films:

X-ray diffraction (XRD) analysis was carried out to characterize the structure of CM- n -TiO₂ thin film photoelectrodes synthesized by flame oxidation of Ti metal sheets.

Figure 3.15 shows the XRD patterns of the CM-*n*-TiO₂ and *n*-TiO₂ thin films; the strong XRD diffraction peaks observed signify that the thin film of CM-*n*-TiO₂ and *n*-TiO₂ are highly crystalline and consists mainly of rutile phase with some peaks belong to the anatase. The peak at 53° 2θ may belong to Ti metal or to the non stoichiometric titanium oxide^{101, 97} such as Ti₃O (jcpds: 01-073-1583) and Ti₆O (jcpds: 01-072-1471).

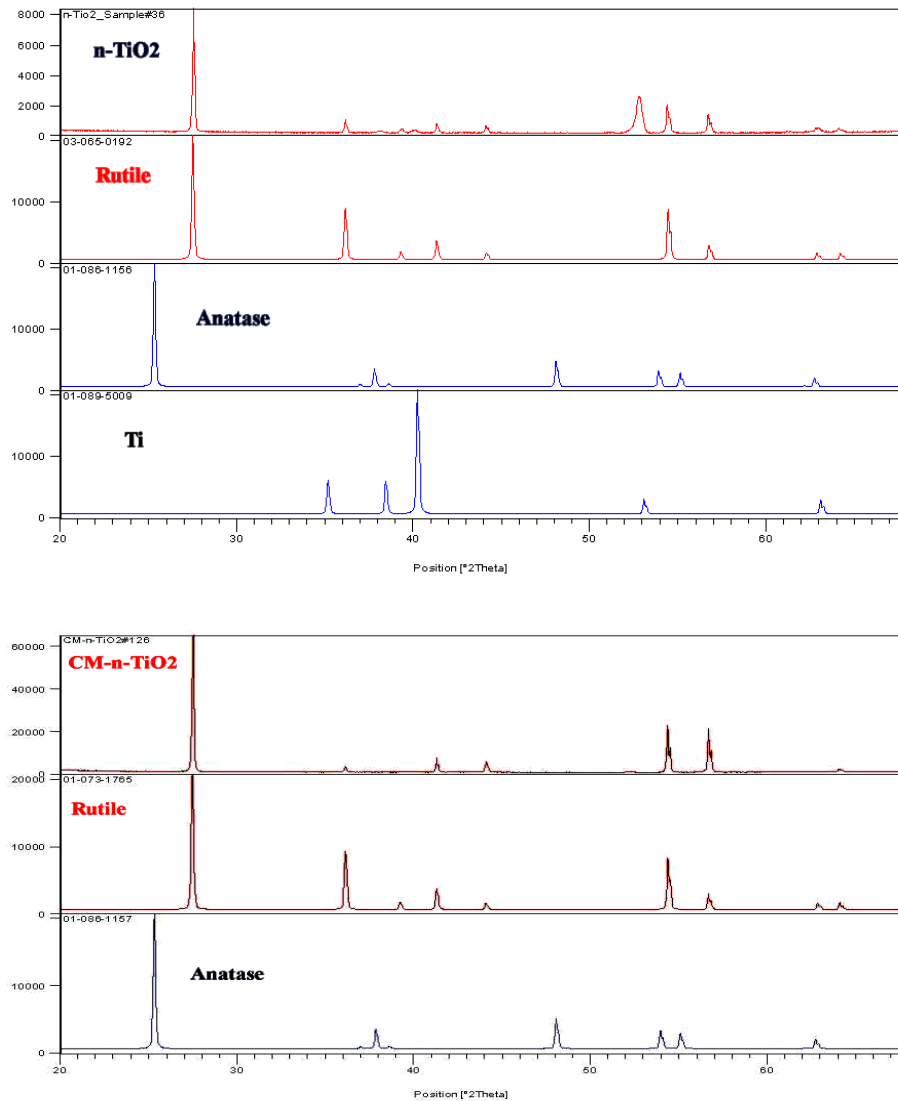


Figure 3.15 Xray diffraction (XRD) patterns for *n*-TiO₂ and CM-*n*-TiO₂ thin films compared to reference patterns (jcpds cards) of Rutile (03-065-0192, 01-073-1765); Anatase (01-086-1156, 01-086-1157); and Ti (01-089-5009)

3.2.4 Photoelectrochemical water splitting at CM-*n*-TiO₂ electrodes under an external minimal bias:

The photoacatalytic activity of CM-*n*-TiO₂ electrodes was investigated in terms of photocurrent density (mA cm⁻²) which is proportional to the amount of molecular oxygen evolved at the surface of the semiconductor electrode. According to faradays law the current density is proportional to the number of moles of oxygen evolved at the electrode surface, therefore it can be calculated using the equation:

$$j = zFn_{O_2} \quad (17)$$

where F is the Faraday constant (F= 85600 C/mol), z is the number of electrons (water splitting is a four electrons process) and n_{O_2} is the number of moles of O₂ evolved.

Figures 3.16 is the plot of the photocurrent density versus measured potential for an efficient CM-*n*-TiO₂ synthesized at the optimum conditions (flame temperature of 825 ± 3°C, thermal oxidation time of 15 min, optimum oxygen gas flow rate of 2.23 L min⁻¹ and the natural gas flow rate of 3.32 L min⁻¹) compared to undoped *n*-TiO₂ synthesized in an electric tube furnace under the optimum conditions (temperature of 825 ± 3°C and oxidation time of 16 min). A photocurrent density of 4.97 mA cm⁻² was observed for CM-*n*-TiO₂ thin films at a measured potential of - 0.6 V/SCE compared to 0.66 mA cm⁻² for *n*-TiO₂ at the same measured potential. This enhancement in the photocurrent is a clear indication of the positive effect carbon incorporation has on the photoresponse of titanium oxide.

The wall-like sharp structures as seen in the SEM micrograms (Fig. 3.12) provide an insight into how carbon, as impurity, modifies the surface morphology of the catalyst. In catalytic reactions a large contact area is highly desirable in order to increase the yield

of the chemical reaction. More importantly, in photoactive semiconductor electrocatalysts textured surfaces play a decisive role in facilitating charge transfer at the electrode-electrolyte interface by reducing the diffusion length for charge carriers compared to a flat surface and thus minimize their recombination rate.^{102, 103} The added benefit of a porous or rough surface morphology is that the incident light is more effectively absorbed due to light scattering within porous structures^{104, 105}, and therefore a better photoresponse compared to a flat surface.^{102, 103} It was also found that the nano-structured morphology facilitate the gas bubble evolution compared to a flat catalytic surfaces where the gas bubbles stick to the surface until a sudden burst occurs.^{106, 107}

The photocurrent density is proportional to the thickness of the oxide film¹⁰⁸, as shown in the theoretical expression [18]. On this basis a thicker oxide film would result in higher absorption of light and consequently a higher photocurrent:¹⁰⁸

$$I_{ph} = \Gamma_0(1 - R)(1 - e^{\frac{-(\alpha w)}{(1 + \alpha L_p)}}) \quad (18)$$

where, Γ_0 is the incident photon flux, R is the optical reflectivity of the solid, L_p is the hole diffusion length (i.e., the minority carrier diffusion length in n -type semiconductor) and α is the linear light absorption coefficient. w is the depth of the space charge region and can be described as follow:

$$w = \sqrt{\frac{2\varepsilon\varepsilon_0(E - E_{onset})}{qN_D}} \quad (19)$$

where ε is the static dielectric constant, ε_0 is the permittivity of free space (8.86×10^{-14} F cm⁻¹), $E - E_{onset}$ is the potential drop in the space charge region (E_{onset} is the potential at which the anodic current is first observed), N_D is the concentration of donor impurities in a semiconductor (in the case of TiO₂; $N_D = n_e$), and q is the electron charge (1.6×10^{-19} C). Note that the photocurrent increases with the width of the space charge region which

in fact depend on the effective absorption of light, carrier density and the bend bending in the semiconducting photoelectrode.

According to the experimental results, and assuming that the oxide film thickness is proportional to the oxidation time, the photocurrent versus oxidation time trends were found to follow equation (18) when the Ti metal samples were flame oxidized for periods equal to or less than 15 min, as seen in Figure 3.17. Whereas, for thicker CM-n-TiO₂ thin films the photocurrent was found to decrease when the oxidation time was greater than 15 min. This anomaly in the photocurrent versus film thickness trend could be explained as follow: for longer oxidation times the CM-n-TiO₂ film is exposed to the extra heat which may cause the film to crack and pills off the underneath electrons collector substrate (Ti metal).

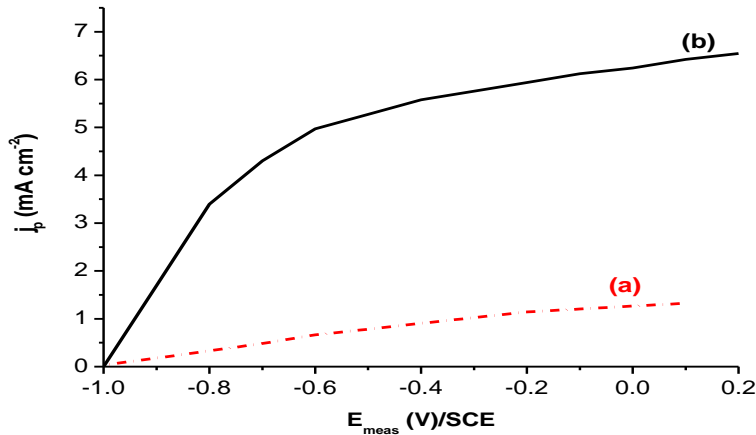


Figure 3.16 Photocurrent density as a function of measured potential, E_{meas} (V/SCE) under light intensity of 0.1 W cm^{-2} from a global AM 1.5 solar simulator and in 5 M KOH electrolyte, (a) Photocurrent density for n-TiO₂ (b) Photocurrent density for CM-n-TiO₂.

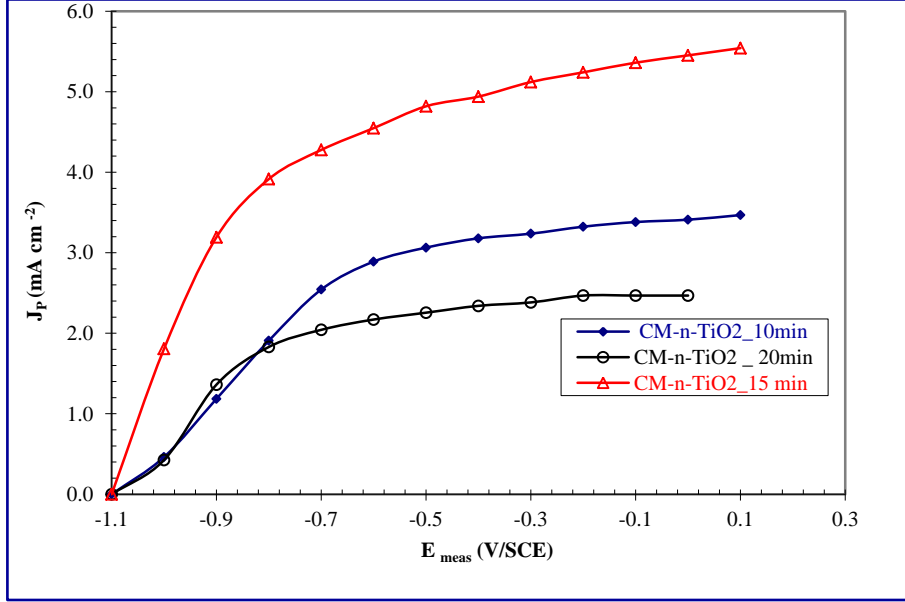


Figure 3.17 Photocurrent density as a function of measured potential, E_{meas} (V/SCE) for CM-n-TiO₂ thin film electrodes synthesized by thermal flame oxidation at the optimum condition of flame temperature and different oxidation times. The measurements were performed under light intensity of 0.1 W cm^{-2} from a global AM 1.5 solar simulator, and in 5 M KOH electrolyte.

3.2.5 Photoconversion efficiency of CM-n-TiO₂ and n-TiO₂ thin film electrodes

under an external minimal bias:

The percent photoconversion efficiencies, ε (%), of the photoelectrodes were calculated using expression: ¹⁵

$$\begin{aligned} \varepsilon (\%) &= \left[\frac{(\text{Output Power} - \text{input Power})}{\text{Incident light Power}} \right] \times 100\% \\ &= \left[j_p \frac{(E_{\text{rev}} - |E_{\text{app}}|)}{P_0} \right] \times 100\% \end{aligned} \quad (20)$$

where j_p is the photocurrent density (mA cm^{-2}); P_0 is the total incident light intensity (0.1 W cm^{-2}); E_{rev} is the reversible potential (1.23 V) for the overall water splitting reaction:



at standard state conditions which can be interpreted as the chemical energy consumed by

converting H₂O to H₂ and O₂; and E_{app} is the applied potential which is calculated as

$$E_{app} = E_{meas} - E_{aoc} \quad (22)$$

where E_{meas} (vs. SCE) is the potential at which the photocurrent density was measured; E_{aoc}(vs.SCE) is the electrode potential at open circuit conditions in the same electrolyte solution under the same illumination at which the photocurrent density was measured.

Due the unfavorable position of the conduction band of *n*-TiO₂, an applied potential from an external source such as a potentiostat is required to drive the water splitting reaction at *n*-TiO₂ anode. In addition to the electric field generated inside the semiconductor under light illumination an externally applied potential is needed to effectively separate the electron – hole pairs. The applied potential needs to be subtracted from the output energy in order to calculate the photoconversion efficiency of the electrode.

Alternatively, the percent total photoconversion efficiency (% ε_{photo(total)}) of light energy to chemical energy can be obtained by the following equation:¹⁵⁵

$$\% \varepsilon_{photo(total)} = \frac{\int_{\lambda_{min}}^{\lambda_g} j_p(\lambda) [E_{rev}^o - |E_{app}(\lambda)|] d\lambda}{\int_{\lambda_{min}}^{\infty} P_o(\lambda) d\lambda} \times 100 \quad (23)$$

where j_p(λ) is wavelength dependent photocurrent density under monochromatic light illumination (mA cm⁻² nm⁻¹) and P_o(λ) is the power density of incident wavelength dependent monochromatic light (mW cm⁻² nm⁻¹). The applied potential, E_{app}(λ) was also found to be wavelength dependent and can be expressed as,

$$E_{app}(\lambda) = E_{meas} - E_{aoc}(\lambda) \quad (24)$$

where $E_{\text{aoc}}(\lambda)$ is the electrode potential in volts at open circuit conditions under monochromatic light illumination of wave length, λ (nm). Since E_{aoc} depends on the incident light intensity % ϵ_{photo} (total) is calculated based on equation [24].

Photoconversion efficiency was also calculated with the assumption that the cathode (Pt as counter electrode) has a fixed potential ¹⁰⁹ and can be estimated as the reduction potential of water in basic media (-0.83V/NHE):



In this case the applied potential can be obtained as:

$$E_{\text{app}} = E_{\text{anode}} - E_{\text{cathode}} = E_{\text{meas}} - E^\circ(\text{H}_2\text{O}/\text{H}_2) \quad (26)$$

Where $E^\circ(\text{H}_2\text{O}/\text{H}_2) = -1.013\text{V}/\text{SCE}$ in a 5 M KOH solution. But it should be noted that the dependence of the open circuit potential (E_{aoc}) of the photo-anode ($n\text{-TiO}_2$) on the incident light (equation [24]) should not be ignored and needs to be taken into account.

For CM- $n\text{-TiO}_2$, a photoconversion efficiency of 4.06% (see Fig. 3.18) was found for water splitting under an external applied potential of 0.41 V versus E_{aoc} (which corresponds to a measured potential, $E_{\text{meas}} = -0.7\text{V}/\text{SCE}$) compared to 0.55% for undoped $n\text{-TiO}_2$ (see Fig. 3.18) under an external applied potential of 0.52 V versus E_{aoc} . It is observed in Fig. 3.16 and Fig. 3.18 that higher photocurrent response and consequent higher photoconversion efficiency (4.06%) of CM- $n\text{-TiO}_2$ samples was determined by the unusually higher ability of the oxide to use the absorbed UV photons to convert OH^- ions to O_2 and water as shown in Fig. 3.19. Such unusual behavior of CM- $n\text{-TiO}_2$ samples mainly in the UV regions may be explained in terms of the following effects. A possible multielectron-hole pairs (excitons) generation (MEG) by absorption of single high energy photons in the UV region across multiple low energy band gaps in the CM- $n\text{-TiO}_2$ nanocrystals (Ncs), as it is observed in its scanning electron microgram (see Fig. 3.12).

The multi-exciton generation (MEG) by a single photon was observed earlier in Ncs.^{110, 111, 112}

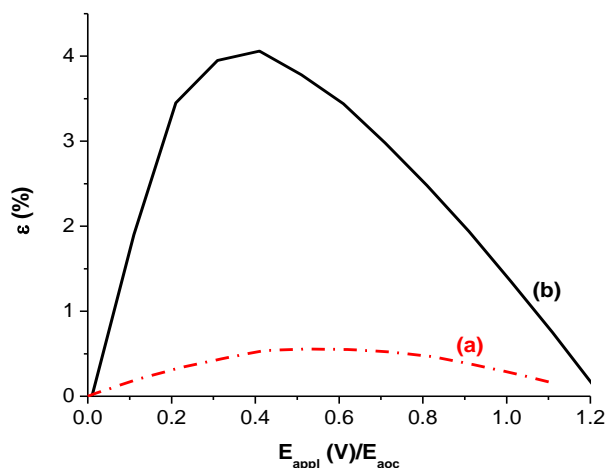


Figure 3.18 Photoconversion efficiency as a function of applied potential E_{app} (V/E_{aoc}) under light intensity of 0.1 W cm^{-2} from a global AM 1.5 solar simulator in a 5 M KOH electrolyte. (a): $n\text{-TiO}_2$ and (b): $\text{CM-}n\text{-TiO}_2$.

3.2.6 Monochromatic photocurrent density for $n\text{-TiO}_2$ and $\text{CM-}n\text{-TiO}_2$:

To investigate the photoactivity of $\text{CM-}n\text{-TiO}_2$, the monochromatic photocurrent density, $j_p(\lambda)$, has to be measured at various wavelengths, λ (nm). The monochromatic photocurrent has a significant advantage over the absorbance spectra in the UV-Vis region due to electronic transition not related to the band gap such as d-d transition.⁹⁸ measured at an applied potential of 0.2 V/SCE

Figure 3.19 shows that the photoactivity of $\text{CM-}n\text{-TiO}_2$ compared to that of undoped $n\text{-TiO}_2$ increased mainly in the UV region of the incident solar simulated light when measured under the same experimental conditions. More importantly a visible light activity of the $\text{CM-}n\text{-TiO}_2$ was also observed. This observation was found to be consistent with the diffuse reflectance spectra of $\text{CM-}n\text{-TiO}_2$ as seen in figure 3.20. The dramatic increase of the photoactivity of $\text{CM-}n\text{-TiO}_2$ in the UV region of the incident

light could be due to an effective absorption of the incident light where light is readily scattered within a porous or rough surface. Another reason is a possible formation of a mid gap band due to carbon doping where electrons are excited from the valence to the newly created mid gap band and from the later to the conduction band of the CM-*n*-TiO₂ electrode.

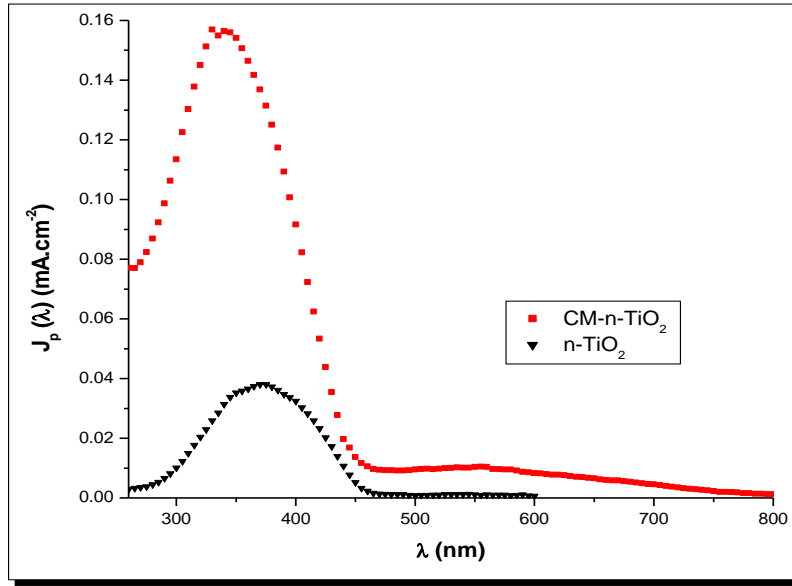


Figure. 3.19 Monochromatic photocurrent density, $j_p(\lambda)$, as a function of λ (nm), for undoped *n*-TiO₂ and CM-*n*-TiO₂. The measurements were performed under a monochromatic light from a solar simulator with global AM 1.5 filter in 5 M KOH and under a potential of 0.2 V/SCE.

A low photocurrent generation in the more energetic wave lengths of UV region was observed and could be due to the low efficiency of charge carrier's collection.⁹⁹ This phenomenon can be explained by the fact that under a highly energetic wave length of the UV region, the conduction band of the semiconductor becomes populated with excited electrons from the valence band. This higher excitation rate causes the inversion of the conduction band, as if the semiconductor electrode is biased by an external negative

applied potential. This inversion in conduction band causes the majority charge carriers in *n*-type semiconductor (electrons) recombine with the minority charge carriers (holes) before reaching the interface semiconductor-electrolyte⁹⁹ (Fig. 3.10).

3.2.7 Diffuse reflectance spectra of CM-*n*-TiO₂ and *n*-TiO₂ thin films:

Figure 3.20 compares the UV-Vis diffuse reflectance spectra of flame-made CM-*n*-TiO₂ and regular *n*-TiO₂ photoelectrodes having maximum photoconversion efficiencies of 4.06 % and 0.55 %, respectively. Both electrodes were synthesized at the same optimum conditions of 825 °C for 15 min. The UV-Vis spectroscopic results show similar behavior of the flame-made CM-*n*-TiO₂ and *n*-TiO₂ thin films in the UV region. However, a visible light absorption is observed for CM-*n*-TiO₂ with a peak at 580 nm. The UV-Vis spectra are consistent with the monochromatic photocurrent for CM-*n*-TiO₂ and *n*-TiO₂ thin films as shown in figure 3.19.

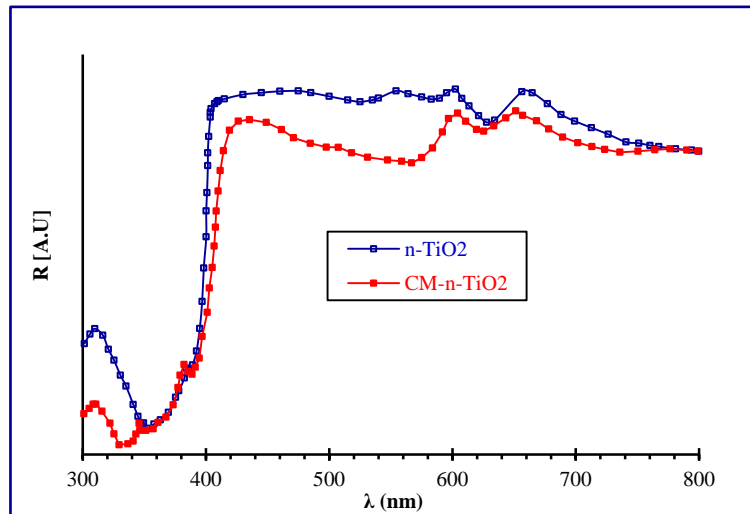


Figure 3.20 Diffuse reflectance spectra for undoped *n*-TiO₂ and CM-*n*-TiO₂.

3.2.8 Band gap energy of CM-*n*-TiO₂ thin film:

Figure 3.21 shows Tauc plot of $(\eta h\nu)^{1/2}$ versus $(h\nu)$ for CM-*n*-TiO₂ and *n*-TiO₂ thin films. Note that η is the quantum efficiency calculated using equation [16]. An extrapolation of the linear regions of the plots, $(\eta h\nu)^{1/2}$ versus $(h\nu)$ for both electrodes, gives the band gap value as the intercept to the horizontal axis (where $(\eta h\nu)^{1/2} = 0$).

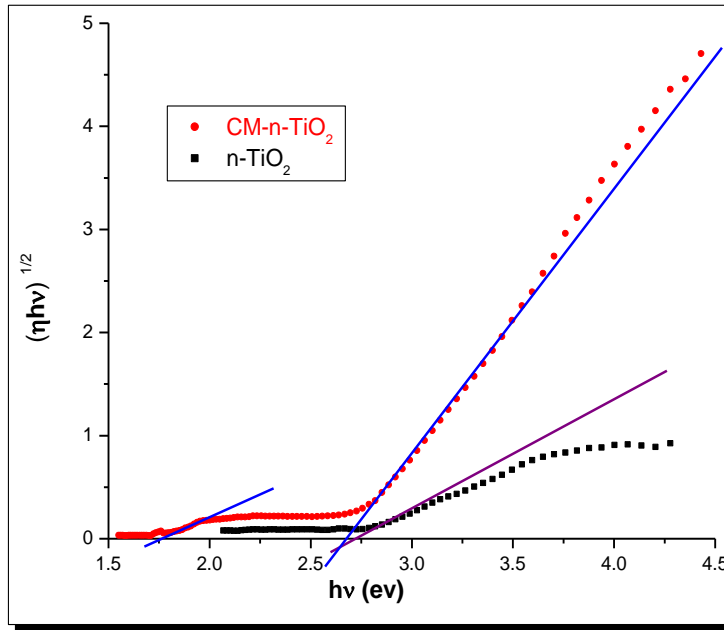


Figure 3.21 The respective plots of $(\eta h\nu)^{1/2}$ vs. $(h\nu)$ to determine the band gap of CM-*n*-TiO₂ and undoped *n*-TiO₂ thin films. The measurement were performed under a light intensity of 0.1 W cm^{-2} from a global AM 1.5 solar simulator in 5 M KOH electrolyte.

From the extrapolation the band gap of CM-*n*-TiO₂ was found to be 2.61 eV, which is narrower than that of regular rutile TiO₂ (3.0 eV). In addition, a mid-gap band located 1.75 eV above the valence band was observed within the band gap of CM-*n*-TiO₂. And this is due to carbon incorporation within the lattice or surface of CM-*n*-TiO₂. The band gap for the electric furnace made *n*-TiO₂ was found to be 2.75 eV which is lower

than the expected 3.0 eV. 100 This anomaly may be attributed to very low level carbon doping by ambient CO₂ in the electric tube furnace. It can be concluded that the high photocurrent response observed for the CM-*n*-TiO₂ compared to undoped *n*-TiO₂ (Fig. 3.16) is due to band gap lowering and the formation of a mid-gap band within the band gap of the CM-*n*-TiO₂ thin film.

3.2.9 AC impedance spectroscopy: flat band potentials and doping densities of CM-*n*-TiO₂ and *n*-TiO₂ thin films:

Since the carbon modification of titanium oxide influenced the catalytic activity of the photocatalyst during water oxidation, it is also important to examine whether the flat potential of CM-*n*-TiO₂ would be affected by carbon implantation on the surface or the lattice of the thin film electrode. The behavior of the catalysts under AC frequencies was investigated with Electrochemical Impedance Spectroscopy (EIS). This study was conducted in order to evaluate the flat band potentials and the doping densities of *n*-TiO₂ and CM-*n*-TiO₂ thin films.

In linear sweep voltametry the external applied potential between the two electrodes is linear with respect to time and the resulting DC current from the chemical reaction has an ohmic relationship with the applied potential. When the external applied potential is not linear but rather solenoid ($E = \Delta E \sin \omega t$) then the subsequent current would be sinusoidal with a value $I = \Delta i \sin(\omega t + \phi)$. The new relationship between the current and the applied potential is known as the impedance which is analogous to the resistance-current- potential relationship in a DC circuit. Therefore the impedance:

$$Z = E(t)/i(t) = \Delta E \sin \omega t / \Delta i \sin(\omega t + \varphi) \quad (27)$$

has a magnitude ($Z_o = \Delta E / \Delta i$) and a phase shift (φ) and thus a vector quantity.

The impedance $Z(\omega)$ is then expressed as a complex number:

$$Z(\omega) = Z_o(\cos \varphi + j \sin \varphi) \quad (28)$$

The expression for $Z(\omega)$ is composed of a real and an imaginary part such as

$$Z = Z' + jZ'' \quad (29)$$

where Z' is the real part of the impedance and Z'' is the imaginary part of the impedance.

Plotting the imaginary part versus the real part gives a chart which is called a "Nyquist Plot" (see Fig. 3.22). Notice that in this plot the Y-axis is negative and that each point on the Nyquist Plot is the impedance at one frequency.

The data was recorded in the frequency range of 10 kHz to 5 mHz; an AC amplitude of 10 mV was used in all measurements; a Pt mesh electrode was used as the counter electrode and either the CM-*n*-TiO₂ or *n*-TiO₂ thin films were used as the working electrode. These measurements were carried out in the dark in 2.5 M KOH solution. The capacitance, C , was calculated from the expression of impedance, Z , for a series of capacitor-resistor model. The capacitance C can be obtained using:

$$Z'' = -j/\omega C \quad (30)$$

with $\omega = 2\pi f$, $j = (-1)^{1/2}$, and f is the AC frequency in Hertz. The values of Z'' at different AC frequencies were obtained from the Nyquist plot (Z'' versus Z') generated from the measured data of impedance, $|Z|$, using VersaStudio software as shown in figure 3.22 with the equivalent RC circuit. R_∞ is the solution resistance, R_2 is the charge transfer resistance and C_2 is the double layer capacitance. Note that the equivalent model is based

on the space charge (electrode surface-electrolyte) capacitance (C_2) and the charge transfer resistance (R_2).

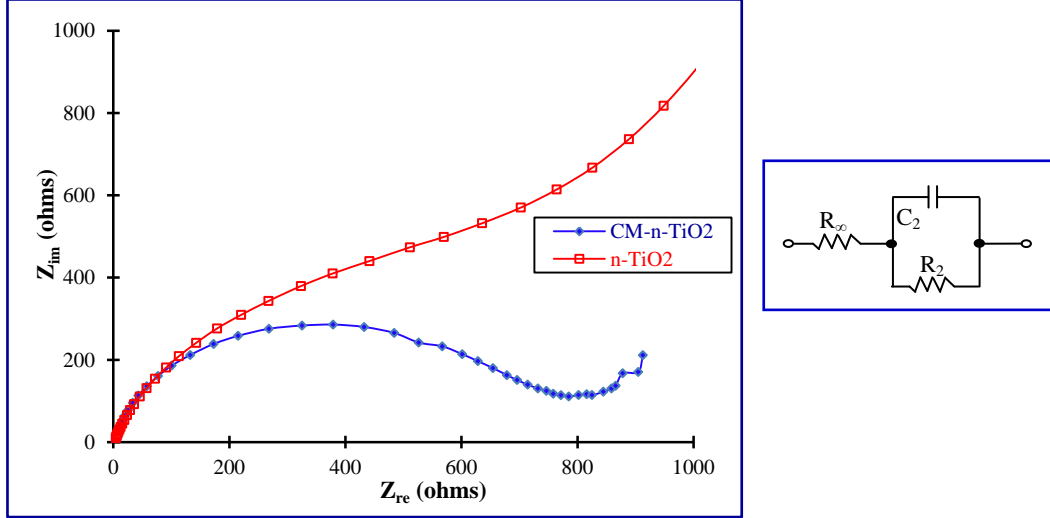


Figure 3.22 Nyquist plot for CM- n -TiO₂ and n -TiO₂ thin films electrodes measured in 2.5 M KOH in dark conditions with the equivalent RC circuit.

It is well known that the flat band potential (E_{fb}) of a semiconductor can be obtained from the intercept of the Mott-Schottky plot using the following expression:

$$1/C^2 = (2/e_o \epsilon \epsilon_o N_d)(E_{app} - E_{fb} - kT/e_o) \quad (31)$$

where ϵ is the dielectric constant of the semiconductor; ϵ_o ($8.85 \times 10^{-12} \text{ F m}^{-1}$) is the permittivity of the vacuum; N_d is the donor density; E_{app} is the applied potential, and kT/e_o is the temperature-dependent term in the Mott-Schottky equation.

In Figure 3.22 the differences between the photocatalysts can be seen where the diameter of the Nyquist plot for CM- n -TiO₂ is smaller than that for n -TiO₂. The diameter of the Nyquist plot is closely related to the charge transfer rate. A small diameter of a Nyquist plot for CM- n -TiO₂ indicates that the nanostructured surface shows a lower charge transfer resistance than that of the n -TiO₂ flat surface.

Figure 3.23 shows the capacitance-potential characteristics in a Mott–Schottky plot of the CM-*n*-TiO₂ and *n*-TiO₂ thin film electrodes at various AC frequencies in 2.5 M KOH electrolyte solution in the dark. It is well known that the slopes of the straight lines of the Mott-Schottky plots are AC frequency dependent; however, this dependence has not been fully understood except that the dielectric relaxation of the semiconductor has been proposed as the origin of such phenomena.¹¹³ In Figure 3.23, straight lines are observed at all the AC frequencies used for the measurement of impedance; however, for frequencies under 5 kHz the dispersion of the slopes of Mott-Schottky plots become highly pronounced. Thus we limited our study to AC frequencies equal to or higher than 5KHz. The positive slop indicates that the semiconductor is *n*-type. The intercept of the straight line of Mott-Schottky plot with the potential axis for *n*-TiO₂ thin film was found between -0.81and -0.83V/SCE including the kT/e_0 term. However, an intercept at around -1V/SCE was observed for CM-*n*-TiO₂. A negative shift of the flat band potential was observed in CM-*n*-TiO₂ compared to the pristine *n*-TiO₂ thin film electrode. This finding suggests that the flat band potential depends on the chemical modification of the semiconductor.

The doping density of the thin films was calculated from the slope of the straight line of the Mott-Schottky plot ($2/e_0\epsilon\epsilon_0N_d$) where $\epsilon = 60$ for intrinsic *n*-TiO₂.¹⁰⁸ The average doping density of *n*-TiO₂ at AC frequencies between 5 and 10 kHz was found to be $2.45 \times 10^{16} \text{ cm}^{-3}$ which is typical for a semiconductor electrode. However, this value was unexpectedly higher than that of CM-*n*-TiO₂ which was found to be $1.36 \times 10^{16} \text{ cm}^{-3}$. A higher doping density for pristine *n*-TiO₂ could be due to the presence of oxygen vacancies in the pristine *n*-TiO₂ thin film.¹⁰¹ Under external polarization these vacancies

will be filled with adsorbed species from the electrolyte leading to higher surface state compared to CM-*n*-TiO₂.

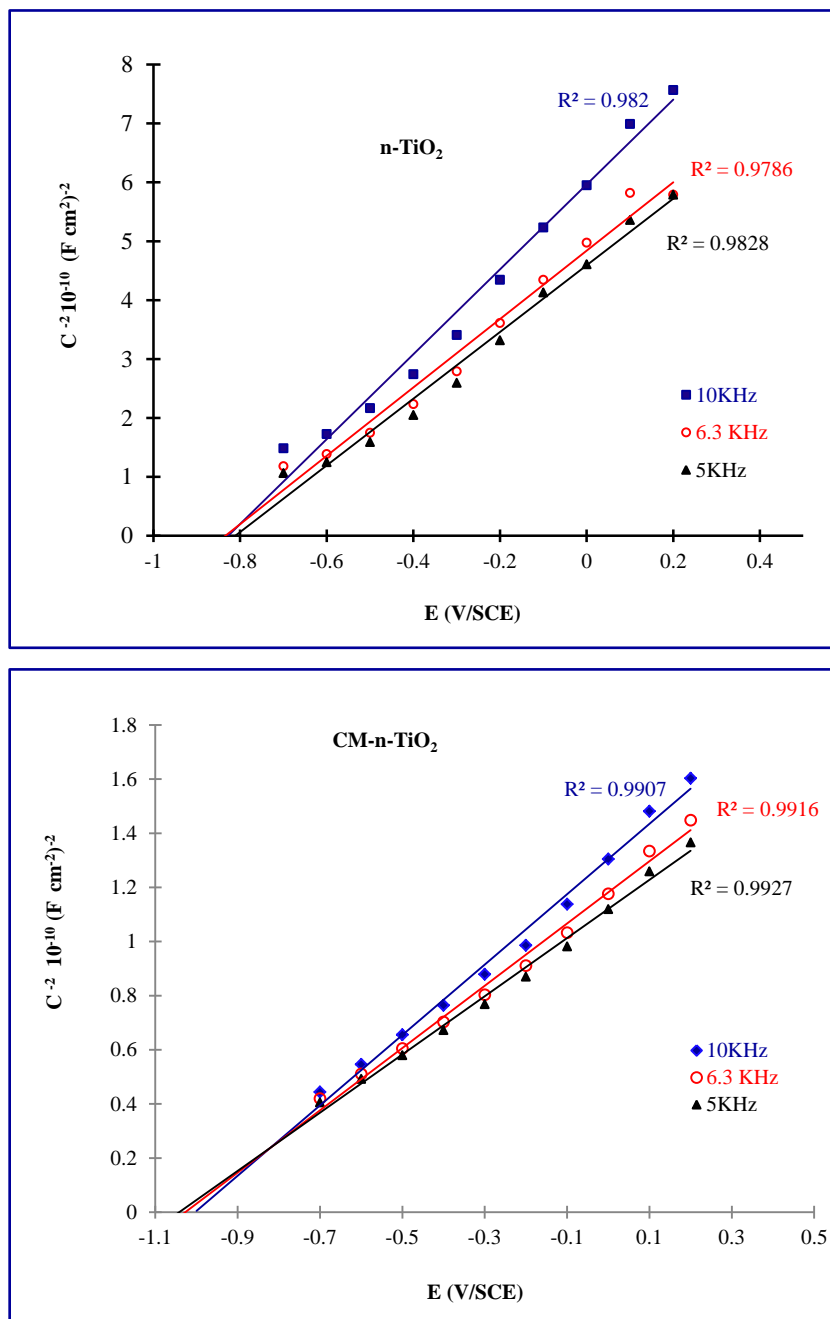


Figure 3.23 Mott-Schottky plot of *n*-TiO₂ and CM-*n*-TiO₂ thin films measured at various AC frequencies. 10 mV AC amplitude, 2.5 M KOH electrolyte measured in dark.

3.2.10 Effect of surface modification by metal islets on the photoactivity of

CM-*n*-TiO₂ thin film electrodes:

Previous studies on the surface modification of several photocatalyst electrodes^{114, 115, 116} showed that electrodeposition of metal islets (Pt, Ni, Ru,...) on the surface of *p*-type semiconductors such as *p*-Si and *p*-InP enhanced the rate of the hydrogen evolution reaction (HER) in terms of photocurrent density. In addition, these metals islets helped to lower the corresponding onset potential for HER on the metal decorated semiconductor electrodes. Based on these observations, surface modifications of the *n*-type semiconductors (photoanodes) with different metal islets are expected to lower the overpotential of the oxygen evolution reaction (OER) under illumination and thereby enhance the overall photoconversion efficiency for water splitting reaction.

In this study different metals (Ni, Pt, Co and Ru) were electrodeposited on the surface of CM-*n*-TiO₂ thin film electrodes. The effect of surface modification of these electrodes on OER was examined in term of photocurrent density in a basic electrolyte under solar simulated light illumination. The photo-catalytic activity and the surface morphology of these metal islets decorated CM-*n*-TiO₂ electrodes were characterized with potentiodynamic measurement and a scanning electron microscopy (SEM).

3.2.11 Surface morphology of CM-*n*-TiO₂ and metal islets decorated CM-*n*-TiO₂ thin films:

SEM pictures were taken before and after metal electrodeposition, Figure 3.24a and b show the surface morphology of CM-*n*-TiO₂ and Ru decorated CM-*n*-TiO₂ respectively. The bright spot (Fig. 3.24 b) clearly revealed the heavy metal (Ru) atoms as

evidence of Ru atoms randomly present on the surface of CM-*n*-TiO₂. Note that the CM-*n*-TiO₂ substrates were not chemically or electrochemically treated before the metal electrodeposition took place. SEM images confirmed the non-uniformity of the deposited metal islets and clusters on the surface of CM-*n*-TiO₂.

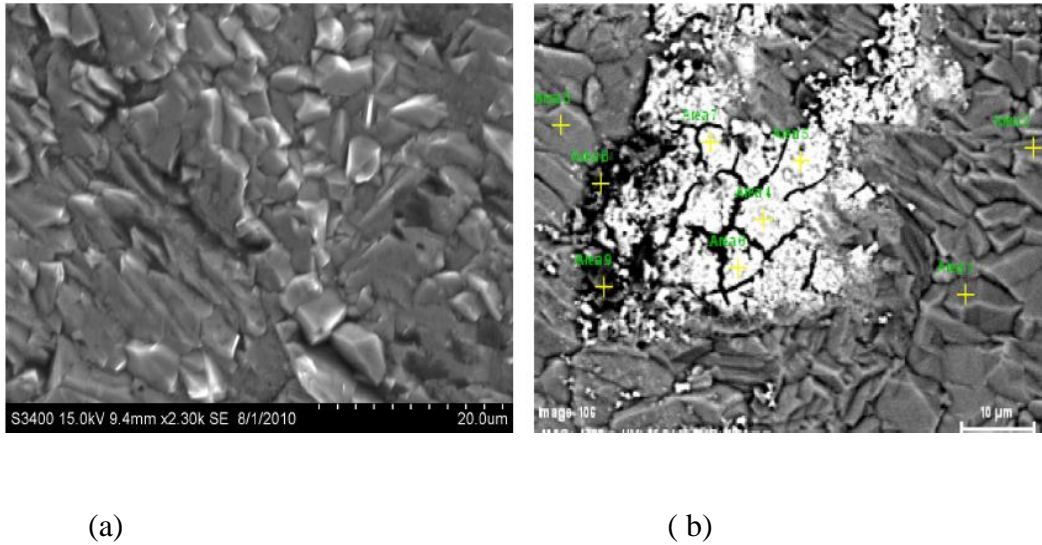


Figure 3.24 SEM picture for: a) CM-*n*-TiO₂ before metal islets electrodeposition
b) CM-*n*-TiO₂ after Ru islets electrodeposition (bright spots for the metal islets and clusters).

The reason for the metal was deposited on preferential spots of the substrate surface is not clearly known.¹¹⁴ However, the deposition of metal islets on these preferential spots could be due to the natural heterogeneity of the surface conductivity of the substrate (CM-*n*-TiO₂). At the same time, a uniform metallic thin layer on the surface of CM-*n*-TiO₂ is not desirable because such a uniform layer will block the incident light from reaching the underlying semiconductor.

3.2.12 Photoactivity of CM-*n*-TiO₂ and metal islets decorated CM-*n*-TiO₂ thin film electrodes:

In Figure 3.25 the dependence of the photocurrent density j_p , (mA cm^{-2}) as a function of measured potential (E_{meas} , V/SCE) were plotted for Ru metal islet decorated CM-*n*-TiO₂ and bare CM-*n*-TiO₂ electrodes under solar simulated light illumination (0.1 W cm^{-2}). The onset potential shift of 36 mV/SCE at a measured potential of - 0.78 V/SCE was observed for Ru metal islet decorated CM-*n*-TiO₂ compared to bare CM-*n*-TiO₂. A photocurrent enhancement (Δj_p) of 0.41 mA cm^{-2} was also observed at the same measured potential.

Table 3 summarizes the electrocatalytic effect of transition metal (Ni, Pt, Co and Ru) islets on CM-*n*-TiO₂ photoelectrodes for OER during water splitting. All data were taken at an applied potential, E_{app} , of 0.2 V/SCE where $E_{\text{app}} = |E_{\text{meas}} - E_{\text{aoc}}|$. E_{meas} is the measured potential and E_{aoc} is electrode potential measured under open circuit condition. It was observed that for CM-*n*-TiO₂ the Ru metal islets acted as the best electrocatalyst ($\Delta j_p = 0.41 \text{ mA cm}^{-2}$; $\Delta E = 36.0 \text{ mV}$) for OER compared to Ni or Co metal islets. Note that Pt and Ru islets have comparable electrocatalytic effect on CM-*n*-TiO₂.

It can be seen from Table 3 and Figure 3.25 that under the same operating conditions, (light intensity of 0.1 W cm^{-2} , 2.5 M KOH) the onset potential of the photocurrent was negatively shifted for metal islets decorated CM-*n*-TiO₂. As a result the negative shift lowered the overpotential for OER and increased the rate of oxygen generation in terms of photocurrent density as shown in Figure 3.25. At an applied potential of 0.2 V/SCE the overpotential shift (ΔE) was calculated to be - 0.042 V for Pt decorated CM-*n*-TiO₂. This overpotential shift corresponds to a lower free energy of

reaction, $\Delta(\Delta G)$, by 8.10 kJ mol^{-1} . This enhancement of photoresponse can be attributed to the increase of the electrocatalytic effect of transition metal islets towards OER compared to bare CM-*n*-TiO₂, as well as an increased field drop across the Schottky junction between the metal islets and the semiconducting CM-*n*-TiO₂. Notably the increased field drop at the semiconductor-metal islet interface helped to minimize the recombination of photo-generated electron hole pairs and consequently enhanced the rate of photoelectrochemical splitting of water.

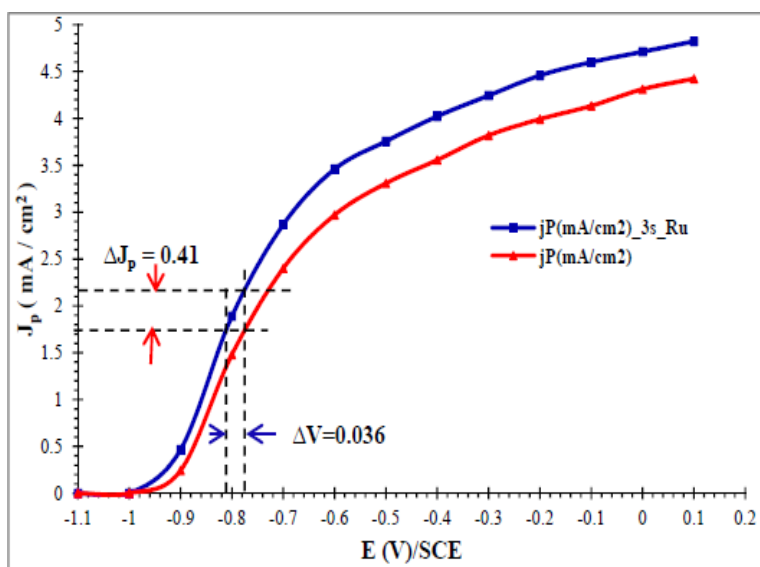


Figure 3.25 Photocurrent density (j_p , mA cm^{-2}) versus measured potential (V_{meas} , V/SCE) for:
 ◆ — Ru metal islet decorated CM-*n*-TiO₂
 ● - - Bare CM-*n*-TiO₂ electrodes. Note that the bare CM-*n*-TiO₂ samples are not highly optimized.

Table 3. The optimum electrodeposition time of metal islets in seconds, the electrode potential under open circuit condition; E_{aoc} , increase in photocurrent density, ΔJ_p ; and the lowering of onset potential, ΔE at an applied potential of 0.2 V.

Metal Islets	Electro-deposition time (second)	E_{aoc} (V)	E_{meas} (V)	ΔJ_p (mA cm ⁻²)	$-\Delta E$ (mV)
Ni	0	-0.923	-0.723	0.16	29
	5	-0.925	-0.725		
Pt	0	-0.861	-0.661	0.37	42
	2	-0.870	-0.670		
Co	0	-0.900	-0.700	0.19	20
	2	-0.910	-0.710		
Ru	0	-0.975	-0.775	0.41	36
	3	-0.980	-0.780		

3.2.13 Effect of surface morphology on the photoactivity of *n*-TiO₂ and

CM-*n*-TiO₂ thin film electrodes:

The effectiveness of a semiconductor catalyst in converting solar energy to hydrogen fuel relies on several factors such as surface morphology, light absorption and the recombination rate of the photogenerated charge carriers. It is well known that a high contact surface area between the catalyst and reactants is essential in order to increase the yield of a chemical reaction; hence, researchers in the field of photocatalysis have developed strategies to design several surface textures that are able to mitigate the photoconversion efficiency of these photocatalysts. The new surface textures include: porosity,^{117, 118} nanotubes,^{119, 120} nanowires¹²¹ and nanorodes.¹²² More importantly, in

semiconductor catalysts these nanostructured textures facilitate gas bubbles evolution¹⁰⁶,¹⁰⁷, enhance the incident light absorption due to light scattering within the porous surfaces and ensure an effective separation of the charge carriers (e^- and h^+) by shortening their diffusion length to reach the interface and the substrate, respectively.^{122, 123}

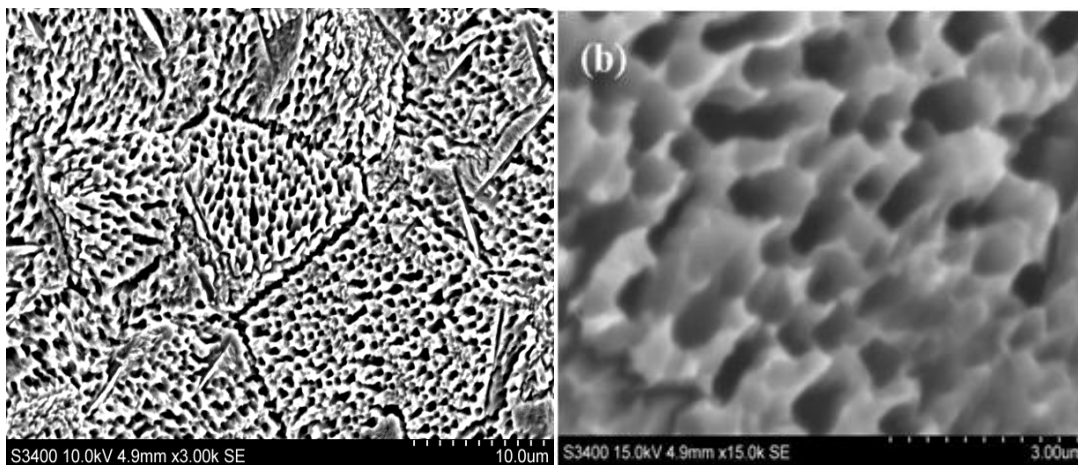


Figure 3.26. Top view SEM picture: (a) Ti metal sample (left) after hydrothermal treatment in 5% HCl solution at 180°C for 10 hours and (b) higher magnifications.

As seen in Figure 3.12, carbon modification of n -TiO₂ by thermal flame oxidation changes the morphology of the resulting thin film. In this study an etched Ti substrate was used instead of a flat Ti substrate. Figure 3.26 a and b show the etched Ti substrate obtained by hydrothermal treatment as reported in the experimental section 2.3. SEM images show a perfectly etched Ti substrate with sharp edges (Figure 3.26a); a closer look at the surface morphology of the etched Ti metal substrate reveals a honeycomb-like nanoporous layer with sharp edges (Figure 3.26b).

The thermal flame oxidation of etched Ti substrate was carried out as reported in section 2.2. The photocurrent density of the CM- n -TiO₂ thin film made by flame

oxidation of the etched Ti substrate unexpectedly decreased compared to CM-*n*-TiO₂ thin film made by flame oxidation of the flat Ti substrate as seen in Figure 3.27. To gain a deeper insight into the unexpected photocurrent decrease, the CM-*n*-TiO₂ thin films synthesized from the etched Ti sample were further investigated with SEM. The resultant SEM images revealed that the nanostructure of the Ti substrate had collapsed under the flame which resulted in a dramatic change of the initial surface morphology (Figure 3.28). The change of surface morphology led to the loss of the activity of these CM-*n*-TiO₂ thin films made from etched Ti substrates.

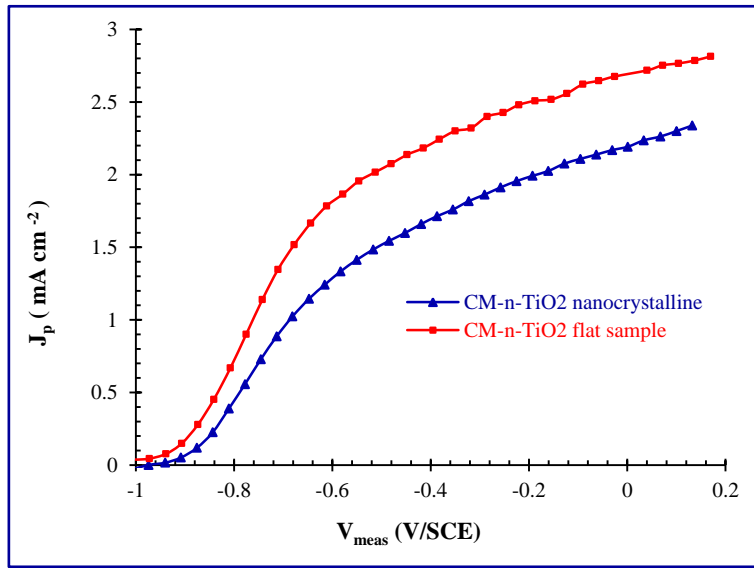


Figure 3.27. Photocurrent density as a function of measured potential, E_{meas} (V/SCE), for CM-*n*-TiO₂ thin film synthesized from a flat Ti sample and CM-*n*-TiO₂ thin film synthesized from an etched Ti sample. The photocurrent measurement was carried out under light intensity of 0.1 W cm⁻² from a global AM 1.5 solar simulators, and 2.5 M KOH electrolyte.

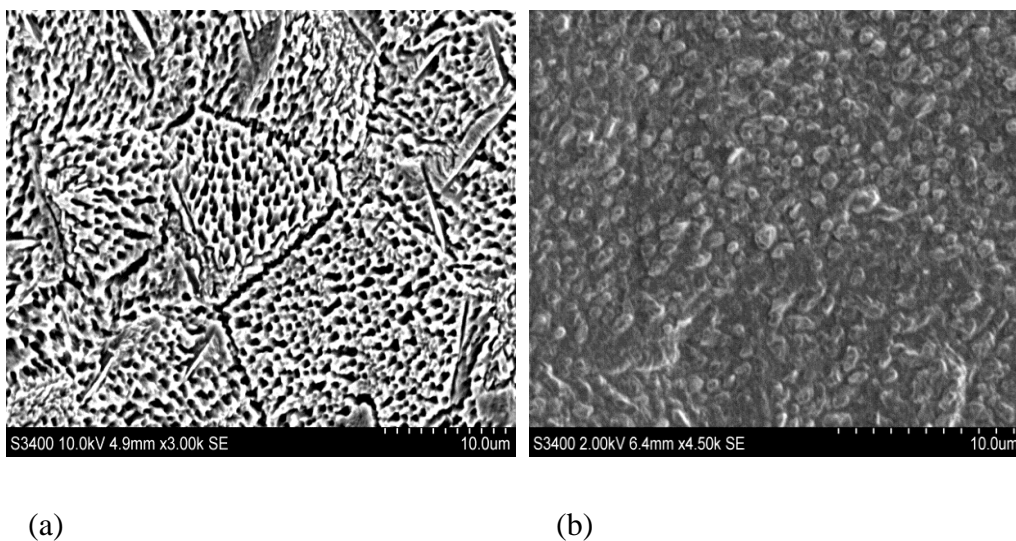


Figure 3. 28. Top view SEM picture (a) Ti metal sample (left) after hydrothermal treatment in 5% HCl solution at 180°C for 10 hours and (b) CM-*n*-TiO₂ thin film synthesized by thermal flame oxidation of the etched Ti metal sample at the optimum condition of flame temperature and time, 825°C and 15 min, respectively.

3.2.14 Summary:

CM-*n*-TiO₂ was successfully synthesized by controlled thermal flame oxidation of Ti metal substrate. Carbon doping of *n*-TiO₂ was found to slightly increase the photoresponse of *n*-TiO₂ in the visible region. However carbon doping increases significantly the photoactivity of *n*-TiO₂ in the UV region more importantly carbon doping changes the surface morphology of the semiconductor as confirmed by SEM investigations. Upon incorporation of carbon atoms within the semiconductor, the photocurrent conversion efficiency of *n*-TiO₂ was enhanced from 0.55% to 4.06% under an applied potential of 0.52 and 0.41 V/SCE respectively.

The surface modification of CM-*n*-TiO₂ with metal islets increased the photoactivity of the metal decorated photocatalyst. CM-*n*-TiO₂ synthesis by flame

oxidation of nanostructured Ti substrate was not successful due to the deterioration of the surface morphology of the substrate as seen by SEM investigation

3.3 Iron oxide nanowires and carbon modified (CM)*n*-Fe₂O₃ thin films for photoelectrochemical water splitting:

Iron oxide crystallizes in three main stable structures: Hematite (α -Fe₂O₃), Magnetite (Fe₃O₄) and Maghemite (γ -Fe₂O₃), it is noteworthy to mention that there are also several iron hydroxide crystalline structures.¹²⁴

Hematite is the most stable structure of iron oxide and is common in nature. It has a unique property in that the crystal morphology can be obtained under several shapes such as rods, spindles, cubes, stars, plates, and discs.^{125, 124} The versatile morphology of hematite makes it attractive in the synthesis iron oxide thin film electrodes with a desired surface morphology. As mentioned earlier in the introduction the semiconducting properties of iron oxide are applicable for the photoelectrochemical water splitting. Thereby, the radiationless fast recombination of the photogenerated charge carriers can be overcome by the use of a nano-structured iron oxide thin film electrodes.⁴⁸ The nanostructured surfaces provide an effective absorption of the incident light, as light scatters on porous surfaces, a high contact surface area at the interface electrode-electrolyte and facilitate gas bubbles evolution.

Nanostructures of hematite offer the possibility of overcoming some of the limitations of iron oxide via the control of the surface morphology. Carbon doping also can enhance the optical and electronic properties of iron oxide as we successfully used it to enhance the photoactivity of pristine *n*-TiO₂. In this study iron oxide nanowires and

carbon modified iron oxide thin film electrodes were synthesized and tested for water splitting under solar simulated light.

3.3.1 Surface morphology of $n\text{-Fe}_2\text{O}_3$ and CM- $n\text{-Fe}_2\text{O}_3$ thin films:

Iron oxide nanowires thin films were successfully synthesized in an electric tube furnace at the optimum conditions of 750°C and 15 min oxidation time in ambient atmosphere as reported earlier in the experimental section. The nanowires are vertically oriented as seen in Figure 3.29.

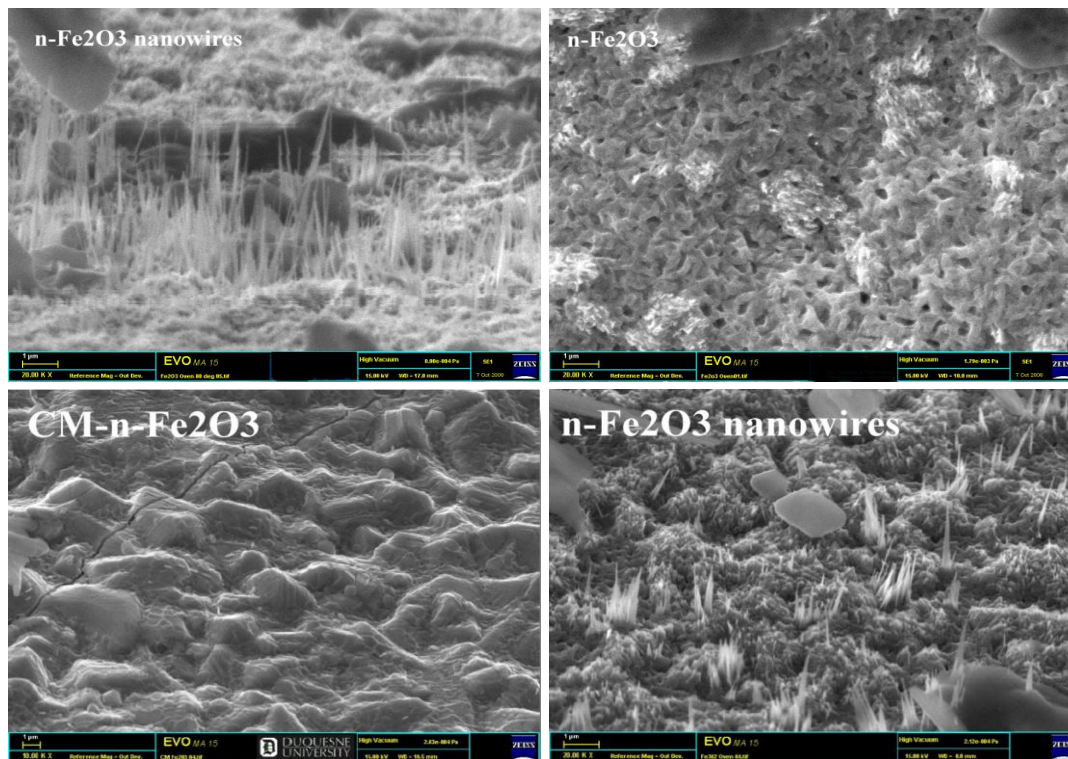


Figure 3.29. Top and side view SEM images for $n\text{-Fe}_2\text{O}_3$ nanowires. Top view SEM image of $n\text{-Fe}_2\text{O}_3$ flat sample, and flame oxidized CM- $n\text{-Fe}_2\text{O}_3$ thin film.

SEM pictures of CM- n -Fe₂O₃ thin films are also shown in figure 3.29. The images reveal a rough surface with cube like structures and no elongated structures such as wires or rods that were observed in n -Fe₂O₃. The absence of elongated structures in CM- n -Fe₂O₃ could be due to the fact that initial stretched structures that have been formed were eventually fused together because of the direct heat from the flame.

3.3.2 Photocurrent density of n -Fe₂O₃ nanowires and CM- n -Fe₂O₃ thin films under external bias:

The photoresponse of the nanostructured iron oxide electrodes was evaluated by measuring the rate of oxygen evolution in terms of photocurrent density, j_p (mA cm⁻²). The j_p can be calculated from the amount of oxygen evolved on the surface of the electrode according to faradays law (equation [17]).

The n -Fe₂O₃ nanowires electrode synthesized in the electric furnace exhibits a higher photocurrent density compared to the n -Fe₂O₃ flat sample as seen in Figure 3.30. The optimized iron oxide nanowires electrode generates a photocurrent density of 1.32 mA cm⁻² at a measured potential of 0.0 V/SCE (Fig. 3.30). The nanowires morphology helped to reduce the transport distance of the photogenerated minority carriers (holes, h⁺) from the bulk of the n -Fe₂O₃ nanowires to the electrode-electrolyte interface and consequently minimized the electron-hole pair recombination rate.^{126, 127} The nanowires structure also increased the effective surface area which is an essential property for a catalytic reaction and facilitates gas bubbles evolution compared to the flat surfaces where bubbles stick to the surface until a sudden burst occurs. Furthermore, the large surface area scatters the incident light in all directions and as a result a better absorption

of light occurs.^{104, 105} This helped to generate a higher photocurrent density compared to that of an early work on $n\text{-Fe}_2\text{O}_3$ flat surface synthesized by spray pyrolytic method.¹²⁸

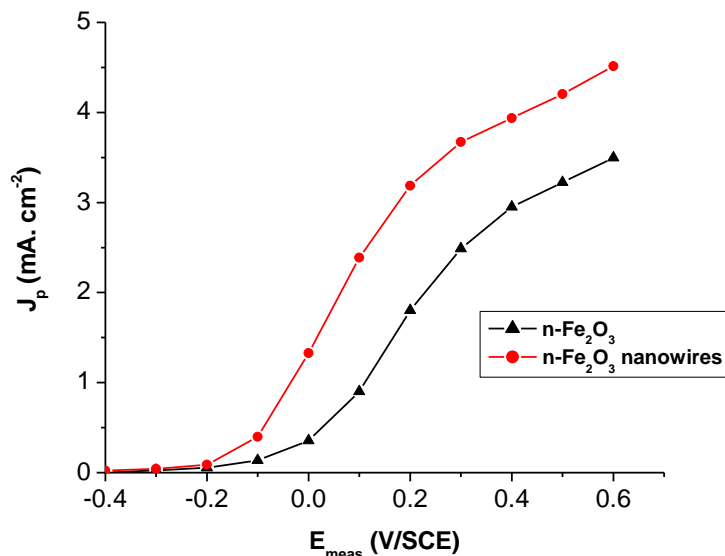


Figure 3.30. Photocurrent densities as a function of measured potential, E_{meas} (V/SCE), for $n\text{-Fe}_2\text{O}_3$ nanowires and $n\text{-Fe}_2\text{O}_3$ flat sample under light intensity of 0.1 W cm^{-2} from a global AM 1.5 solar simulator in 5 M KOH electrolyte.

The CM- $n\text{-Fe}_2\text{O}_3$ thin film synthesized at a flame temperature of $850 \pm 3^\circ\text{C}$ for 3 min oxidation time (optimum conditions) exhibited a higher photocurrent density than that of $n\text{-Fe}_2\text{O}_3$ nanowires for water splitting (Fig. 3.31) even though CM- $n\text{-Fe}_2\text{O}_3$ has no nanowires on its surface (Figure 3.29). At the same applied potential (0.0 V/SCE) the photocurrent density of CM- $n\text{-Fe}_2\text{O}_3$ thin film electrode improved more than two fold (3.14 mA cm^{-2}) compared to that of $n\text{-Fe}_2\text{O}_3$ nanowires (1.32 mA cm^{-2}) as seen in Figure 3.31. The photoactivity enhancement is mostly due to carbon incorporation on the surface or the lattice of the iron oxide thin film during flame oxidation. Carbon incorporation in CM- $n\text{-Fe}_2\text{O}_3$ is responsible for the higher photocurrent density generated during water splitting compared to earlier work on the Si-doped $n\text{-Fe}_2\text{O}_3$ thin films.⁵⁵

Furthermore, carbon doping of the semiconductor reduces the external applied potential to drive the water splitting reaction as seen in Figure 3.31 where oxygen evolution starts earlier, compared to the $n\text{-Fe}_2\text{O}_3$ nanowires thin film. These results indicate that carbon incorporation in Fe_2O_3 also increased its electrical conductivity and thus minimized the recombination of carriers prior to reaching the reactants at the interface. Note that low electrical conductivity is a major drawback in Fe_2O_3 samples.

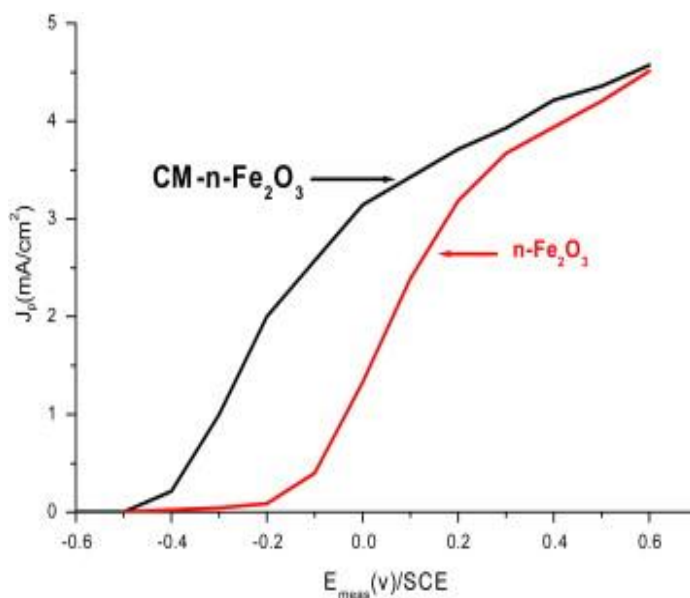


Figure 3.31. Photocurrent density as a function of measured potential, E_{meas} (V/SCE), for $n\text{-Fe}_2\text{O}_3$ nanowires and CM- $n\text{-Fe}_2\text{O}_3$ thin film electrodes under light intensity of 0.1 W cm^{-2} from a global AM 1.5 solar simulator in 5 M KOH electrolyte.¹²⁹

3.3.3 Photoconversion efficiency of $n\text{-Fe}_2\text{O}_3$ nanowires and CM- $n\text{-Fe}_2\text{O}_3$ thin films:

The percent photoconversion efficiencies, ε (%), of the photoelectrodes were calculated using equation [20]. Notice that the open circuit potential, E_{aoc} , of $n\text{-Fe}_2\text{O}_3$ nanowires and CM- $n\text{-Fe}_2\text{O}_3$ electrodes were found to be dependent on the wavelength dependent intensity of the incident light. Consequently ε (%) is calculated based on the

assumption of the contribution from the photopotential generated under light illumination. Therefore, the applied potential is different than the measured potential.

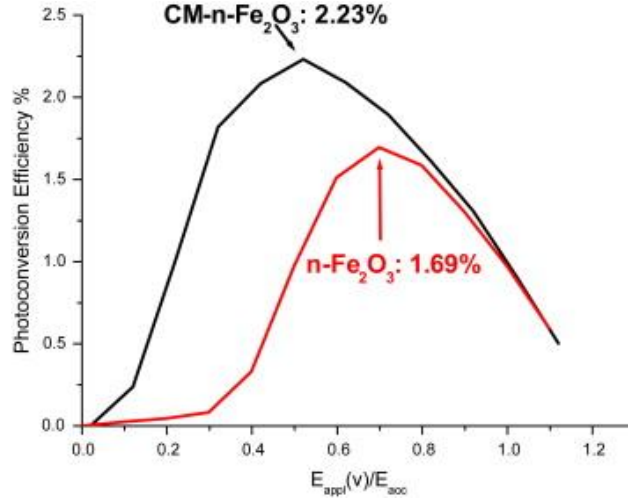


Figure 3.32. Photoconversion efficiency for $n\text{-Fe}_2\text{O}_3$ and $\text{CM-}n\text{-Fe}_2\text{O}_3$ as a function of applied potential E_{app} (V/ E_{aoc}) under light intensity of 0.1 W cm^{-2} from a global AM 1.5 solar simulator in 5 M KOH electrolyte.¹²⁹

As mentioned earlier in section 3.2.5 the other photoconversion efficiency expressions is not used here due to the fact that the dependence of the open circuit potential (E_{aoc}) on the incident light should not be ignored and needs to be taken into account.

Using Equation [20] the photoconversion efficiencies as a function of applied potential for $n\text{-Fe}_2\text{O}_3$ nanowire thin films and $\text{CM-}n\text{-Fe}_2\text{O}_3$ thin films were calculated (see Fig. 3.32). The maximum photoconversion efficiency of 1.69% at an applied potential of 0.7 V vs E_{aoc} and 2.23% at an applied potential of 0.5 V vs E_{aoc} were observed for $n\text{-Fe}_2\text{O}_3$ nanowires and $\text{CM-}n\text{-Fe}_2\text{O}_3$, respectively. From the plot of photoconversion efficiency- applied potential dependence, it is obvious that the overpotential for oxygen

evolution is lower on the surface of CM- n -Fe₂O₃ electrode compared to the pristine n -Fe₂O₃ nanowires.

3.3.4 Monochromatic photocurrent density of n -Fe₂O₃ nanowires and CM- n -Fe₂O₃ thin films:

The dependence of monochromatic photocurrent density, $j_p(\lambda)$, on the wavelength, λ (nm), of the incident light for both n -Fe₂O₃ nanowires and CM- n -Fe₂O₃ thin film electrodes having photoconversion efficiency of 1.69 and 2.23 %, respectively, are shown in Figure 3.33. The monochromatic photocurrent density, $j_p(\lambda)$, vs. wavelength, λ (nm), at a measured potential of 0.1 V/SCE under monochromatic light from a global AM 1.5 solar simulator exhibits a significant visible light absorption activity for both electrodes. The plot $j_p(\lambda)$ vs. λ (nm) illustrates that doping iron oxide (Fe₂O₃) using carbon can improve the photoactivity of the semiconductor particularly in the UV region between 225 and 450 nm.

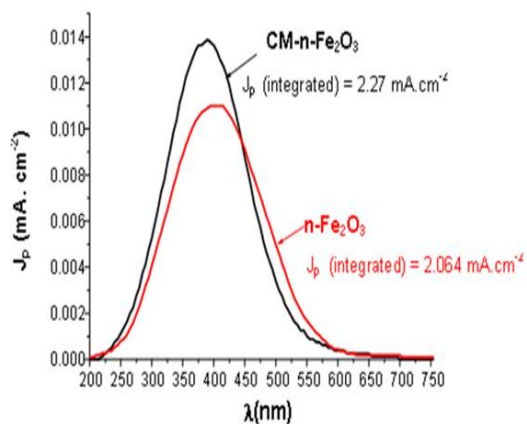


Figure 3.33. Monochromatic photocurrent density, $j_p(\lambda)$, as a function of wavelength of light, λ (nm), for n -Fe₂O₃ nanowires and CM- n -Fe₂O₃ thin film electrodes. The monochromatic photocurrent measurements were performed under light intensity of 0.1W cm⁻² from a global AM 1.5 solar simulator in 5 M KOH electrolyte.¹²⁹

3.3.5 Band gap energy of CM- n - Fe_2O_3 thin film:

Figure 3.34 shows Tauc plot of $(\eta h\nu)^{1/2}$ versus $(h\nu)$ for n - Fe_2O_3 nanowires and CM- n - Fe_2O_3 thin film electrodes. Note that η is the quantum efficiency calculated using equation [16]. An extrapolation of the linear regions of the plots, $(\eta h\nu)^{1/2}$ versus $(h\nu)$ for both electrodes, gives the band gap value as the intercept to the horizontal axis (where $(\eta h\nu)^{1/2} = 0$). From the extrapolation the band gap of CM- n - Fe_2O_3 was found to be about 2.2 eV, however the band gap for the n - Fe_2O_3 nanowires was found to be about 2.0 eV lower than that of CM- n - Fe_2O_3 . These values are within the range of the reported band gap values of CM- n - Fe_2O_3 (1.5 - 2.35 eV).^{130, 131, 132, 133}

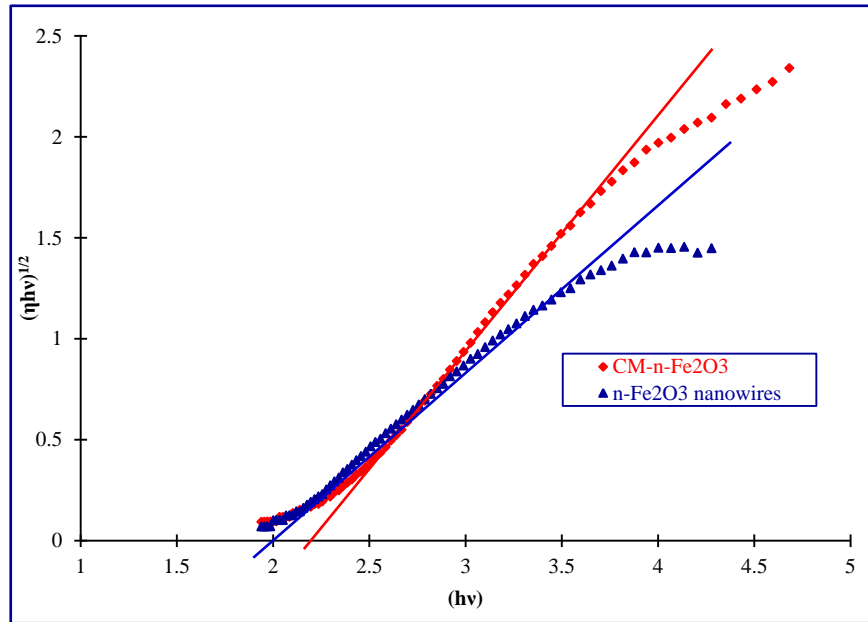


Figure 3.34 The respective plots of $(\eta h\nu)^{1/2}$ vs. $(h\nu)$ to determine the band gap of n - Fe_2O_3 nanowires and CM- n - Fe_2O_3 . The measurement were performed under a light intensity of 0.1 W cm^{-2} from a global AM 1.5 solar simulator in 5 M KOH electrolyte.

3.3.6 UV-Vis spectra of $n\text{-Fe}_2\text{O}_3$ nanowires and CM- $n\text{-Fe}_2\text{O}_3$ thin films:

The UV-Vis spectra for $n\text{-Fe}_2\text{O}_3$ and CM- $n\text{-Fe}_2\text{O}_3$ are presented in Figure 3.35. The samples have a clear absorption edge at around 600 nm, which conforms to the band gap of hematite (iron (III) oxide). The CM- $n\text{-Fe}_2\text{O}_3$ films showed an enhanced absorption in both UV and visible regions extending up to 680 nm.

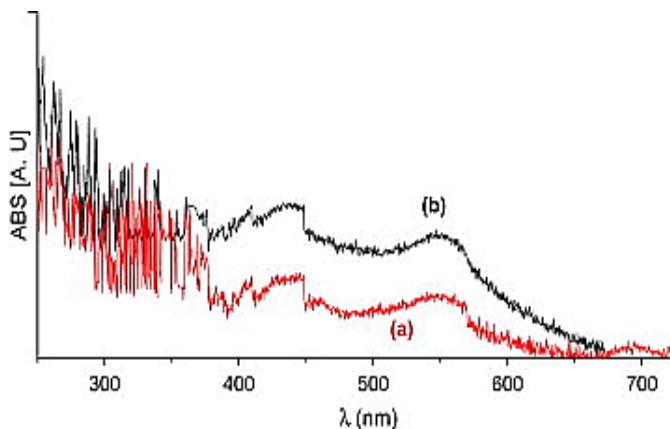


Figure 3.35. Diffuse reflectance spectra for $n\text{-Fe}_2\text{O}_3$ and CM- $n\text{-Fe}_2\text{O}_3$.¹²⁹

3.3.7 AC impedance spectroscopy: flat band potentials and doping densities of CM- $n\text{-Fe}_2\text{O}_3$ and $n\text{-Fe}_2\text{O}_3$ nanowires thin films:

The behavior of the thin film catalysts under AC frequencies was investigated with Electrochemical Impedance Spectroscopy (EIS). This study was conducted in order to evaluate the flat band potentials and the doping densities of CM- $n\text{-Fe}_2\text{O}_3$ and $n\text{-Fe}_2\text{O}_3$ nanowires. The data was recorded in the frequency range of 10 kHz to 5 mHz; an AC amplitude of 10 mV was used in all measurements; a Pt mesh electrode was used as the counter electrode and either the CM- $n\text{-Fe}_2\text{O}_3$ or $n\text{-Fe}_2\text{O}_3$ nanowires thin films were used as the working electrode.

Figure 3.36 shows the capacitance - potential characteristics in Mott-Schottky plot of the $n\text{-Fe}_2\text{O}_3$ nanowires and CM- $n\text{-Fe}_2\text{O}_3$ thin film electrodes at various AC

frequencies in 2.5 M KOH electrolyte solution in the dark. The capacitance, C , was calculated from the expression of impedance, Z , for a series of capacitor-resistor model as given in equation [30]. The squared inverse of capacitance C was plotted against the applied potential according to Mott-Schottky expression, (equation [31]).

In Figure 3.36, good fit of the straight line region of the Mott-Schottky plots were observed for the AC frequencies used for impedance measurement; however, for frequencies under 5 kHz the dispersion of the slopes of Mott-Schottky plots become highly pronounced. Thus we limited our study to AC frequencies equal to or higher than 5KHz. The positive slop indicates that the semiconductor is n -type. The intercept of the straight line of Mott-Schottky plot with the potential axis for n -Fe₂O₃ nanowires thin film was obtained between -0.38 and -0.41 V/SCE including the temperature dependent correction term, kT/e_0 ; whereas, an intercept between -0.43 and -0.49 V/SCE was observed for CM- n -Fe₂O₃. A negative shift of the flat band potential was observed in CM- n -Fe₂O₃ compared to n -Fe₂O₃ nanowires as seen in figure 3.30. This finding suggests that the flat band potential depends on the chemical modification of the semiconductor.

The doping density of the thin films was calculated from the slope of the straight line of the Mott-Schottky plot ($2/e_0\epsilon\epsilon_0N_d$) where $\epsilon = 80$ for intrinsic n -Fe₂O₃.¹³⁴ The average doping density of n -Fe₂O₃ at AC frequencies between 5 and 10 kHz was found to be $3.27 \times 10^{16} \text{ cm}^{-3}$ which is typical for a semiconductor electrode. However, this value was as expected higher for the carbon doped n -Fe₂O₃ which was found to be $4.14 \times 10^{16} \text{ cm}^{-3}$.

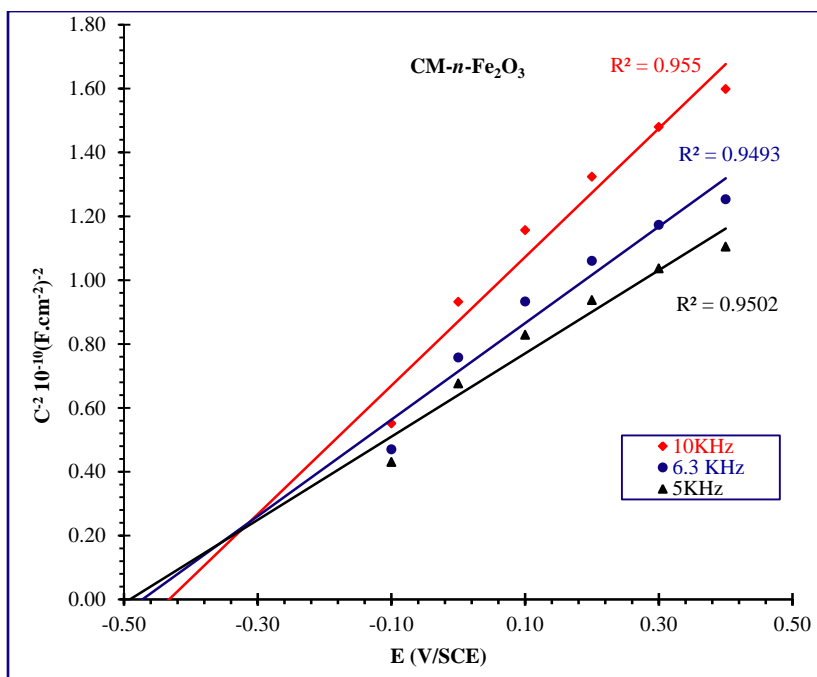
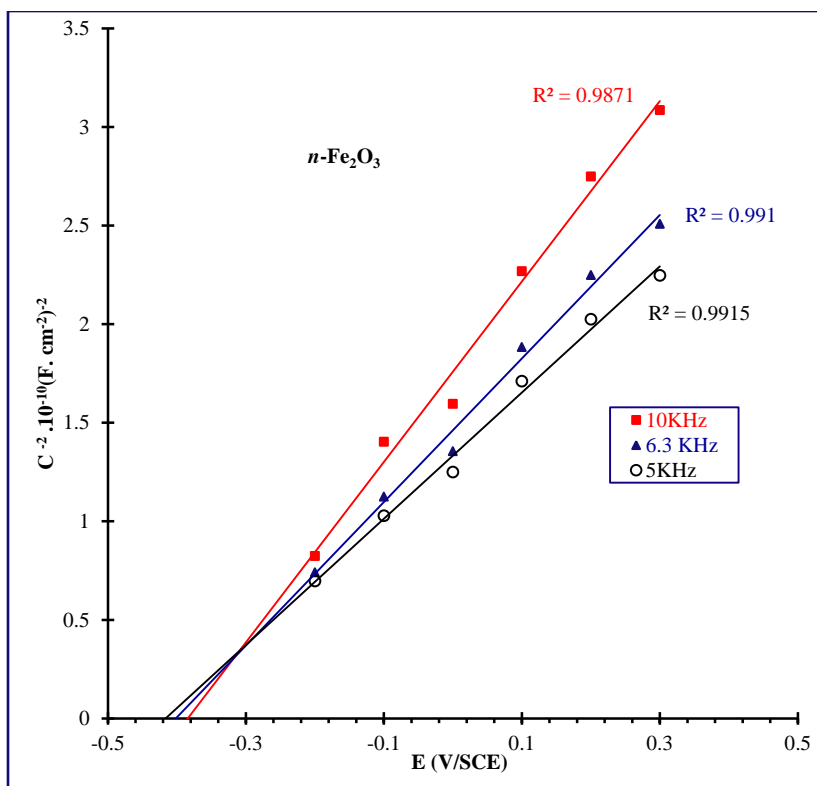


Figure 3.36 Mott-Schottky plot of *n*-Fe₂O₃ nanowires and CM-*n*-Fe₂O₃ thin films measured at various AC frequencies. 10 mV AC amplitude, 2.5 M KOH electrolyte measured in dark.

3.3.8 Elemental analysis for $n\text{-Fe}_2\text{O}_3$ nanowires and CM- $n\text{-Fe}_2\text{O}_3$ thin films using

EDS:

Figure 3.37 and Figure 3.38 show EDS spectra of the catalyst. The source of carbon in the CM- $n\text{-Fe}_2\text{O}_3$ sample is more likely to be from the combustion mixture of CH_4 and O_2 . Table 4 shows the elemental composition of CM- $n\text{-Fe}_2\text{O}_3$ and $n\text{-Fe}_2\text{O}_3$ where the amount of carbon is slightly higher in the flame made CM- $n\text{-Fe}_2\text{O}_3$ samples.

Table 4. EDS analysis and surface composition of $n\text{-TiO}_2$ and CM- $n\text{-TiO}_2$.

<i>Elements Atom %</i>	<i>Nanowires $n\text{-Fe}_2\text{O}_3$</i>	<i>Carbon modified CM-$n\text{-Fe}_2\text{O}_3$</i>
Fe	42.47	40.27
O	52.88	53.77
C	4.65	5.96

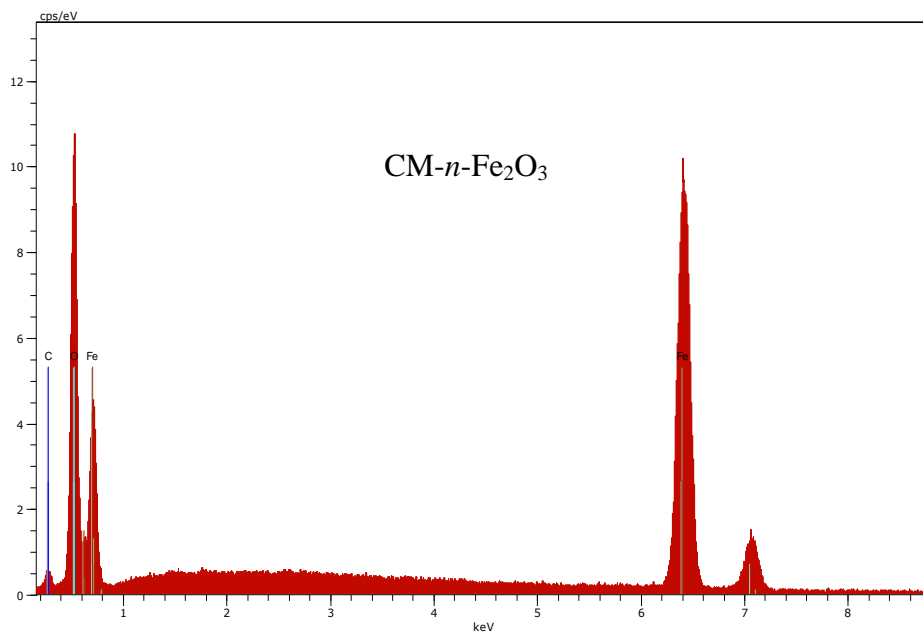


Figure 3.37. EDS spectra for CM- $n\text{-Fe}_2\text{O}_3$ thin films showing the surface elemental composition.

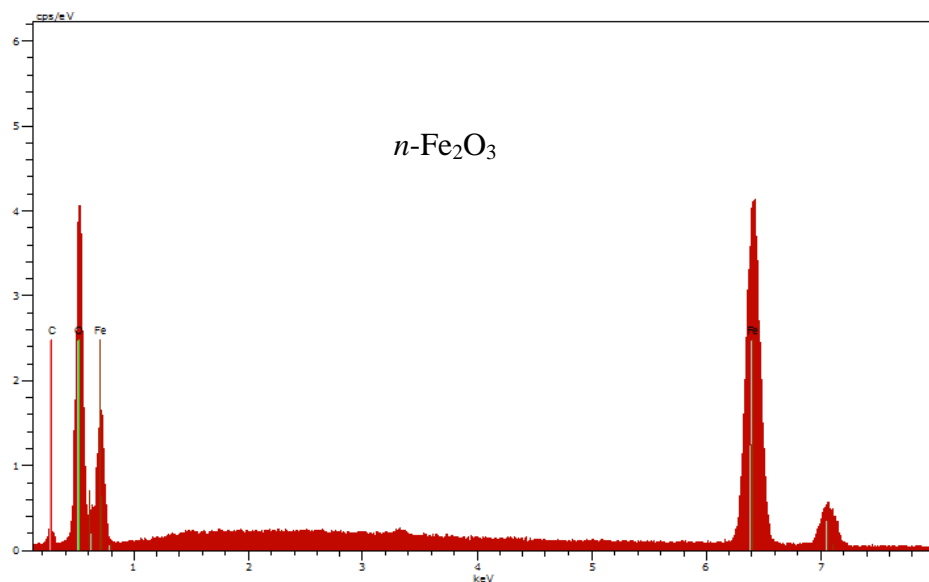


Figure 3.38. EDS spectra for $n\text{-Fe}_2\text{O}_3$ nanowires thin films showing the surface elemental composition.

3.3.9 X-ray Diffraction (XRD) patterns of $n\text{-Fe}_2\text{O}_3$ nanowires and CM- $n\text{-Fe}_2\text{O}_3$ thin films:

X-ray diffraction spectroscopy (XRD) was used to investigate the structure of $n\text{-Fe}_2\text{O}_3$ nanowires and flame oxidized CM- $n\text{-Fe}_2\text{O}_3$ thin films. Figure 3.39 shows strong XRD diffraction peaks which signify that the thin film of $n\text{-Fe}_2\text{O}_3$ nanowires and CM- $n\text{-Fe}_2\text{O}_3$ were highly crystalline and consisted mainly on Fe_2O_3 , Fe_3O_4 . This is consistent with the color of as synthesized thin films, which is black (Fe_2O_3) with red spots (Fe_3O_4) near the edges.

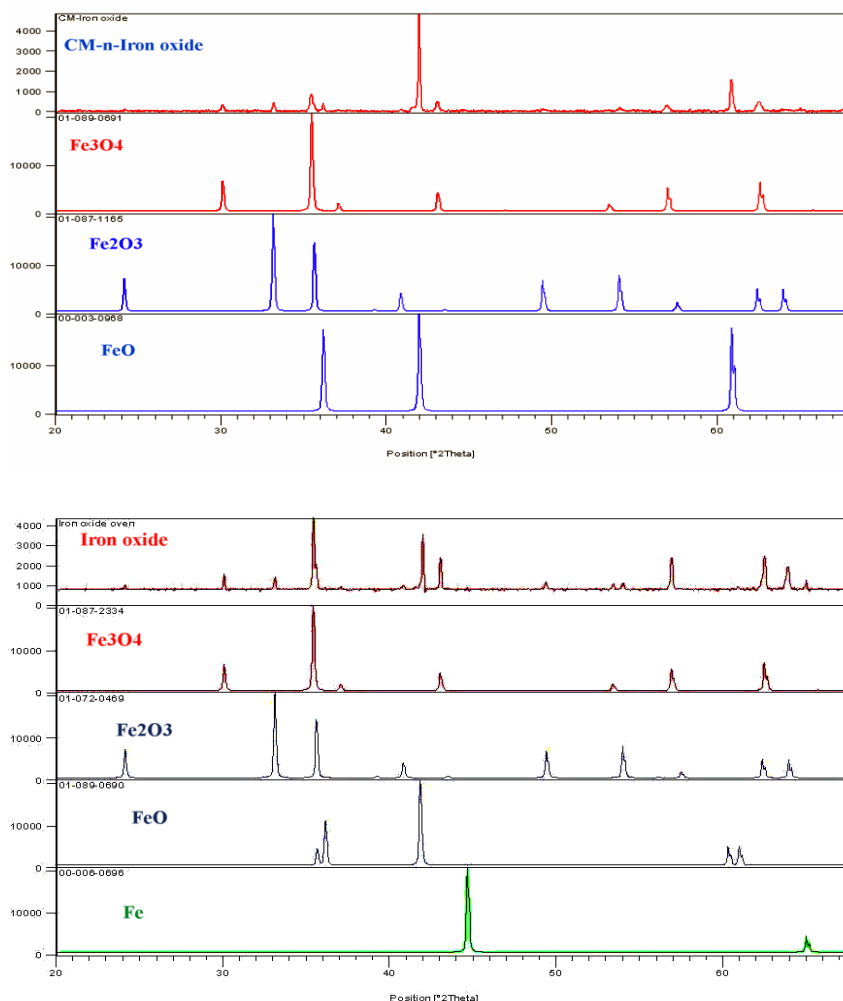


Figure 3.39 X-ray diffraction (XRD) patterns for iron oxide (nanowires) and carbon modified iron oxide (CM-*n*-Fe₂O₃) thin films compared to the reference patterns (jcpds cards) of Fe₂O₃(01-072-0469, 01-087-1165); Fe₃O₄ (01-089-0691, 01-087-2334); Fe (00-003-0968, 01-089-0690) and Fe (00-006-0669)

3.3.10 Summary:

The *n*-Fe₂O₃ nanowire films can be synthesized by oxidizing iron metal sheet in a tubular electric furnace and such films showed enhanced photoresponse for water splitting reaction compared to those made by spray pyrolysis or by silicon doping. Upon photoexcitation the minority carriers (holes) generated in the bulk of these nanowires travel a short distance to the semiconductor-electrolyte interface where they can react

with different species (OH^- , H_2O), thus minimizes the probability of recombination with majority charge carriers (electrons). Carbon modified iron (III) oxide ($\text{CM-n-Fe}_2\text{O}_3$) synthesized by flame oxidation of iron metal sheet generated much higher photoconversion efficiency compared to undoped $\text{n-Fe}_2\text{O}_3$ and also those made by spray pyrolysis or by silicon doping.

3.4 Monolithic water splitting and artificial photosynthesis:

Currently hydrogen generation from water electrolyzers is significantly more expensive than that produced from coal or natural gas. Therefore, coupling water electrolyzers with renewable power sources such as solar cell or wind turbine instead of electricity from a power plant is an ultimate solution that is capable of reducing the price of hydrogen generation by water electrolysis. Alternatively, the use of a monolithic water splitting systems would further lower costs associated with the separate construction and interconnection of photovoltaic (PV) systems and water electrolyzers.¹³⁵ This involves the emersion of the PV cell directly into the electrolyte solution. The new system resembles an artificial photosynthesis with a leaf-like design to split water to its elemental constituents of H_2 and O_2 where oxygen evolves on the positive side and hydrogen at the negative side of the PV system. Such a process is appealing with the use of semiconductors that generate enough electromotive force under sunlight illumination to drive the thermodynamically unfavorable water splitting reaction.

As mentioned earlier in section 1.2, amorphous silicon (a-Si) is an attractive candidate for this process. However, due to the instability of PV systems in electrolyte solution, a-Si cannot satisfy the stability criteria of a self-driven leaf-like PEC. In this

study triple junction amorphous silicon (Tj-a-Si) was selected as the semiconductor (PV system) to be covered with a visible light transparent TiO_2 thin film. The TiO_2 covered Tj-a-Si was further protected with a thin film of manganese oxide as shown in Figure 3.40.

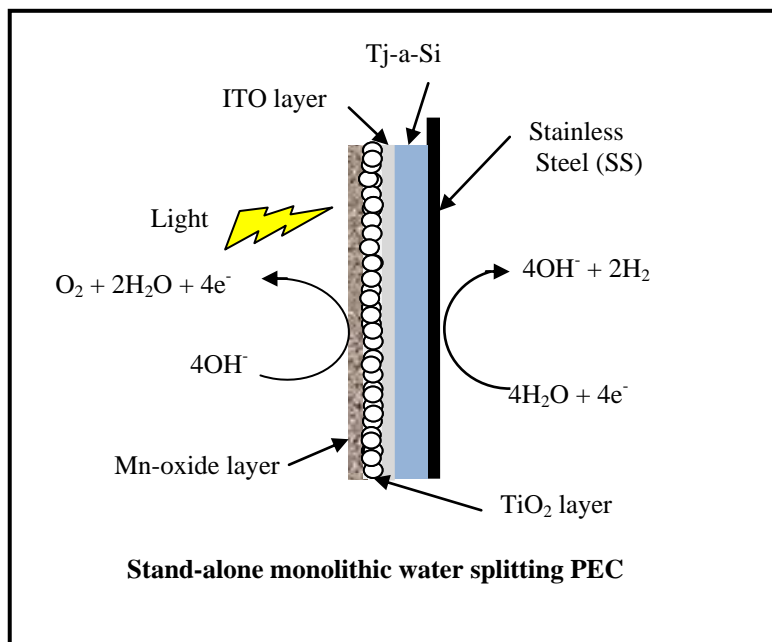


Figure 3.40 Schematic diagram of the monolithic leaf-like TiO_2 –Mn-oxide coated Tj-a-Si PEC. The diagram demonstrates the self-driven generation of oxygen on the light illuminated (1 sun) TiO_2 –Mn-oxide coated Tj-a-Si surface and hydrogen gas on the dark stainless steel (SS) surface during water splitting in 2.5 M KOH electrolyte.

3.4.1 Current-voltage (I-V) Curve for Tj-a-Si Solar Cell:

The current-voltage (I-V) plot (Fig. 3.42) of Tj-a-Si having a surface area of 0.82 cm^2 was obtained under solar simulated light intensity of 0.1 W cm^{-2} . The plot shows an open circuit voltage (V_{oc}) of 2.5 V, a short circuit current density, (j_{sc}) of 16.5 mA cm^{-2} and a maximum photovoltage (V_{max}) of 1.5 V at maximum power density (P_{max}) of 17.9

mW cm^{-2} . The V_{max} of 1.5 V supplied by the Tj-a-Si solar cell is sufficient to drive the water splitting reaction without the need of additional bias from an external power source.

The deposition of TiO_2 thin film on Tj-a-Si was carried out as reported in the experimental section 2.8.1 and yielded a thin film that contains coagulated particles of TiO_2 as shown in the SEM pictures (Fig. 3.41). It was stated in section 2.8.2 that a Mn-oxide layer will provide further protection for TiO_2 in electrolyte solution. We, therefore, deposited a thin layer of Mn-oxide on TiO_2 covered Tj-a-Si electrode.

The structure of the Mn-oxide layer was investigated by X-ray spectroscopy. It was reported earlier that curing $\text{Mn}(\text{OH})_2$ under vacuum resulted in the formation of Mn_2O_3 phase, only; this was confirmed by XPS analysis.⁶⁴ Whereas, our X-ray analysis of Mn-oxide, synthesized under the same experimental conditions, revealed the presence of two phases, Mn_2O_3 and Mn_3O_4 (Fig. 3.43).

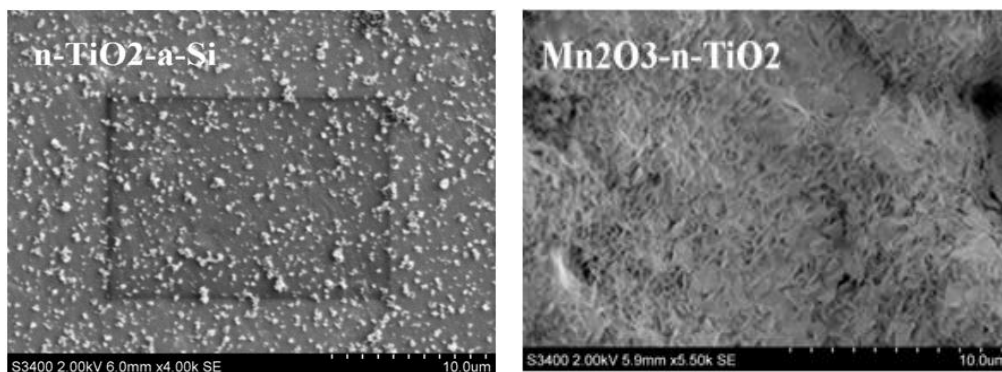


Figure 3.41 Top view SEM picture of TiO_2 coated Tj-a-Si and Mn-oxide- TiO_2 covered Tj-a-Si solar cell.

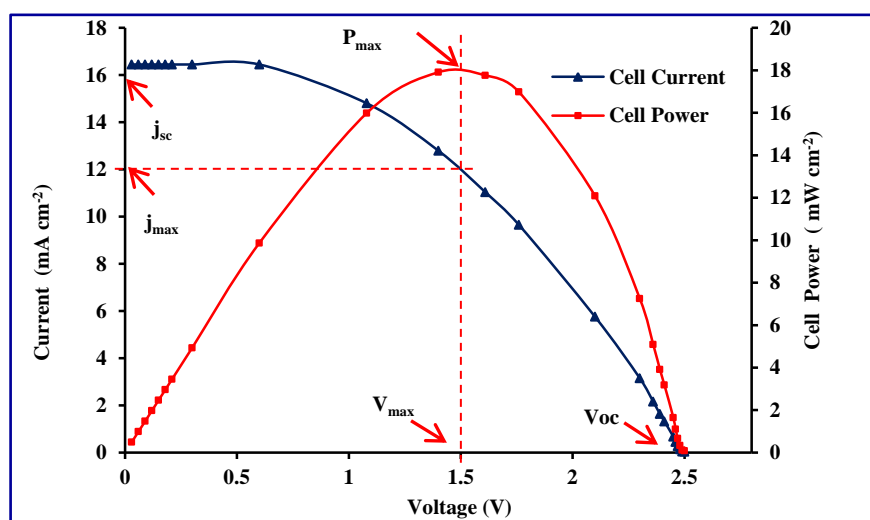


Figure 3.42 Plots of photocurrent density and cell power density versus photovoltage for Tj-a-Si solar cell to determine the maximum photovoltage (V_{\max}) at a maximum power.

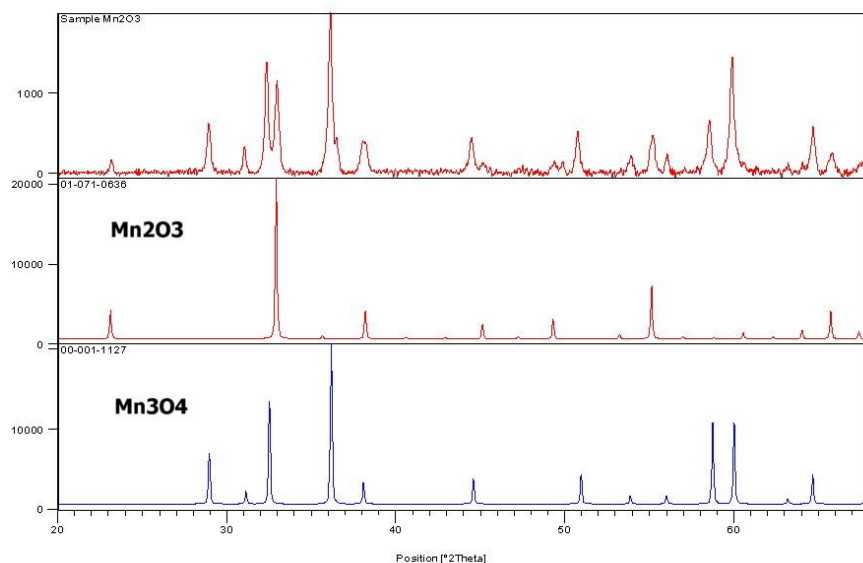


Figure 3.43 XRD powder patterns acquired from the as-prepared Mn-oxide film. Patterns for Mn_2O_3 are observed, see jcpds card 01-071-0636; patterns for Mn_3O_4 are also observed, see jcpds card 00-001-1127.

3.4.2 Volumes of H₂ gas collected using Mn-oxide-TiO₂ coated Tj-a-Si solar cell based PEC:

The volume of hydrogen collected using Mn-oxide-TiO₂ covered Tj-a-Si electrode as a function of time of exposure under solar simulated light is given in Figure 3.44. From the slope of the fitted straight line of the plot, the rate of H₂ evolution was obtained. The steady state H₂ generation rate was found to be 0.0207 mL cm⁻² min⁻¹ (12.4 L m⁻² h⁻¹). The moles of H₂ produced per second, $n_{H_2} = 1.37 \times 10^{-8}$ mol cm⁻² sec⁻¹, were calculated using the ideal gas law.

$$n_{H_2} = \frac{(P_{atm} - P_{water\ vap}) \times V_{H_2}}{RT} \quad (32)$$

With the assumption that hydrogen behaves as an ideal gas at atmospheric pressure, and considering the vapor pressure of water of the electrolyte solution to be equal to that of pure water, $P_{water\ vap} = 0.03126$ atm (23.76 mm H), at room temperature.

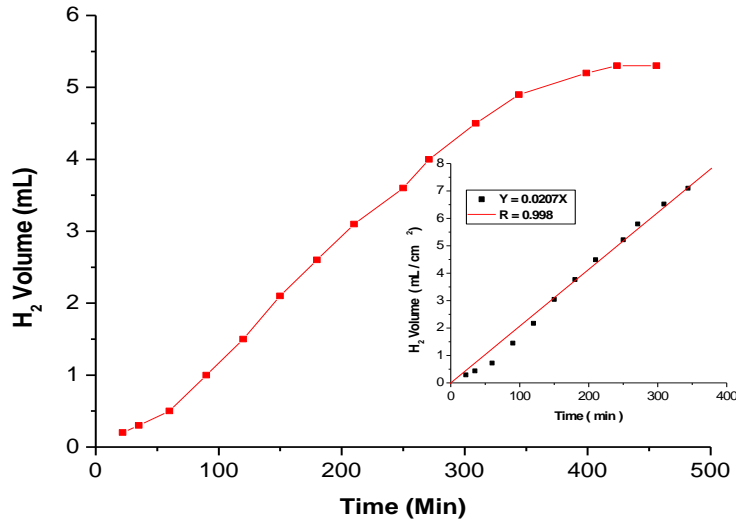


Figure 3.44 Volumes of Hydrogen gas (mL) collected versus time (min). In the inset a fitting line was drawn for the linear part of the plot of the volumes of H₂ evolved per cm² of photoactive Tj-a-Si surface of area 0.80 cm² versus time.

3.4.3 Solar to Hydrogen Efficiency, %STHE:

The percentage of solar to hydrogen efficiency, % STHE, was calculated directly from the number of moles of hydrogen, n_{H_2} , collected. The %STHE for H_2 generation was obtained from the following expression: ^{61, 27, 22}

$$STHE (\%) = \left[\frac{(j_p \times E_{rev}^0)}{P_{light}} \right] \times 100 \quad (33)$$

The photocurrent density, j_p , of hydrogen generation was calculated using Faraday's equation [17] and was found to be 2.64 mA cm^{-2} ; the standard reversible potential, $E_{rev}^0 = 1.23 \text{ V}$ for the overall water splitting reaction under standard conditions and light intensity of $P_{light} = 0.1 \text{ W cm}^{-2}$. The %STHE of 3.25 % was obtained and it is in agreement with %STHE calculated directly from the number of moles of H_2 collected, n_{H_2} using the equation, ¹³⁶

$$STHE(\%) = \left[\frac{(-\Delta G^0 \times n_{H_2})}{P_{light}} \right] \times 100 \quad (34)$$

with $\Delta G^0 = -237.13 \text{ kJ mole}^{-1}$ for the free energy of formation of $H_2O(l)$ from $H_2(g)$ and $O_2(g)$ under standard state condition, $n_{H_2} = 1.37 \times 10^{-8} \text{ mol}_{H_2} \text{ cm}^{-2} \text{ sec}^{-1}$ and $P_{light} = 0.1 \text{ W cm}^{-2}$.

The observed low solar to hydrogen efficiency could be attributed to the absorption and reflection of light by Mn-oxide- TiO_2 coating prior to reaching the underlying Tj-a-Si and therefore loss of light intensity. It should be also noted that the Tj-a-Si solar cell used in this study could generate a maximum photovoltage of 1.5 V only. Hence, a higher % STHEs could be achieved if more efficient a-Si that is capable of supplying a higher maximum photovoltage were used. High maximum photovoltage (>

2.0 V) and high photocurrent generating solar cells are needed to be used in a monolithic PEC for the self-driven photosplitting of water to hydrogen with high solar to hydrogen efficiency ($\geq 10.0\%$) that is required for future marketability.¹³⁷

Furthermore, the thin layer of Mn-oxide on TiO₂ covered Tj-a-Si surface acted as a protective layer, however, it is not an efficient electrocatalyst for the oxygen evolution reaction (OER). Thereby the protective layer should be both optically transparent as well as possesses high electrocatalytic activity towards OER. The added benefit of this design is the stability enhancement of a-Si based electrode by minimizing thermal damage of a-Si caused by heat producing infrared radiation that is absorbed by the aqueous solution in the monolithic PEC.

3.4.4 Stability of Mn-oxide-TiO₂ coated Tj-a-Si solar cell based PEC in the electrolyte solution:

Figure 3.44 indicates that the TiO₂-Mn-oxide coated Tj-a-Si solar cell based PEC sustained water splitting for 6 hours and started to decline in next half hour to no more hydrogen accumulation over the cathode. This result shows 70 times more stable compared to uncoated Tj-a Si solar cell, which lasted only for 5 minutes in 2.5 M KOH during water splitting reaction. Pinholes in Mn-oxide -TiO₂- film on Tj-a-Si may be the cause of the electrode degradation after 6 hours.

Some promising results were reported earlier^{61, 27, 65, 138, 139, 140} on monolithic PV based PEC for water splitting. It should be noted that some of these PV-PEC's are somewhat stable, but not cost effective or efficient enough, while others are efficient but not cost effective and stable enough in the electrolyte solution

3.4.5 Summary:

In this study Mn-oxide-TiO₂ coated Tj-a-Si was successfully used for monolithic self-driven water splitting to H₂ and O₂ having solar to hydrogen efficiency of 3.25 % under solar simulated light illumination of 1 sun. Higher solar to hydrogen efficiency could be achieved if a higher maximum photovoltage generating Tj-a-Si solar cell were used. The coating on Tj-a-Si by a corrosion resistant transparent layer of Mn-oxide-TiO₂ was essential to enhance the electrode stability from five minutes to six hours during water splitting reaction. Long-term stability can be achieved if a pinhole free transparent corrosion resistant layer could be deposited on Tj-a-Si solar cells. Experiments run at near neutral pH 6.5 could have enhanced the stability of Mn-oxide-TiO₂ coating on Tj-a-Si surface but photoconversion efficiency would be lower.

3.5 Water electrolysis:

3.5.1 Optimum power for water electrolysis:

The performance of solar or PV driven water electrolysis has not been yet reported in terms of optimum power from a PV cell that is required to sustain hydrogen generation overtime. In this study we report the optimum power and voltage required to be supplied either by a power supply or silicon solar cell for water electrolysis carried out in a single compartment electrochemical cell.

To investigate the effect of the applied potential on hydrogen generation during water splitting, different powers were applied to the electrochemical cell from a power supply while maintaining the same applied current [$power (W) = i (A) \times E (V)$]. Platinum (Pt) metal was chosen and used as electrode for OER and HER in 2.5 M KOH electrolyte

solution to eliminate other factors such as electrode degradation. Hydrogen gas was collected over the Pt cathode as was explained in the experimental section 2.8.3 and the corresponding hydrogen current was calculated from the number of moles of hydrogen gas collected according to equations [17] and [32].

It was observed in Figure 3.45 that hydrogen current was considerably less than the current supplied from the power supply when the applied potential was below the optimum value of 3.5 V. These results demonstrate that hydrogen current cannot be sustained closer to the current supplied if the applied voltage was not optimum (3.5 V).

To determine the dependence of hydrogen generation rate on the applied potential, hydrogen currents were measured by varying the applied potential while maintaining similar powers (see Fig. 3.46). It was observed that though the values of total power supplied were almost similar, the hydrogen current was not sustained closer to the supplied current when the voltage applied was lower ($V = 3.0$ volt) than the optimum value, e.g., 3.5 V. Furthermore, hydrogen currents were measured at two different applied potentials (e.g., 3.5 V and 4.0 V) as a function of time (see Figure 3.47). It was observed in both cases that the hydrogen currents were found to be closer to the current supplied from the power supply. Hence, a high applied potential equal or above the optimum value of 3.5 V is essential to sustain a hydrogen current closer to the externally supplied current. One needs high potential to overcome the extra resistance developed at the electrode surface during gas evolution.

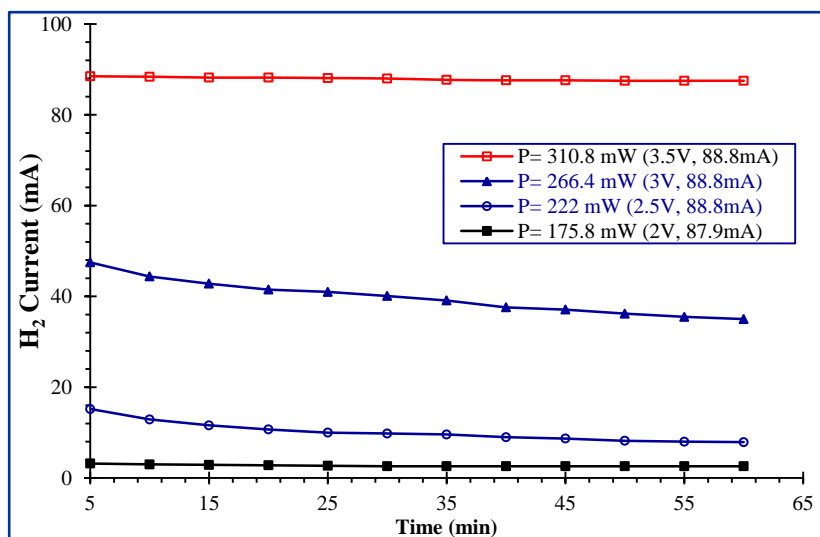


Figure 3.45 Hydrogen current vs time plots for different powers (P) supplied to electrochemical cell from the power supply (the areas of the Pt anode and Pt cathode were 0.69 cm^2 and 4.25 cm^2 respectively).

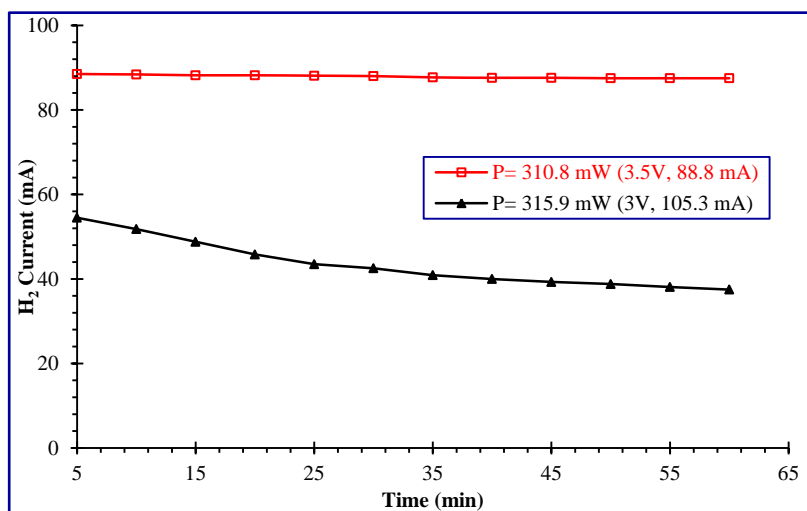


Figure 3.46 The effect of the applied voltage on hydrogen current at similar powers but different voltages from the power supply (the areas of the Pt anode and Pt cathode were 0.69 cm^2 and 4.25 cm^2 respectively).

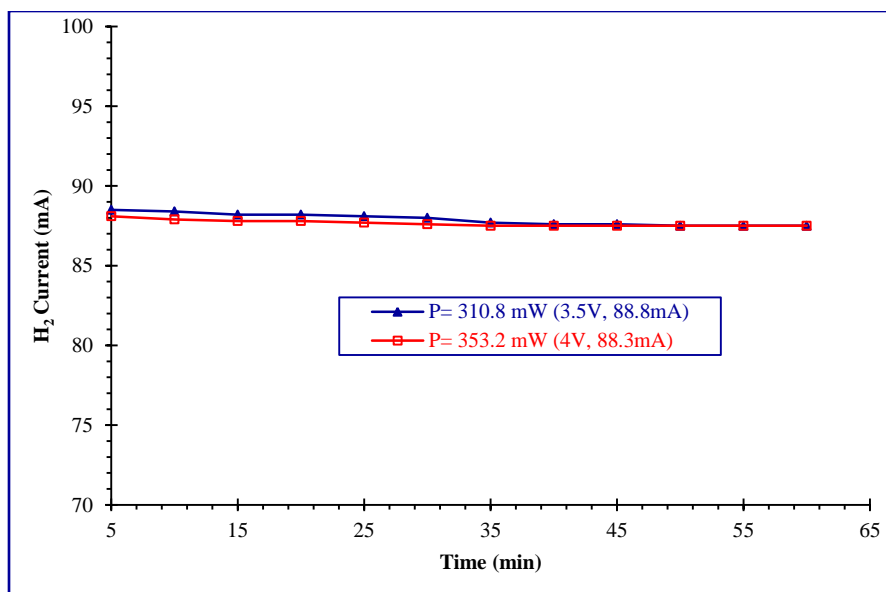


Figure 3.47 The effect of high voltages from a Power Supply on hydrogen currents (the areas of the Pt anode and Pt cathode were 0.69 cm^2 and 4.25 cm^2 respectively).

The effect of the applied power from solar cells on hydrogen current was investigated with the use of different solar cells generating different powers. Hence, different powers were applied from these solar cells to carry out water electrolysis. The observed hydrogen currents were plotted as a function of time as shown in Figure 3.48. It was observed that hydrogen current was found to be closer to the current supplied from solar cell 1 having a maximum photovoltage of $V_{\max} = 3.8 \text{ V}$ and a maximum power $P_{\max} = 22.5 \text{ mW cm}^{-2}$ (see Fig. 3.48 and Fig. 3.49). However, much lower hydrogen current was observed when solar cell 2 with $V_{\max} = 1.5 \text{ V}$ and $P_{\max} = 20.5 \text{ mW cm}^{-2}$ was used during water electrolysis despite that solar cell 2 supplied the highest photocurrent compared to solar cell 1 and solar cell 2 (fig. 3.48 and Fig. 3.49).

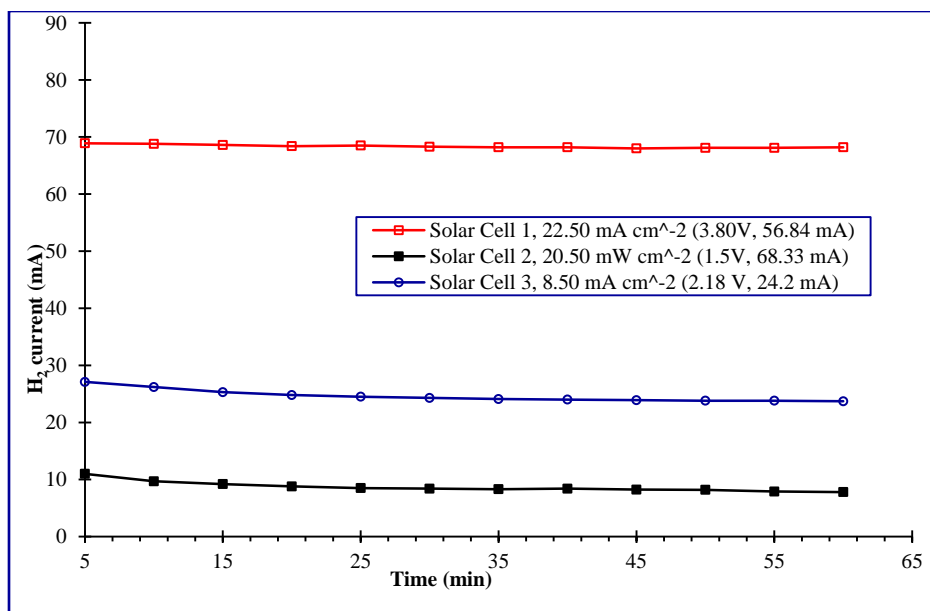


Figure 3.48 Hydrogen current density vs time plots for power supplied from solar cell 1, 2, and 3 under solar simulated light intensity of 0.1 mW cm^{-2} (the areas of the Pt anode and Pt cathode were 0.69 cm^2 and 4.25 cm^2 respectively).

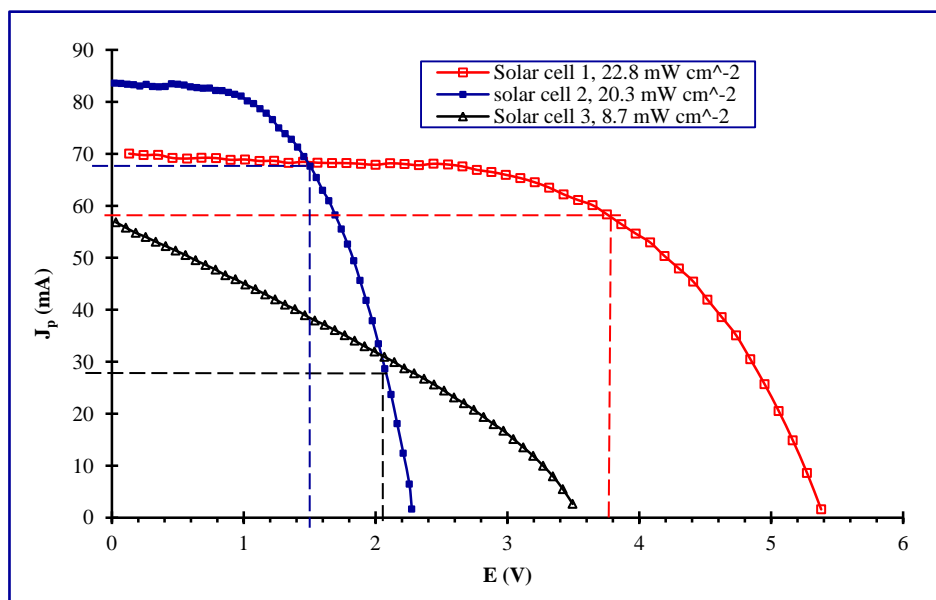


Figure 3.49 I-V curves for the three solar cells used to power the electrochemical cell during water splitting. The photoactive areas of solar cell 1, 2 and 3 used were 9.6 cm^2 , 5.0 cm^2 and 6.2 cm^2 respectively.

In conclusion it should be pointed out that it is essential to have an optimum voltage (e.g. ≥ 3.5 V) to generate high hydrogen rate during water electrolysis despite having a high current supplied either from power supply or from solar cells. This finding is essential to design a state of the art PV cells with optimum power requirements for solar driven water electrolysis.

3.5.2 Earth abundant electrocatalyst for oxygen evolution reaction (OER):

3.5.2.1 Development of earth abundant and high performance porous catalyst for oxygen generation for solar driven water electrolysis:

In order to produce inexpensive hydrogen generated by solar driven water electrolysis, it is essential to develop cost effective and efficient electrocatalysts. The approach is aimed at developing a suitable combination of materials to produce highly porous catalytic anodes for oxygen generation with low over-potentials to minimize the energy losses and achieve high electrolysis efficiency. For this project a highly porous anodes, Ni-Co₃O₄, were synthesized as given in the experimental section 2.9.

The porosity of Ni-Co₃O₄ was studied using fluid pore filling method (experimental section 2.9) and the void ratio was calculated according to equation [15] where the average void ratio is shown in table 5. These porous Ni-Co₃O₄ electrodes produced high void volume with an average void percent of 68.4%; furthermore, SEM image in figure 3.50 clearly shows the porous structure of these electrodes.

Electrochemical performance of the porous anode was assessed in terms of hydrogen current generation rate (mA cm⁻²) and percent solar to hydrogen efficiency during solar driven water electrolysis. The PV cell used for this study consists of two

double junction amorphous silicon (Dj-a-Si) solar cells connected in series having total surface area of 1.82 cm^2 . Each Dj-a-Si cell could deliver a maximum photovoltage, $V_{\text{max}} = 1.5 \text{ V}$, and a maximum current density, J_{max} of 12.1 mA cm^{-2} at maximum power, P_{max} , under solar simulated light with intensity of 1 sun (0.1 W cm^{-2}) as shown in Figure 3.51.

The % STHE was calculated using the expression in equation [33]. Note that in multicell electrolyzer the total solar to hydrogen conversion efficiency is expressed as,

141, 142, 143

$$\%STHE = PV \text{ efficiency} \times \text{Electrolyzer efficiency} \quad (35)$$

where the PV and electrolyzer efficiencies are provided by the equipments manufacturers.

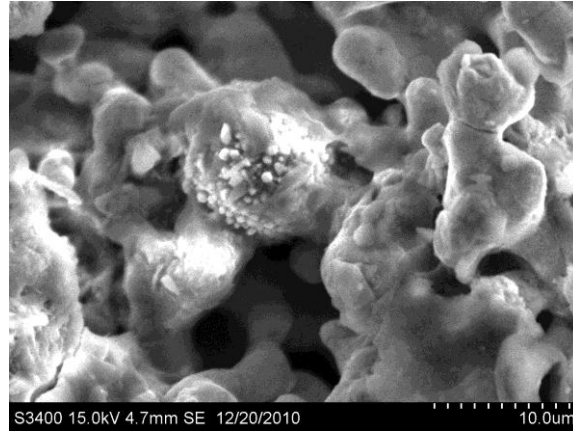


Figure 3.50 Top view SEM image of porous Ni-Co₃O₄.

Other efficiencies similar to equation [33] were also reported, where the thermo-neutral voltage of 1.48 V which corresponds to $\Delta G = 39 \text{ W h g}^{-1}$ was used.^{1, 144} In this study we used standard potential for water splitting reaction, 1.23V or $\Delta G = 237.2 \text{ kJ}$

mol⁻¹, instead of the thermo-neutral potential which is considered as an overestimation at room temperature.¹⁴⁵

Table 5. Void calculation for nickel-cobalt oxide porous anodes

Void Volume cc	Bulk Volume cc	Void Ratio	Void %
1.6	2.4	0.72	72

The results of hydrogen current generation and the % STHE in the solar driven electrochemical cell calculated according to equations [17] and [33], respectively are shown in Table 6. The higher amount of hydrogen gas was collected with the use of Ni-Co₃O₄ anode compared to RuO₂-Ti. Although Co-oxides and Ni are known to have lower catalytic activity¹⁴⁶ toward OER compared to RuO₂; the observed higher hydrogen current efficiency is possibly due to the high surface area of the porous anode Ni-Co₃O₄ compared to the flat RuO₂-Ti.

Table 6. Hydrogen current, and % STHE for Ni-Co₃O₄ compared to RuO₂-Ti anode in a Dj-a-Si solar cell driven water electrolysis under solar simulated light of 0.1 W cm⁻².

Cell electrodes	H ₂ Current (mA cm ⁻²)	STHE%
Ni-Co ₃ O ₄ Pt	12.84	8.66
Ti/RuO ₂ Pt	12.55	8.46

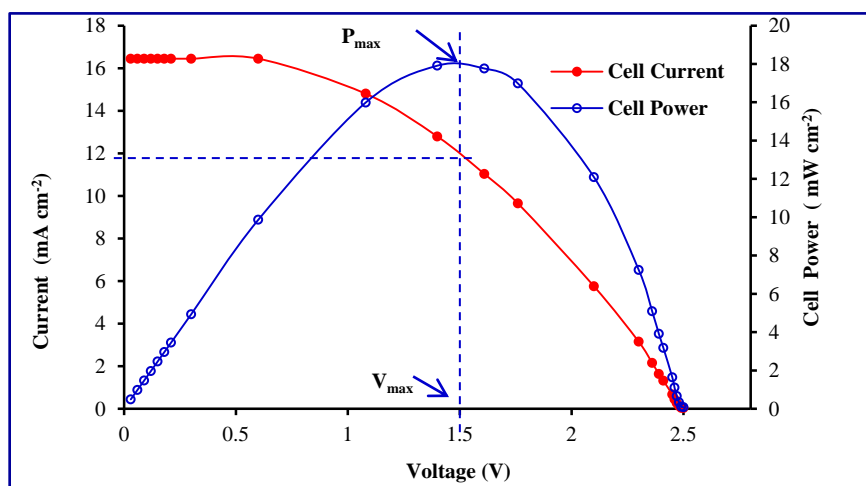


Figure 3.51 Current density, J (mA cm^{-2}) versus cell voltage (Volt) and cell power density, P (mW cm^{-2}) for the Dj-a-Si solar cell under solar simulated light intensity of 0.1 W cm^{-2}

3.5.2.2 Catalytic activity of Ni-Co-mixed oxide toward OER under an external bias:

Ni-Co mixed oxide thin film electrodes were tested for their activity toward oxygen evolution to determine the optimum composition or Ni/Co ratios. These mixed oxide thin film electrodes were synthesized as described in experimental section 2.10. Polarization data was taken at 50 mV/s between 0.2 and 0.8 V vs SCE and is shown in figure 3.52. Ni-Co mixed oxide thin film electrode with the ratio, Ni/Co = 3, was found to generate the highest current of the electrocatalysts examined during water electrolysis. Ni-Co mixed oxide with the optimum ratio was further investigated for water electrolysis and compared to Co-oxide and bare ITO. Figure 3.53 shows the polarization data at 50 mV/s between 0 and 1.6 V vs SCE for Ni-Co mixed oxides, Co oxide and ITO during water electrolysis. Ni-Co mixed oxide catalyst shows the highest catalytic activity for OER compared to Co-oxide. The observed sharp rise in current density at Ni-Co mixed oxide at 0.5 V/SCE indicates a possible interaction between Ni and Co oxides that played

an important role in generating active low overpotential surface sites for OER. For example, at 1.0 V/SCE the current density of 83.50 mA cm^{-2} was observed at Ni-Co-oxide, which is almost 3-fold higher compared to observed current density of 30.0 mA cm^{-2} at Co-oxide under the same applied external bias.

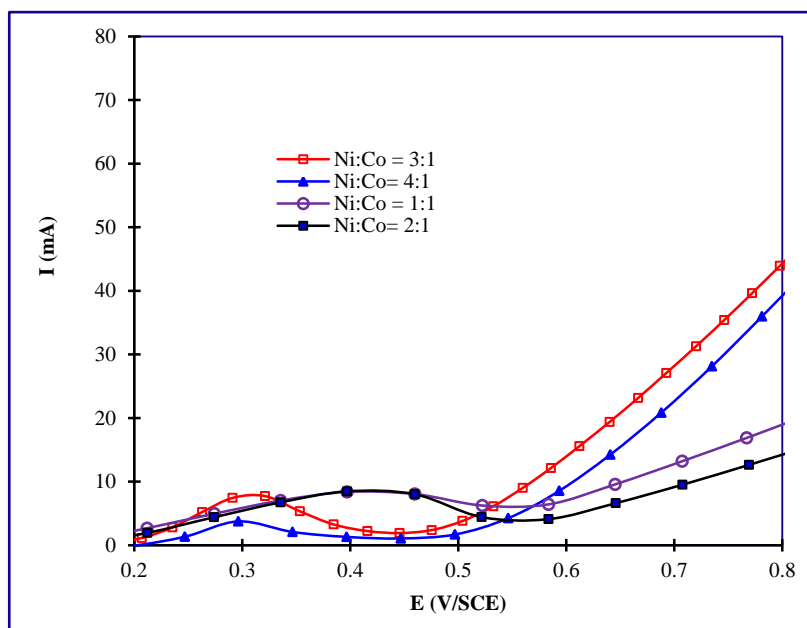


Figure 3.52 Current density, $J \text{ (mA cm}^{-2}\text{)}$ versus applied potential ($E \text{, V/SCE}$) for oxygen evolution reaction (OER) during water splitting in 2.5 M KOH electrolyte solution showing the highest activity for Ni-Co₂O₃ mixed oxide with a ratio of Ni/Co = 3.

The observed peaks prior to oxygen evolution in Figure 3.52, 3.53 and 3.54 is a pinpointing to the formation of an oxide before oxygen evolution starts. The voltametric behavior of Co and Ni oxides in alkaline medium can be complex due to the involvement of different types of oxide species and their relevant allotropic phases in the electrochemical process at the electrode surface. In alkaline medium and under positive polarization species that may be involved in the electrochemical process are M(OH)_2 ,

MO, M₂O₃, M₃O₄, MO₂ (where M = Co, Ni).^{147, 148} According to the voltamogram in figure 3.54 the peak prior to oxygen evolution for Ni-Co mixed oxides with the optimum composition is most likely due to the cobalt oxide species. These observations also show the existence of a correlation between the position of the oxidation peak and an early oxygen evolution. This finding supports an early attempt to find a useful descriptor or guidelines for an efficient metal oxide based oxygen evolving catalyst.⁷⁵ To date numerous studies have been carried out on transition metal oxide based catalysts for OER. Although the catalytic activity of these oxides has been improving, prior studies failed to provide an insight on the active sites and a simple mechanism for OER.

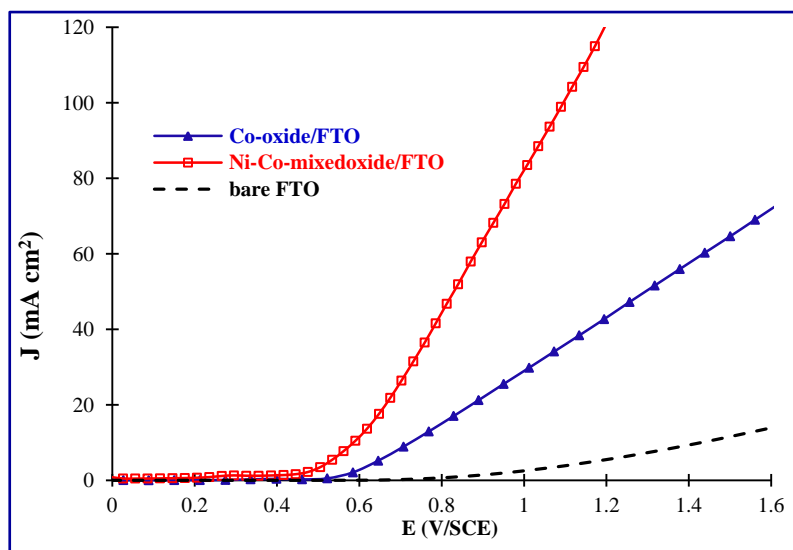


Figure 3.53 Current density, J (mA cm⁻²) versus applied potential (E , V/SCE) for oxygen evolution reaction (OER) during water splitting in 2.5 M KOH electrolyte solution showing the highest activity for Ni-Co-mixed oxides compared to Co-oxide and bare FTO coated conducting glass.

Figure 3.55 shows the Tafel plots for Ni-Co mixed oxide and Co oxide thin film electrodes. Ni-Co mixed oxide has the lowest Tafel slope of 160 mV/decade compared to 233 mV/decade for Co-oxide anodes during oxygen evolution. The lowest Tafel slope

for mixed Ni-Co oxide indicated a high electrocatalytic activity due to synergetic effect^{149, 150} of two oxides that generated active surface sites for efficient OER.

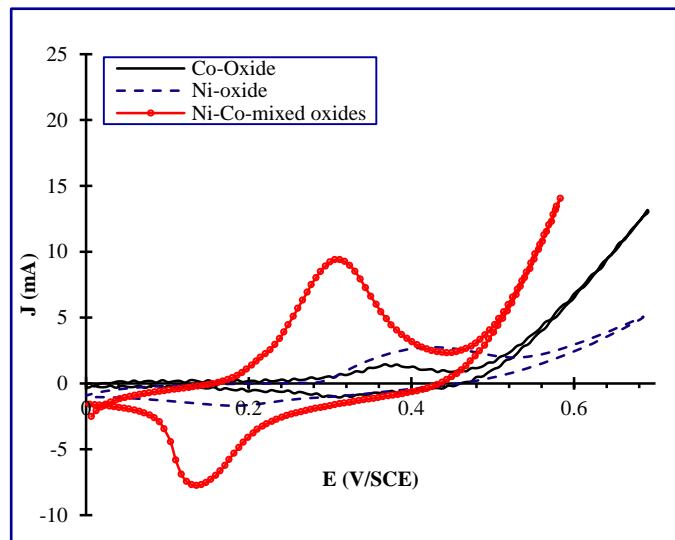


Figure 3.54 Cyclic voltammetry plots for Ni-Co-mixed oxide with optimum composition, Co-oxide, Ni-oxide deposited on FTO coated glass substrate in 2.5 M KOH electrolyte.

Surface morphological observations were obtained using scanning electron microscopy (SEM). The micrograph in Figure 3.56 (C) shows the morphology of Ni-Co mixed oxides thin film with a homogenous coating compared to a porous surface of Co-oxide, Fig. 3.56(B), and less porous surface of Ni oxide, Fig. 3.56 (B). A homogenous coating may result in better adherence to the underlying ITO substrate and thus better current collection. However, cracks are still visible on the surface of Ni-Co mixed oxides thin film.

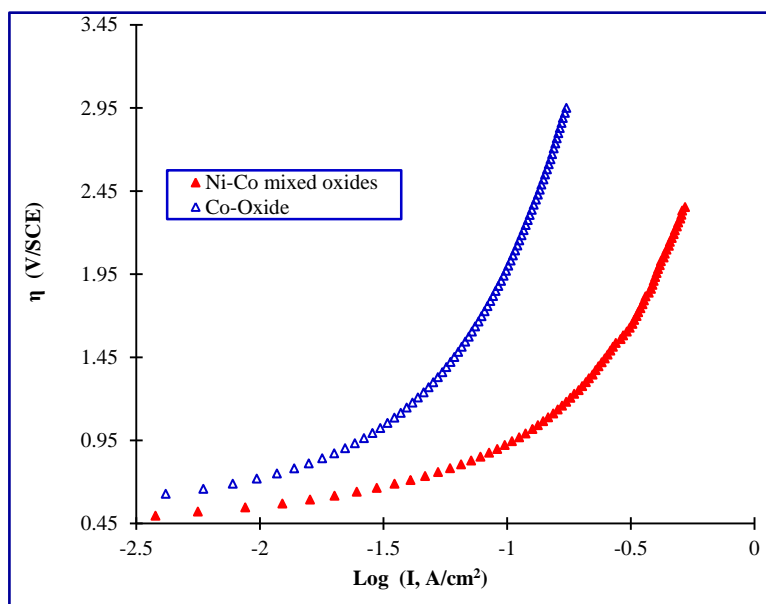


Figure 3.55 Tafel plots obtained from the I-V (current density I and potential, V) curve during OER on Ni-Co mixed oxide and Co-oxide thin films. The overpotentials for OER were obtained using $\eta = E_{\text{app}} - 0.116$ where E_{app} is the measured potential at the electrode during OER.

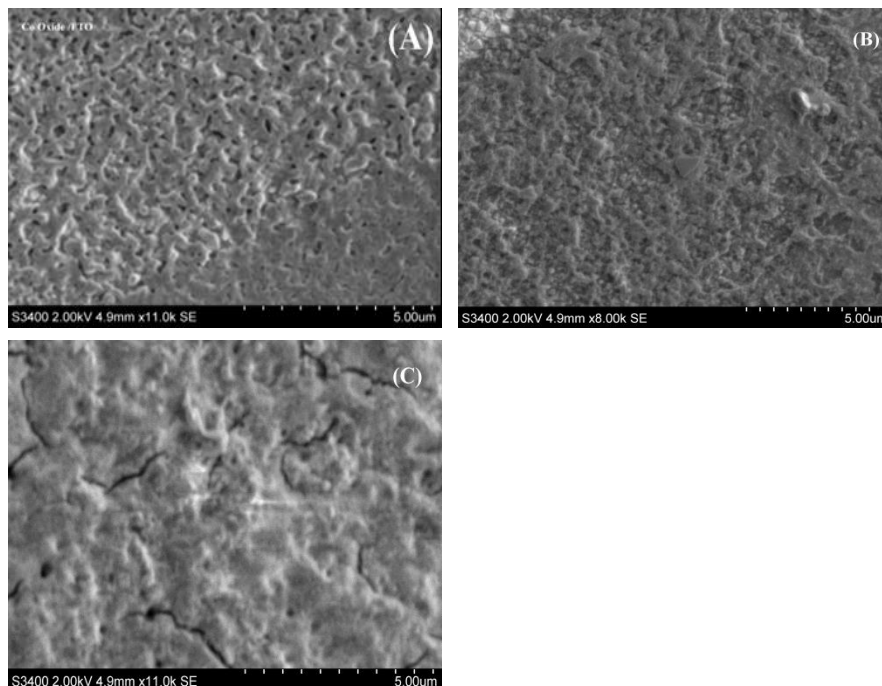


Figure 3.56 SEM Pictures of (A) Co-oxide on FTO coated glass substrate (B) Ni-Co-mixed oxide on FTO coated glass substrate (c) Porous Ni-Cobalt oxide plate.

3.5.4 Summary

Ni-Co mixed oxide anodes can be synthesized by spray pyrolysis on fluorine doped tin oxide conductive glass. These Ni-Co mixed oxide thin films exhibit a high catalytic activity towards oxygen evolution compared to the high efficient Co-monoxide thin film electrode. The High activity could be due to the synergetic effect of mixed oxides which helped to generate electroactive sites for efficient oxygen evolution. In this study a correlation between the transition from lower oxidation state to a higher oxidation state of the metal oxide thin film and an early oxygen evolution was observed. It is noteworthy to point out that this correlation remains as the sole electrochemical descriptor for an efficient oxygen evolution using transition metal oxide electrodes.

REFERENCES

1. Vezirouglou, T. N. *International of Hydrogen energy* **1998**, 23, 1077.
2. Sumida, K.; Rogow, D. L.; Mason, J. A.; McDonald, T. M.; Bloch, E. D.; Herm, Z. R.; Bae, T.; Long, J. R. *Chemical Reviews* **2012**, 112, 724-781.
3. Venkatesh, A.; Jaramillo, P.; Griffin, W. M.; Matthews, H. S. *Environmental Scienec & Technology* **2012**, 46, 9838-9845.
4. Paul, J. C.; Steinbach, P. B.; Ownby, D. R. *Energy & Fuels* **2008**, 22, 3949-3954.
5. Lopez, D.; Buitrago, R.; Escribano, A. S.; Reinoso, F. R.; Mondragon, F. *Journal of Physical Chemistry C* **2008**, 112, 15335-15340.
6. McConnell, V. P. Composites and the fuel cell revolution. *Reinforced Plastics* **2002**, 46, 38-40.
7. *Annual energy outlool*; U. S. Energy administration, 2012.
8. Borup, R.; Meyers, J.; Pivovar, B.; Kim, Y. S.; Mukundan, R.; Garland, N.; Meyers, D.; Wilson, M.; Garzon, F.; Wood, D. e. a. *Chemical Review* **2007**, 107, 3904-3951.
9. Antolini, E. *Journal of energy materials* **2003**, 38, 2995-3005.
10. Bockris, J. O.; Srinivasan, S. *Fuel Cells: Their electrochemistry*; McGraw Hill, 1969.
11. Fujishima, A.; Honda, K. *Nature* **1972**, 238, 37.
12. Linsebigler, A.; Lu, G.; Yates, J. T. *Chemical Reviews* **1995**, 95, 735-758.
13. Thompson, T. L.; Yates, J. T. *Journal of Chemical Review* **2006**, 106, 4428-4453.
14. Chen, X.; Shen, S.; Guo, L.; Mao, S. S. *Chemical Reviews* **2010**, 110, 6503-6570.
15. Khan, S. U. M.; Al-Shahry, M.; Ingler Jr, W. *Science* **2002**, 297, 2243-2245.
16. Mohapatra, S. K.; Misra, M. *Journal of Physical Chemistry C* **2007**, 111, 11506-11510.
17. Bak, T.; Nowotny, J.; Rekas, M.; Sorrell, C. C. *International Journal of Hydrogen Energy* **2002**, 27, 19-26.
18. Kisch, H.; Macyk, W. *Chemiphyschem* **2002**, 3, 399-400.
19. Asahi, R.; Morikawa, T.; Ohwaki, T.; Aoki, K.; Taga, Y. *Science* **2001**, 293, 269-271.
20. Umabayashi, T.; Ymaki, T.; Yamamoto, S.; Miyashita, A.; Tanaka, S.; Asai, K. *Journal of Applied Physics* **2003**, 93, 5156.
21. Umabayashi, T.; Yamaki, T.; Itoh, H.; Asai, K. *Applied Physics Letters* **2002**, 81, 454-456.
22. Ingler, W. B.; Khan, S. U. M. *Electrochemical Solid State Letters* **2006**, 9, G144-G146.
23. Wag, G.; Ling, Y.; Wang, H.; Yang, X.; Wang, C.; Zhang, J. Z.; Li, Y. i. *Energy and Environmental Science* **2012**, 5, 6180-6187.
24. Sayama, K.; Arakawa, H. *Journal of Photochemistry and Photobiology A:*

- Chemistry* **1996**, 94, 67-68.
25. Licht, S. *Journal of Physical Chemistry B* **2001**, 105, 6281-6294.
 26. Licht, S.; Wang, B.; Mukerji, S.; Soga, T.; Umeno, M.; Tributsch, H. *Journal of Physical Chemistry B* **2000**, 104, 8920-8924.
 27. Khaselev, O.; and Turner, J. A. *Science* **1998**, 280, 425-427.
 28. Wang, H.; Lewis, J. P. *Journal of Physics: Condensed matter* **2006**, 18, 421-434.
 29. Umebayashi, T.; Yamaki, T.; Itoh, H.; Asai, K. *Journal of Physical Chemical Solids* **2002**, 63, 1909-1920.
 30. Bellardita, M.; Addamo, M.; Di Paola, A.; Palmisano, L. *Chemical Physics* **2007**, 339, 94-103.
 31. Zabova, H.; Cirkva, V. *Journal of Chemical Technology and Biotechnology* **2009**, 84, 1624-1630.
 32. Jie, H. S.; Park, H.; Lee, K. B.; Chang, H. J.; Ahn, J. P.; Park, J. K. *Surface Interface Analysis* **2012**, 44, 1449-1452.
 33. Zhu, H.; Tao, J.; Dong, X. *Journal of Physical Chemistry C* **2010**, 114, 2873-2879.
 34. Wang, C. y.; Bahnemann, D. W.; Dohrmann, J. K. *Chemical Communication* **2000**, 0, 1539-1540.
 35. Graciani, J.; Ortega, Y.; Sanz, J. F. *Chemistry of Materials* **2009**, 21, 1431-1438.
 36. Breckenridge, R. G.; Hosler, W. R. *Physical Review* **1953**, 91, 793-802.
 37. Chen, X.; Liu, L.; Yu, P. Y.; Mao, S. S. *Science* **2011**, 331, 746-750.
 38. Chen, X.; Liu, L.; Liu, Z.; Marcus, M. A.; Wang, W. C.; Oyler, N. A.; Grass, M. E.; Mao, B.; Glans, P. A.; Yu, P. Y.; Guo, J.; Mao, S. S. *Nature* **2012**, 1-7.
 39. Torres, G. R.; Lindgren, T.; Lu, J.; Granqvist, G. C.; Lindquist, S. E. *Journal of Physical Chemistry B* **2004**, 108, 5995-6003.
 40. Irie, H.; Watanabe, Y.; Hashimoto, K. *Journal of Physical Chemistry B* **2003**, 107, 5483-5486.
 41. Tachikawa, T.; Tojo, S.; Kawai, K.; Endo, M.; Fujitsuka, M.; Ohno, T.; Nishijima, K.; Miyamoto, Z.; Majima, T. *Journal of Physical Chemistry B* **2004**, 108, 19299-19306.
 42. Mohapatra, S. K.; Mahajan, V. K.; Misra, M. *Nanotechnology* **2007**, 18, 445705-445711.
 43. Xu, C.; Shaban, Y. A.; Ingler, W. B.; Khan, S. U. M. *Solar Energy Materials and Solar Cells* **2007**, 91, 938-943.
 44. Di Valentin, C.; Pacchioni, G.; Selloni, A. *Chemical Matter* **2005**, 17, 6656.
 45. Lin, Y.; Zhou, S.; Sheehan, S. W.; Wang, D. *Journal of The American Chemical Society* **2011**, 133, 2398-2401.
 46. Kleiman-Shwarsctein A, H. Y. F. A. S. G. M. E. *Journal of Physical Chemistry* **2008**, 112, 15900-15907.
 47. Khan, S. U. M.; Zhou, Z. Y. *Journal of Electroanalytical Chemistry* **1993**, 357, 407-420.
 48. Sanchez, C.; Sieber, K. D.; Somorjai, G. A. *Journal of Electroanalytical Chemistry*

- 1988**, 90, 252-269.
49. Cesar, I.; Kay, A.; Gonzalez, J. A.; Gratzel, M. *Journal of American Chemical Society* **2006**, 128, 4582-4583.
 50. Khan, S. U. M.; Akikusa, J. *Journal of Physical Chemistry B* **1999**, 103, 7184-7189.
 51. Ingler, J. W. B.; Khan, S. U. M. *International Journal of Hydrogen Energy* **2005**, 30, 821-827.
 52. McGregor, K. G.; Calvin, M.; Otvos, J. W. *Journal of Applied Physics* **1979**, 50, 369-373.
 53. Khader, M. M.; Lichtin, N. N.; Vurens, G. H.; Salmeron, M.; Somorjai, G. A. *Langmuir* **1987**, 3, 303-304.
 54. Satsangi, V. R.; Kumari, S.; Singh, A. P.; Shrivastav, R.; Dass, S. *International Journal of Hydrogen Energy* **2008**, 33, 312-318.
 55. Kay, A.; Cesar, I.; Gratzel, M. *Journal of American Chemical Society* **2006**, 128, 15714-15721.
 56. Hu, Y.; Kleiman-Shwarsstein, A.; Forman, A. J.; Hazen, D.; Park, J.; McFarland, E. W. *Chemistry of Materials* **2008**, 20, 3803-3805.
 57. Wheeler, D. A.; Wang, G.; Ling, Y.; Li, Y.; Zhang, J. Z. *Energy & Environmental Science* **2012**, 5, 6682-6702.
 58. Vayssieres, I.; Sathe, c.; Butorin, S. M.; Shuh, D. K.; Nordgren, J.; Guo, J. *Advanced Material* **2005**, 17, 2320-2323.
 59. Goetzberger, A.; Hoffmann, V. U. *Photovoltaic solar energy generation* ; Springer, 2005.
 60. Rech, B.; Wagner, H. *Applied Physics A* **1999**, 69, 155-167.
 61. Lin, G. H.; Kapur, M.; Kainthla, R. C.; Bockris, J. O. *Applied Physics Letter* **1989**, 55, 4386.
 62. Kainthla, C.; Zelenay, B.; O'M., B. J. *Journal of Electrochemical Society* **1986**, 133, 248.
 63. Morisaki, H.; Watanabe, T.; Iwase, M.; Yazawa, K. *Applied Physics Letters* **1976**, 29, 338.
 64. Kainthla, C.; Zelenay, B.; O'M., B. J. *Journal of Electrochemical Society* **1987**, 134, 841.
 65. Reece, S. Y.; Hamel, J. A.; Sung, K.; Jarvi, T. D.; Esswein, A. J.; Pijpers, J. J. H.; Nocera, D. G. *Science* **2011**, 334, 645.
 66. Smith, R. D. L.; Prévot, M. S.; Fagan, R. D.; Zhang, Z.; Sedach, P. A.; Siu, M. K. J.; Trudel, S.; Berlinguette, C. P. *Science* **2013**, 340, 60-63.
 67. Whitesides, G.; Crabtree, G. W. *Science* **2007**, 315, 796-798.
 68. Marcelo, D.; Dell'Era, A. . *International Journal of Hydrogen Energy* **2008**, 33, 3041.
 69. Mallouk, T. E. *Nature Chemistry* **2013**, 5, 362-363.
 70. Cook, T. R.; Dogutan, D. K.; Reece, S. Y.; Surendranath, Y. T. T. S.; Nocera, D. G. *Chemical Review* **2010**, 110, 6474-6473.

71. Walter, M. G.; Warren, E. L.; McKone, J. R.; Boettcher, S. W.; Mi, Q.; Santori, E. A.; Lewis, N. S. *Chemical Review* **2010**, *110*, 6446-6473.
72. Alonso-Vante, N.; Colell, H.; Stimming, U.; Tributsch, H. *Journal of physical Chemistry* **1993**, *97*, 7381-7382.
73. Boodts, C. F.; Trasatti, S. *Journal of Electrochemical Society* **1990**, *137*, 3784-3789.
74. Alves, V. A.; DaSilva, L. A.; Boodts, J. F. C.; Trasatti, S. *Electrochimica Acta* **1994**, *39*, 1585-1589.
75. Trasatti, S. *Electrochimica Acta* **1980**, *29*, 1503.
76. Bockris, J. O.; Otagawa, T. *Journal of The Electrochemical Society* **1984**, *131*, 290-302.
77. Suntivich, J.; May, K. J.; Gasteiger, H. A.; Goodenough, J. B.; Shao-Horn, Y. *Science* **2011**, *334*, 1383-1385.
78. Gerken, J. B.; McAlpin, J. G.; Chen, J. Y. C.; Rigsby, M. L.; Casey, W. H.; Britt, R. D.; Stahl, S. *Journal of American Chemical Society* **2011**, *133*, 14431.
79. Kanan, M. W.; Nocera, D. G. *Science* **2008**, *321*, 1072.
80. Risch, M.; Khare, V.; Zaharieva, I.; Geencser, L.; Chernev, P.; Dau, H. *Journal of American Chemical Society* **2009**, *131*, 6936.
81. Zhang, Q.; Wei, Z. D.; Liu, C.; Liu, X.; Qi, X. Q.; Chen, S. G.; Ding, W.; Ma, Y.; Shi, F.; Zhou, Y. M. *International Journal of Hydrogen Energy* **2012**, *37*, 10479.
82. Castro, E. B.; Real, S. G.; Pinheiro, D. L. F. *International Journal of Hydrogen Energy* **2004**, *29*, 255-261.
83. Hu, C. C.; Lee, Y. S.; Wen, T. C. *Material Chemistry and Physics* **1997**, *48*, 246.
84. Silva, G. C.; Fugivara, C. S.; Filho, T. G.; Sumodjo, P. T. A.; Benedetti, A. V. *Electrochimica Acta* **2002**, *47*, 1875.
85. Castro, E. B.; Gervasiz, C. A.; Vilche, J. R. *Journal of Applied Electrochemistry* **1998**, *28*, 835.
86. Shim, H. S.; Shinde, V. R.; Kim, H. J.; Sung, Y. E.; Kim, W. B. *Thin Silid Films* **2008**, *516*, 8573.
87. Trasatti, S. *Electrochimica Acta* **1991**, *36*, 225.
88. Bocca, C.; Barbucci, A.; Delucchi, M.; Cerisola, G. *International Journal of hydrogen Energy* **1999**, *24*, 21.
89. Szklarczyk, M.; Bockris, J. O. *Journal of physical Chemistry* **1984**, *88*, 5241.
90. Benea, L.; Bonora, P. L.; Borellos, A.; Martelli, S.; Wenger, F.; Ponthiaux, P.; Galland, J. *Solid State Ionics* **2002**, *151*, 89-95.
91. osioptoelectronics. <http://www.osioptoelectronics.com/standard-products/silicon-photodiodes/general-purpose-photodiodes/blue-enhanced-photodiodes.aspx> (accessed August 2013).
92. Reference Solar Spectral Irradiance: Air Mass 1.5. <http://rredc.nrel.gov/solar/spectra/am1.5/> (accessed Sept 15, 2013).
93. Neumann, B.; Bogdanoff, P.; Tributsch, H.; Sakthivel, S.; Kisch, H. *Journal of physical Chemistry B* **2005**, *109*, 16579.

94. Van de Krol, R.; Liang, Y.; Schoonman, J. *Journal of Materials Chemistry* **2008**, *18*, 2311-2320.
95. Lemon, B. L.; Hupp, J. T. *Journal of Physical Chemistry* **1996**, *100*, 14578-14580.
96. Schaub, R.; Wahlstrom, E.; Ronnau, A.; Laegsgaard, E.; Stenggaard, I.; Besenbacher, F. *Science* **2003**, *17*, 377-379.
97. Strunk, J.; Vining, W. C.; Bell, A. B. *Journal of Chemical Society C* **2010**, *114*, 16937-16945.
98. Shankar, K.; Basham, J. I.; Allam, N. K.; Varghese, K. O.; Mor, G. K.; Feng, X.; Paulose, M.; Seabold, J. A.; Choi, K. S.; Grimes, C. A. *Journal of Physical Chemistry C* **2009**, *113*, 6327-6359.
99. Reichman. *Journal of Applied Physics* **1981**, *38*, 251.
100. Burda, C.; Lou, Y.; Chen, X.; Samia, A. C. S.; Stout, J.; Gole, J. L. *Nano Letters* **2003**, *3*, 1049-1051.
101. Schaub, R.; Wahlström, E.; Rønnau, A.; Lægsgaard, E.; Stensgaard, I.; Besenbacher, F. *Science* **2003**, *299*, 377-379.
102. Mor, G. K.; Shankar, K.; Paulose, M.; Varghese, O. K.; Grimes, C. A. *Nano Letters* **2006**, *6*, 215-218.
103. Liu, B.; Aydil, E. S. *Journal of American Chemical Society* **2009**, *131*, 3985-3990.
104. Tsaq, Y.; Sondergaard, T.; Skovsen, E.; Gurevich, L.; Pederson, K.; Pederson, T. G. *Optics Express* **2013**, *21*, A84-A95.
105. Ko, Y. H.; Raju, G. S. R.; Kim, S.; Yu, J. S. *Physica Status Solidi A* **2012**, *209*, 2161-2166.
106. Oh, J.; Deutsch, T. G.; Yuan, H.; Branz, H. M. *Energy and Environmental Science* **2011**, *4*, 1690-1694.
107. Sim, U.; Jeong, H.; Yang, T.; Nam, K. T. *Journals of Materials Chemistry A* **2013**, *1*, 5414-5422.
108. Baram, N.; Ein-Eli, Y. *Journal of Physical Chemistry C* **2010**, *114*, 9781-9790.
109. Liu, M.; Snapp, N. D.; Park, H. *Chemical Science* **2011**, *2*, 80-87.
110. Schaller, R. D.; Klimov, V. I. *Physical Review Letters* **2004**, *92*, 186601-186604.
111. Ellingson, R. J.; Beard, M. C.; Johnson, J. C.; Yu, P.; Micic, O. I.; Nozik, A. J.; Shabaev, A.; Efros, A. L. *Nano Letters* **2005**, *5*, 865-871.
112. Schaller, R. D.; Sykora, M.; Pietryga, J. M.; Klimov, V. I. *Nano Letters* **2006**, *6*, 424-429.
113. Dutoit, E. C.; Van Meirhaeghe, R. L.; Cardon, F. G. W. P. *Bunsenges Physical Chemistry* **1975**, *79*, 1206.
114. Szklarczykt, M.; Bockris, J. O. *Journal of Physical Chemistry* **1984**, *88*, 5241.
115. Szklarczykt, M.; Bockris, J. O. *Journal of Physical Chemistry* **1984**, *88*, 1808.
116. Bockris, J. O.; Khan, S. U. M. *Surface Electrochemistry*, 1st ed.; Plenum: New York, 1993.
117. Arai, T.; Konishi, Y.; Iwasaki, Y.; Sugihara, H.; Sayama, K. *Journal of Combinatorial Chemistry* **2007**, *9*, 574-581.

118. Gimenez, S.; Dunn, H. K.; Rodenas, P.; Fabregat, F.; Miralles, S. G.; Barea, E. M.; Trevisan, R.; Guerrero, A.; Bisquert, J. *Journal of Electroanalytical Chemistry* **2012**, *668*, 119-125.
119. Park, J. H.; Kim, S.; Bard, A. J. *Nano Letters* **2006**, *6*, 24-28.
120. Allam, N. K.; Shankar, K.; Grimes, G. A. *Journal of Material Chemistry* **2008**, *18*, 2341-2348.
121. Aydil, E. S.; Liu, B. *Nanotechnology* **2008**, *19*, 505604.
122. Shi, J.; Sun, C.; Starr, M. B.; Wang, X. *Nano Letters* **2011**, *11*, 624-631.
123. Chang, C.; Huang, T.; Lin, Y. T.; Lin, Y. Y.; Chen, C.; Chu, T.; Su, W. *Journal of material Chemistry* **2008**, *18*, 2201-2207.
124. Cornell, R. M.; Schwertmann, U. *The Iron Oxides: Structure, Properties, Reactions, Occurrence and Uses*; VCH: New York, 1996.
125. Wang, H.; Brandl, D. W.; Le, F.; Nordlander, P.; Halas, N. J. *Nano Letters* **2006**, *6*, 827-832.
126. Yan, X.; Zou, C.; Gao, X.; Gao, W. *Journal of Material Chemistry* **2012**, *22*, 5629-5640.
127. Borse, P. H.; Jun, H.; Choi, S. H.; Hong, S. J.; Lee, J. S. *Applied Physics Letters* **2008**, *93*, 173103-173106.
128. Akikusa, J.; Khan, S. U. M. *Journal of Physical Chemistry B* **1999**, *103*, 7184.
129. Frites, M.; Shaban, A. Y.; Khan, U. M. K. *International Journal of Hydrogen Energy* **2010**, *35*, 4944-4948.
130. Beerman, N.; Vayssieres, L.; Lindquist, S. E.; Hagfeldt, A. *Journal of Electrochemical Society* **2000**, *147*, 2456-2461.
131. Miller, E. L.; Palauselli, D.; Marsen, B.; Rocheleau, R. E. *Thin Solid Films* **2004**, *466*, 307-313.
132. Gartner, M.; Crisan, M.; Jitianu, A.; Scurtu, R.; Gavrilă, R.; Oprea, I.; Zaharescu, M. *Journal of Sol-Gel science Technology* **2003**, *26*, 745.
133. Akl, A. *Application Surface Science* **2004**, *233*, 307-319.
134. Ling, Y.; Wang, G.; Wheeler, D. A.; Zhang, J. Z.; Li, Y. *Nano Letters* **2011**, *11*, 2119-2125.
135. Bard, A. J.; Fox, M. A. *Account of Chemical Research* **1995**, *28*, 141-145.
136. Park, H.; Vecities, C. D.; Choi, W.; Weres, O.; Hoffmann, M. R. *Journal of Physical Chemistry C* **2008**, *112*, 885.
137. About Us: SunPower. <http://us.sunpowercorp.com/about/newsroom/press-releases/?relID=125454> (accessed September 1, 2013).
138. Rocheleau, R. E.; Miller, E. L.; Misra, A. *Energy Fuels* **1998**, *12*, 3-10.
139. Yamada, Y.; Matsuki, N.; Ohmori, T.; Mametsuka, H.; Kondo, M.; Matsuda, A.; Suzuki, E. *International Journal of Hydrogen Energy* **2003**, *28*, 1167-1169.
140. Kelly, N. A.; Gibson, T. *International journal of Hydrogen Energy* **2006**, *31*, 1658-1673.
141. Kelly, N. A.; Gibson, T. L.; Cai, M.; Spearot, J.; B., O. D. *International Journal of*

- Hydrogen Energy* **2010**, 35, 892-899.
142. Gibson, T. L.; Kelley, N. A. *International Journal of Hydrogen Energy* **2010**, 35, 900-911.
 143. Tributsch, H. *International Journal of Hydrogen Energy* **2008**, 33, 5911-5930.
 144. Peharz, G.; Dimorth, F.; Wittstadt, U. *International of Hydrogen Energy* **2007**, 32, 3248-3252.
 145. Turner, J. A. *Science* **2004**, 305, 972-974.
 146. Wendt, H.; Kreysa, G. *Electrochemical Engineering Science and Technology in Chemical and other Industries*; Springer-Verlag: Berlin Heidelberg, 1999.
 147. Wu, G.; Li, N.; Zhou, D.; Mitsuo, K.; Xu, B. *Journal of Solid State Chemistry* **2004**, 177, 3682-3692.
 148. Pralong, V.; Vidal, A. D.; Beaudoin, B.; Leriche, J. B.; Tarascon, J. M. *Journal of electrochemical Society* **2000**, 147, 1306-1313.
 149. Boots, C. F.; Trasatti, S. *Journal of the Electrochemical Society* **1990**, 137, 3784.
 150. Trasatti, S. *Electrochimica Acta* **1991**, 36, 225.
 151. Khan, S. U. M.; Akikusa, J. *Journal of Electrochemical Society* **1998**, 145, 89.
 152. Trasatti. *Electrochimica Acta* **1984**, 29, 1503-1512.
 153. Ghosh, P. C.; Emonts, B.; Janssen, H.; Mergel, J.; Stolten, D. I. *Solar Energy* **2003**, 75, 469-478.
 154. Jun, S.; Weng, M.; Huang, W. *Journal of Materials Chemistry* **2012**, 22, 20319-20333.
 155. Shaban, A. Y.; Khan, U. M. S. *Science of Advanced Materials* **2012**, 4, 1-9